Protein-lipid interactions in raft-exhibiting membranes probed by combined AFM and FCS

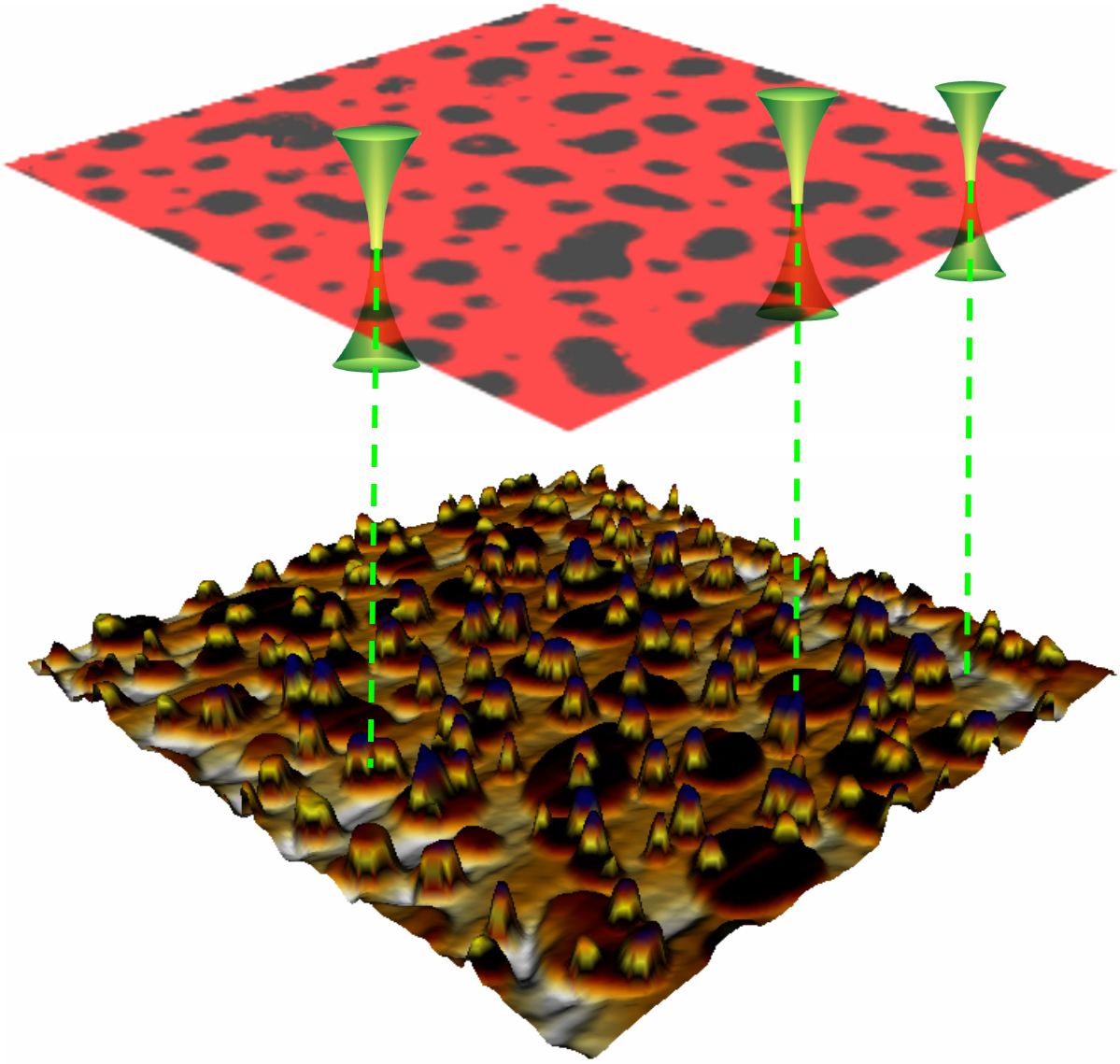

Dissertation zur Erlangung des akademischen Grades
Doctor rerum naturalium (Dr. rer. nat.)

vorgelegt von Salvatore Chiantia

Introduction and Outline

The cellular membrane is a complex biological entity, far from being an inert assembly of protein and lipids which separates cells from the surrounding environment. A multitude of biological processes, ranging from active transport of ions into and out of the cell, to the immune response, are regulated at the level of the plasma membrane. The understanding of their molecular basis is among the central goals of modern biological research. In order to dissect the complexity of actual cell membranes, which involves a very complex network of intermolecular interactions, a "divide and conquer" strategy proves very useful. To this end, researchers try to isolate molecules from complex biological contexts to understand their function in simple model systems under controlled conditions. A variety of model membranes have thus been developed in order to gain insight into membrane processes. This approach has resulted in a deeper knowledge on how lipids and proteins interact and how these interactions govern the function of cellular membranes. In the recent past in fact, a connection has been established between the lateral structure of the plasma membrane and its biological function. Furthermore, a large range of biophysical techniques have been used to characterize protein-lipid microdomains. For example, atomic force microscopy (AFM) can offer a very detailed, though quasi-static, image of the lipid bilayer topography, thus enabling the investigation of phase separation and domain formation with nanoscopic resolution. On the other hand, fluorescence imaging and fluorescence correlation spectroscopy (FCS) are much faster techniques, albeit limited by optical resolution. Through the analysis of fluorescence signal fluctuations, FCS can characterize membrane heterogeneities providing information about the concentration and mobility of membrane components. These two techniques perfectly complement each other, both because of the different time scales involved, and because of the different physical properties –i.e. structure vs. dynamics- which can be probed in the sample.

The thesis is organized as follows: *chapters 1-3* offer a brief introduction to the principles of AFM, FCS and membrane organization respectively. *Chapter 4* deals with the development of a combined AFM-FCS approach and its application to the study of lipid bilayers. Having described the central experimental technique, chapter 5-8 specifically address the use of this technique to answer important biophysical questions. *Chapter 5* focuses on the stability of supported model membranes, with particular emphasis on lipid microdomains in conditions of drought. Stressing environmental conditions can cause a substantial rearrangement in the lateral organization of the lipid bilayer. The understanding of these processes is important, for example, in the long-term storage of red blood cells, platelets and stem cells. *Chapter 6* describes changes in the lateral organization of the membrane which are also important in other cellular events, like apoptosis, senescence or viral pathogenesis. In these cases, a particular lipid called *ceramide* is involved in reorganization of lipid domains *in vivo*. Using a combination of AFM and FCS *in vitro*, we investigate the effects of ceramide on the lateral organization of the membrane on a molecular scale. *Chapter 7* deals with synthetic short-chain ceramide analogues which are often used to mimic the effect of their natural occurring long-chain counterparts, not only in biochemical research but also in medical applications. Nevertheless, these molecules have very different biophysical properties and here we examine their highly dissimilar effects on membrane organization. Finally, moving a step further up in the ladder of complexity, membrane proteins are introduced into our model system and the focus of attention shifts to protein-lipid interactions. In *chapter 8* we study how the organization of proteins in the membrane is influenced by the presence of ceramide, both from a structural and dynamic perspective, and we discuss how these rearrangements can be connected to cellular events observed *in vivo*.

Publications

Articles in relation to this thesis:

Trajkovic K., Hsu C., Chiantia S., Rajendran L., Wenzel D., Schwille P., Brügger B., Simons M. (2007) *A role for ceramide in exosome formation within multivesicular endosomes*, **Science**, in press

Renner L., Osaki T., Chiantia S., Schwille P., Pompe T., Werner C. (2007) *Lipid Bilayer Formation on Thick Polymer Cushions,* **J. Phys. Chem. B**, in press

Chiantia S., Ries J., Chwastek G., Carrer D., Li Z., Bittman R., Schwille P. (2007) *Role of ceramide in membrane protein organization investigated by simultaneous AFM and FCS*, **Biochim. et Biophys. Acta**, in press

Garcia-Sàez A., Chiantia S., Schwille P. (2007) *Effect of line tension on the lateral organization of lipid membranes,* **J. Biol. Chem.**, in press, (Cover-page article)

Chiantia S., Kahya N., Schwille P. (2007) *Raft Domain Reorganization Driven by Short- and Long-Chain Ceramide: a Combined AFM and FCS study*, **Langmuir**, 23:7659-65

Garcia-Sàez A., Chiantia S., Salgado J., Schwille P. (2007) *Pore formation by a Bax-derived peptide: effect on the line tension of the membrane probed by AFM*, **Biophys. J.**, 93:103-112

Chiantia S., Ries J., Kahya N., Schwille P. (2006) *Combination of AFM and 2-focus Scanning FCS on Raft-exhibiting Model Membranes*, **ChemPhysChem.**, Nov 15, 7:2409-18. (Cover-page article)

Chiantia S., Kahya N., Ries J., Schwille P. (2006) *Effects of ceramide on liquid-ordered domains investigated by simultaneous AFM and FCS*, **Biophys. J.**, Jun 15;90(12):4500-8.

Chiantia S., Kahya N., Schwille P. (2005) *Dehydration damage of domain-exhibiting supported bilayers: an AFM study on the protective effects of disaccharides and other stabilizing substances*, **Langmuir**, Jul 5;21(14):6317-23

Chapter 1 – Introduction to Atomic Force Microscopy (AFM)

1.1 Scanning probe microscopy

Scanning probe microscopy (SPM) is a branch of microscopy dealing with the imaging of surfaces via a direct mechanical interaction between a probe and the sample. In this way, images are formed by "feeling" rather than "looking" at the specimen. Furthermore, SPMs can provide information about sample topography with resolution and magnification typical of electron microscopy, but under physiological imaging conditions that are normally associated only with light microscopy.

From a historical point of view, SPM was born in the early 1980s, when Binnig and Rohrer revolutionized the world of microscopy with the invention of the scanning tunneling microscopy (STM) (1,2). In particular, they built an apparatus which could measure the separation between a sharp metallic probe and a conducting surface, via monitoring the exponential decay of the tunneling current with increasing distance. If the probe-sample distance changes a few angstroms, the current will be an order of magnitude lower. The importance of this invention granted these scientists the award of the Nobel Prize in Physics in 1986. In the same year, Binnig and colleagues announced the invention of the second member of the SPM family: the atomic force microscopy (AFM), also known as scanning force microscopy (SFM) (3). AFMs began to be commercially available in the early 1990s and, few years later, also combinations of SPM and optical microscopes started to appear. A particular example of such combination is the scanning near field optical microscopy (SNOM).

In this context the word "microscopy" might be misleading, since SPMs operate in a very peculiar way compared to optical microscopes. Conventional far field microscopes image samples collecting transmitted or reflected radiation. The resolution is thus limited by Abbe´s diffraction limit depending on the used wavelength. For light microscopes, the resolution limit is ca. 200 nm. Higher resolution can be achieved using high energy electrons in the electron microscope (EM), whose associated wavelength can go down to few nanometers. Unfortunately, molecular resolution still requires that the samples are imaged under vacuum conditions. On the other hand, SPM imaging derives from measuring the interaction between the probe and the sample during the scanning of the surface. Hence the resolution depends on the sharpness of the tip and on the positional accuracy of the probe on the sample. Interestingly, SPM can image most biopolymers with sub-molecular resolution in gaseous or liquid (i.e. physiological) environment.

The first SPM biological studies have been performed using STM. Although STM offers the highest resolution achievable by SPMs, the samples have to be relatively flat and conductive. These requirements offset the main advantages of the SPM method. Using AFM, there are no major restrictions in sample size or topography, and biological samples, ranging in size from macromolecules to whole cells, can be imaged in their native state.

1.2 AFM: principle and setup

As previously said, AFM images sample by "feeling" rather than "seeing". In analogy with a blind person who feels an object with his fingers and builds up a mental image of what they

are touching, AFM can produce a detailed picture not only of the topographical features of the sample, but also of its surface characteristics.

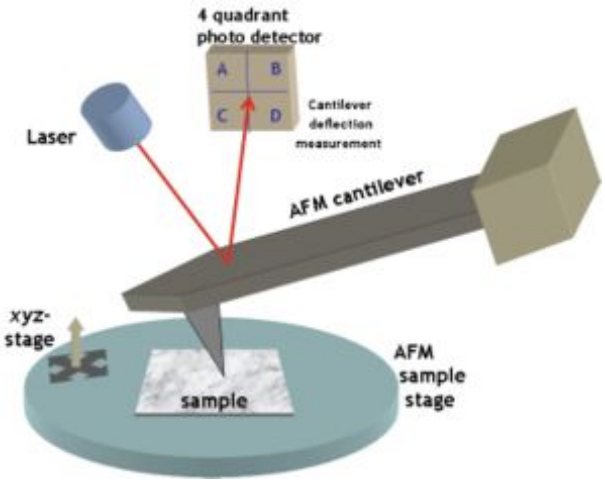

Figure 1.1 *Schematic representation of the atomic force microscope setup. From www.answers.com/topic/nanotechnology.*

Figure 1.1 illustrates the main features of the AFM setup. The first part consists of a sharp tip mounted at the end of a cantilever which is, in turn, bonded to a glass chip. The flexible cantilever allows the tip to move up and down following the sample's topography. Furthermore, the cantilever has a well-defined, usually very low (10^{-2}-10^{0} N/m), spring constant that allows the AFM to control the force applied on the sample with great precision while the sample surface is scanned (4).

The second part of the setup is the scanning mechanism. The accurate positioning of the tip relative to the sample is performed by means of a piezoelectric transducer. When a potential difference is applied on a piezoelectric ceramics, this expands or contracts with an achievable accuracy of atomic dimensions. In this way, the motion of the tip (or of the sample, depending of the specific AFM design) can be controlled in the three orthogonal directions x, y, and z, which are monitored by three different channels in the instrument's control electronics. While the x and y channels refer to the position of the tip on the sample's surface, the z channel monitors the height of the cantilever (5).

The third and final part of the AFM setup is the detection mechanism. There are several ways to monitor the deflection of the cantilever, but the most common one, also used for the work described in this thesis, is the so-called "optical lever" method. A laser beam is focused on the end of the cantilever and is reflected on a four-segment photodiode. As the tip moves in response to the sample topography, the reflected spot moves on the photodiode changing in intensity in each quadrant. The difference in laser intensities between the top two segments and the bottom two produces an electric signal that is correlated to the normal motion of the tip. The difference between the laser intensity in the left and right segment pairs produces a signal that is, in turn, correlated to any lateral or twisting motion of the cantilever. This simple method is sensitive enough to detect atomic scale movements of the tip-cantilever system, while it is scanned above the sample's surface.

During the scanning of the sample, the surface topography makes the cantilever deflect while the force between the tip and the sample changes. In the most common AFM operating mode, the so-called contact mode with constant deflection (i.e. constant force), the cantilever deflection is maintained at a chosen constant set-point level by a feedback loop which continuously adjusts the z displacement of the piezoelectric scanner and thus the tip-sample distance. Usually, the AFM software allows the control of the parameters for the proportional (P gain) and integral (I gain) gain of the z feedback loop. If the values of these parameters are not high enough, the z-scanner has a delayed reaction to the topography and the cantilever

might bend too much (i.e. apply too high force), thus damaging the sample. On the other hand, too high values for the gain parameters might cause oscillations in the system. In this operation mode, the x, y, and z displacements of the piezoelectric scanners are recorded and displayed as an image of the sample's topography (6).

1.3 Interaction forces and imaging modes

The interaction between the sample and the tip varies while the tip is scanned over the sample's surface. As a result, the cantilever bends elastically. The operation of the AFM depends on the measurement of the forces between the sample and the tip that, in the case of biological specimens, are usually van der Waals, electrostatic, capillary/adhesive and double layer forces.

Van der Waals (or London) forces are weak attractive interactions between electrically neutral molecules. They originate from fluctuations of the electrons spatial distribution in a molecule that give rise to an "instantaneous" electric dipole. This subtle charge imbalance can induce a similar imbalance in a neighboring molecule, the result being that the slightly positively charged end of one molecule will be attracted to the negatively charged end of the other molecule. Usually this effect is hidden by much larger forces, like those originating from electrostatic interactions. But in absence of other forces, it is possible to picture the force-distance relationship between the tip and the sample simply in terms of van der Waals interactions and the Pauli Exclusion Principle. In particular, as the tip-sample distance r changes, the variation of the potential energy of the system can be described by the pair-potential energy function $E^{pair}(r)$. The special case of the $E^{pair}(r)$ used to describe this physical system is called "Lennard-Jones" potential:

$$E^{pair}(r) = 4\varepsilon\left[\left(\frac{\sigma_0}{r}\right)^{12} - \left(\frac{\sigma_0}{r}\right)^{6}\right] \tag{1.1}$$

where σ_0 and ε are constants depending on the material, the value of σ_0 being comparable to the radius of the atoms involved. The $1/r^{12}$ term accounts for the steep increase in repulsive force between the tip and the sample for very small distances, where atoms strongly repel each other due to the Pauli Exclusion Principle. The negative $1/r^6$ term accounts for the weak attractive van der Waals force at relatively large distances. If we imagine to slowly approach the sample's surface with the cantilever, when r is much bigger than σ, the force between the atoms at the end of the tip and those in the sample will be practically zero. As the separation is decreased, the cantilever will start to bend towards the sample in response to the attractive van der Waals forces. Almost abruptly, the tip will land on the sample and this phenomenon is called "jump to contact". If the cantilever keeps moving downwards, the bent cantilever will straighten out and the force between the sample and the tip will be minimal. This is the best condition to image the sample. Obviously, if the cantilever is moved further downwards, the tip will start applying a force on the sample and the cantilever will bend upwards.

If both the AFM tip and the sample posses a net electric charge, van der Waals interactions become usually neglectable and the tip-sample interactions are dominated by Coulomb and double layer forces: two charged atoms will attract or repel each other and the interaction will be measurable even at distances that are large compared to the typical distances involved in van der Waals interactions, as the potential energy is in this case inversely proportional to the distance r. Nevertheless, when imaging in aqueous media and physiological conditions, oppositely charged ions will accumulate between the charged surfaces creating a so called "ionic atmosphere". In this case, the potential decays exponentially away from the surface, and the thickness of this ionic atmosphere is called "Debye length" ($1/k_D$). For small values

of the surface potentials (Ψ_0), the potential at a distance x ($\Psi(x)$) can be expressed according to the Debye-Hückel approximation: $\Psi(x) \approx \Psi_0 e^{-k_D x}$.

The greater the ionic strength of the imaging buffer, the lower the influence of electrostatic forces on the tip-sample interactions. In the case of uncontrolled electrostatic interactions, artifacts in the determination of the height of biological molecules can arise, for example, due to repulsion of the tip (7). Electrical shielding of the AFM tip can nevertheless be achieved using for example low (few mM) concentration of divalent metal ions in the imaging medium. (8). It is necessary to take into account the balance between van der Waals and Coulomb forces if sub-nanometer resolution of soft biological matter is to be achieved (9).

Finally, it is important to point out that AFM tips can wear out with usage. The apex of the tip might become blunt and contaminated with small amounts of sample. This leads to a larger contact area between tip and sample, unspecific interactions and ultimately to what is known as "adhesive forces". Such forces can represent a problem when imaging small and delicate objects and should be kept under control by often starting afresh with a new tip (10,11).

Depending on the main interaction force, several imaging modes can be distinguished.

"Contact -dc- mode" is the most common imaging mode. The AFM tip is brought in direct contact with the sample and then scanned over its surface. This process can be performed both in air and in water (or buffer solution), but scanning in water environment has the obvious advantage of eliminating capillary forces which can arise from the nanoscopic layer of water present on the surface of "dry" samples. Contact mode thus allows much greater precision in determining and controlling the applied forces. In the most common cases, this imaging mode is also called "constant force mode". The value of the imaging force is, in fact, set constant in the instrument software and this is equivalent to performing the scan with the cantilever bent at a constant small angle. The larger the cantilever deflection, the larger the applied force on the sample. Imaging conditions should always be optimized so to have the minimum possible force but still satisfying contrast and definition of the sample's topographic features.

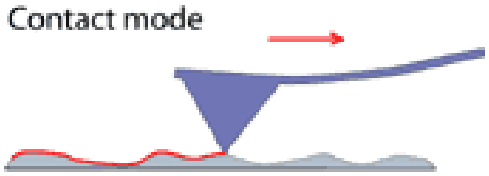

Figure 1.2 *Contact mode imaging. The arrow represents the scanning direction. From www.jpk.com*

As an alternative to the contact mode imaging, the tip can also be oscillated over the sample during the scan. Typical driving frequencies are in the range of 5-10 kHz (close to cantilever resonance in water) with 1-10 nm amplitude, so that the tip touches the sample only instantaneously, at the extreme points of the oscillations. The transient contact with the sample surface can effectively shift the resonance frequency of the cantilever. Given that the driving frequency of the piezo is kept constant, the interaction with the sample will finally result in a damping of the oscillation: the energy transfer between the oscillating piezo and the cantilever is indeed optimal only when the driving frequency is very close to the resonance frequency of the system. In this so-called "Tapping" or "alternated-contact" mode (12), the amplitude of the oscillation is then the feedback parameter and is kept constant by changing the height of the cantilever (13). This imaging mode has the advantage of strongly reducing the shear or lateral forces exerted by the tip on the sample and this could be particularly useful in the case of biological samples that are very fragile or weakly attached to the substrate.

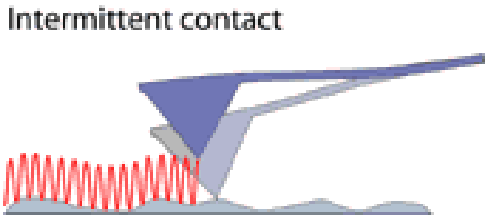

Figure 1.3 *Intermittent contact mode imaging. From www.jpk.com*

Finally, it is possible to image the sample by oscillating the tip few nm above the sample, like in alternated-contact mode, but without any even transient contact. In this case, the oscillations are not damped by direct short-range interaction with the sample but only by the long range van der Waals interactions. This imaging mode, called "true non contact mode" can be useful in further reducing unwanted deformation and shear stress of the sample.

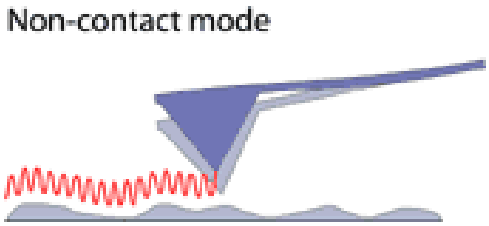

Figure 1.4 *Non-contact mode imaging. From www.jpk.com*

In all the imaging modes described so far, the instrument output that creates the topographic image of the sample is the height of the cantilever which satisfies the set parameters (e.g. constant cantilever deflection in contact mode, constant amplitude in alternate-contact mode…). For this reason, the obtained image is also called "height image". Nevertheless, there are three more types of output signals originated during the scanning process, namely the vertical deflection of the cantilever, the lateral deflection and the phase lag. Though not directly related to the topography of the sample, all these signals can provide information about the surface properties.

As already said, in contact mode, the tip tracks accurately the surface of the sample because the feedback loop keeps the bending of the cantilever at a (low) constant value. Of course this process is not perfect and, when the tip suddenly encounters an obstacle during the scanning, the cantilever will bend before the system can adjust the height of the cantilever to correct for the bending. This will always happen at the border of topographical features and, if the feedback does not respond fast enough, will result in blurred height images. As the bending of the cantilever is continuously monitored and recorded as "error signal", the unwanted bending will also result as a peak in the so-called "error signal image". In other words, the error signal image (or vertical deflection image) presents a positive peak when the cantilever has suddenly to bend upwards and a negative peak when it has to bend downwards. For these reason, the error signal can be imagined as the mathematical first derivative of the height image. It is in fact flat if the height does not change considerably, and presents sharp features (positive or negative) when the height changes suddenly.

Again in contact mode, additional information can be gained from monitoring the lateral twisting of the cantilever. Depending on the scanning speed and on the applied vertical force, the friction between the sample surface and the tip can in fact bend the cantilever laterally. This movement is easily recorded with the above described four-segment photodiode. The signal so obtained is recorded as "friction image" (lateral deflection image, or lateral force image) and can give information about the surface properties of the sample (e.g. surface electric charge) that influence the friction with the scanning tip, independent of surface topography.

When using any non-contact mode, it is also possible to monitor the difference in phase between the driving frequency and the effective oscillation frequency of the cantilever. The phase lag signal is recorded as "phase image". In analogy with the friction image, the phase image can be used to distinguish different surface chemistry, or to study changes in the local elastic properties of the sample, independent of the surface topography.

1.4 Force measurements in molecular films

The AFM is not only a method to measure the topography or the surface properties of solid samples. Simply because of the way this technique works, AFM is first of all a method to measure very small forces. Following Hooke's law: $f=-K\Delta z$, where f is the force applied on/by the cantilever, K is the spring constant of the cantilever and Δz is the deflection of the cantilever, it is possible to measure the force applied on/by the sample monitoring the deflection of the cantilever. The precision of AFM force measurements is mainly limited by thermal motion. The molecules in liquid constantly interacting with the cantilever posses an average energy equal to $\sim \frac{1}{2} k_B T$ for each degree of freedom, where k_B is the Boltzmann constant. The thermal energy can be transferred to the continuously vibrating cantilever and transformed in average elastic energy. This corresponds to a typical force of few pN (14), which is then the lower limit for a force appreciable by AFM. An extensive review of the subject of AFM force measurements is provided by Butt et al. (15).

In this paragraph, we will rather focus on the application and measurements of forces on adsorbed layers with a well defined structure normal to the solid support surface like, for example, lipid bilayers. Lipid organization will be the subject of chapter 3 of this thesis, but for the comprehension of this paragraph it will suffice to know that lipid bilayers can be considered as two-dimensional liquids: individual molecules can diffuse laterally, but they are confined in the normal direction. When the AFM is used to apply a controlled force on the bilayer, a typical pattern is observed. Firstly, at large separation, no interaction between the layer and the tip is observed (i.e. no deflection of the cantilever). At closer distance, the tip is subjected to a repulsive force increasing linearly with further reduction of the height of the cantilever. Once a certain threshold is reached (threshold yield), the lipid layer ruptures and the tip jumps to contact with the solid support. Such jump is visualized as a discontinuity in the force vs. z-piezo displacement curve (16). Figure 1.5 gives an example of such discontinuity, as measured in a supported lipid bilayer made of dioleoyl-phosphatidylcholine, sphingomyelin and cholesterol (17).

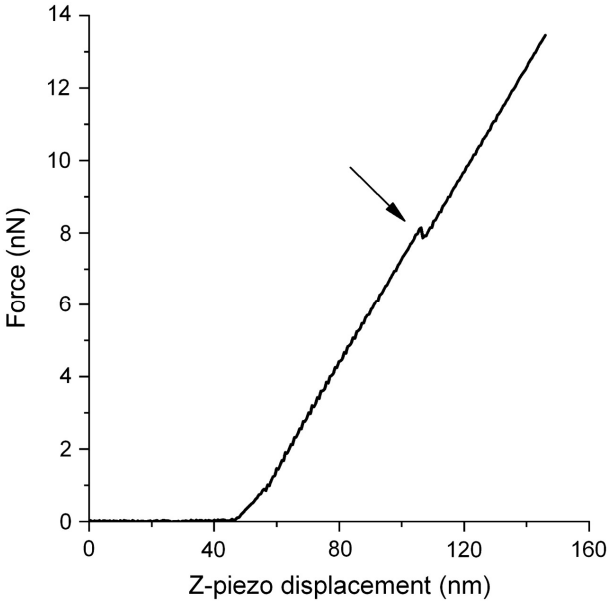

Figure 1.5 *Typical force-distance curve measured on supported lipid bilayer made of dioleoyl-phosphatidylcholine, sphingomyelin and cholesterol (17). The arrow indicates the discontinuity in the curve that is referred to as "threshold yield".*

Such jumps occur not only in the case of solid supported lipid bilayers, but also in other systems like surfactants layers (18). Rupture of thin films has been extensively studied because of its importance in industrial and natural processes. Using a model based on the continuum nucleation theory (19), it is possible to describe the rupture of the bilayer in presence of a force as an activated process. Briefly, the energy that is released when a hole of radius r_h is formed in presence of a compression force *f* applied by an AFM tip or radius R is:

$$E = -\Gamma 2\pi r_h - \pi r_h^2 (S + f/2\pi R) \tag{1.2}$$

where Γ is the line tension and *S* is the surface energy. The first two terms express then the energy that has to be paid (hence the negative sign) to open the hole. The third term expresses the compression of the film. The higher the applied force, the easier the opening of the hole will be. Once this activation barrier is overcome, the tip will penetrate through the bilayer. It is possible then to calculate the probability to measure a certain threshold yield F_t, following Arrhenius law:

$$\ln P(F_t) = -\frac{A}{K\nu}\int_{F_S}^{F_t} \exp\left(-\frac{c}{F' - F_S}\right) dF' \tag{1.3}$$

$$c = \frac{2\pi^2 \Gamma^2 R}{k_B T}$$

$$F_S = 2\pi RS$$

where *A* can be approximated by the resonance frequency of the cantilever, k_B is the Boltzmann constant, *T* is the temperature, and *K* the spring constant of the cantilever.

Equation 1.3 can be integrated analytically (16) and dP/dF_t can be calculated:

$$\frac{dP}{dF_t} = \frac{A}{K\nu}\exp\left(-\frac{c}{F_t - F_S} - \frac{A}{K\nu}\left(\exp\left(-\frac{c}{F_t - F_S}\right)(F_t - F_S) - c\,\mathrm{Ei}\left(\frac{c}{F_t - F_S}\right)\right)\right) \tag{1.4}$$

$$\mathrm{Ei}(x) = \int_x^\infty e^{-t}/t \, dt$$

If the rupture force is measured hundreds of times, it is possible to plot in histograms the number of times a specific force value was measured. Fitting the experimentally obtained threshold yield distribution with Equation 1.4, it is possible to link macroscopically observed quantities, like the pierce-through force, to microscopic properties of the film, like the line tension Γ. A practical application will be presented in chapter 4 of this thesis.

1.5 References

(1) Binnig, G., and Rohrer, H., **1983**, *Surface Science* 12, 236-244.
(2) Binnig, G., and Smith, D., **1986**, *Rev. Sci. Instrum.* 57, 1688-1689.
(3) Binnig, G., Quate, C. F., and Gerber, C., **1986**, *Phys. Rev. Letts.* 56, 930-933.
(4) Boisen, A., Hansen, O., and Bouwstra, S., **1996**, *J. Micromech. Microeng.* 6, 58-62.
(5) Baselt, D. R., Clark, S. M., Youngquist, M. G., Spence, C. F., and Baldeschwieler, J. D., **1993**, *Rev. Sci. Instrum.* 64, 1874-1882.
(6) Taylor, M. E., **1993**, *Rev. Sci. Instrum.* 64, 154-158.
(7) Müller, D.J. and Engel, A,. **1997**, *Biophys J*, 73, 1633-1644.
(8) Butt, H. J., **1991**, *Biophys. J.* 60, 1438-1444.
(9) Müller, D.J., Fotiadis, D., Scheuring, S., Müller, S.A. and Engel, A., **1999**, *Biophys. J.*, 76, 1101-1111.)
(10) Pierce, M. L., Stuart, J. K., Pungor, A., Dryden, P., and Hlady, V., **1994**, *Langmuir* 10, 3217.
(11) Weisenhorn, A. L., Khorsandi, M., Kasas, S., Gotzos, V., and Butt, H. J., **1993**, *Nanotechnology* 4, 106-113.
(12) Zhong, Q., Inniss, D., Kjoller, K., and Elings, V. B., **1993**, *Surface Science* 290, 688-692.
(13) Meyer, E., Hug, H. J., and Bennewitz, R., **2004**, Scanning Probe Microscopy. The lab on a tip, Springer-Verlag.).
(14) Evans, E., **2001**, *Annu. Rev. Biophys. Biomol. Struct.*, 30, 105-128.
(15) Butt H. J., Cappella B., and Kappl M., **2005**, *Surface Science Reports* 59, 1-152.
(16) Chiantia S., Ries J., Kahya N., and Schwille P. **2006**, *Chemphyschem,* 13, 2409.
(17) Garcia-Saez A. J., Chiantia S., Salgado J, and Schwille P. **2007**, *Biophys. J.,* 93, 103-112
(18) Burgess I., Jeffrey C. A., Cai X., Szymanski G., Galus Z., and Lipkowski J., **1999**, *Langmuir* 15, 2607
(19) Butt, H. J., and V. Franz. **2002**, *Phys. Rev.* 66: 031601-1–031601-9.
(20) Morris, V. J., Kirby, A. R., and Gunning A. P., Atomic Force Microscopy for Biologists, **1999**, Imperial College Press, London.

Chapter 2 – Introduction to Fluorescence Correlation Spectroscopy

2.1 Introduction

Fluorescence correlation spectroscopy (FCS) is an experimental technique with single-molecule sensitivity which was introduced more that 30 years ago (1). Differently from bulk techniques, which report only general information on the heterogeneous character of the sample, FCS is based on the study of the fluorescence signal detected from a very small portion of the sample. Fluorescence intensity fluctuations can occur in a fluid sample at thermal equilibrium. Monitoring the fluctuations as a function of time, a simple mathematical analysis provides information about the average number of molecules in the focal volume and the dynamical properties of the processes giving rise to the fluorescence fluctuations. Possible applications include: determination of local concentrations (2), diffusion of molecules (3), photophysical and photochemical reactions (4,5), binding and reaction kinetics (6,7).

Compared to single particle tracking (SPT) (8), which also monitors the diffusion of single fluorescent molecules, FCS is more versatile and less time-consuming. A simpler method to study diffusion of fluorescent molecules is fluorescence recovery after photobleaching (FRAP) (9), which nevertheless requires heavy-loaded labeling of the sample and high laser power. On the other hand, FCS is less invasive and requires a much smaller concentration of fluorophores and lower excitation power. These features are particularly important in delicate systems, like lipid membranes, whose dynamic and structural properties can be easily perturbed by the presence of fluorescent contaminant or by laser induced heating.

2.2 Theory of FCS

In FCS, the excitation light is focused to a diffraction limited spot (10). Fluorescent molecules in solution move through the focal volume because of Brownian motion. Furthermore, they can also undergo transitions between electronic states with different quantum yields. These two processes cause fluctuations of the fluorescence signal collected from the molecules in the focal volume. The temporal autocorrelation function measures the self-similarity of the signal in time. This quantity depends on how long a molecule will be in the same state and in the focal volume, and decays with time. The decay time and the shape of the autocorrelation function provide information about the mechanisms giving rise to the signal fluctuations. We call *F(t)* the fluorescence signal collected from the detection volume as a function of time. The fluctuation of the signal is denoted by δF(t) and is defined as:

$$\delta F(t)=F(t)-\langle F\rangle \tag{2.1}$$

where <F> is the fluorescent intensity time average. The autocorrelation function $G(\tau)$ is defined as:

$$G(\tau)=\frac{\langle \delta F(t+\tau)\delta F(t)\rangle}{\langle \mathrm{F(t)}\rangle^2}=\frac{\langle \delta F(\tau)\delta F(0)\rangle}{\langle \mathrm{F}\rangle^2} \tag{2.2}$$

The second equivalence is true for stationary samples. The fluorescent signal from different molecules can be considered completely uncorrelated, because of the random time separating the excitation and the emission of a fluorescent molecule. The fluorescence intensity detected from a volume element in position ***r*** at time *t* is proportional to the position-dependent

excitation profile *I(**r**)*, the concentration of the fluorophores *c(**r**,t)*, their fluorescence quantum yield $\eta(t)$, their excitation cross-section σ_{exc}, the overall fluorescence detection efficiency for the fluorophore *E* and the normalized fluorescence collection efficiency *Y*. Furthermore, in case of polarized excitation and/or detection, the fluorescence signal depends also on the orientation of the absorbing/emitting dipole moments. Neglecting this last rotational term,

$$F(t) = \int W(\mathbf{r}) q(t) c(\mathbf{r},t) dV \tag{2.3}$$

where $W(\mathbf{r})=Y(\mathbf{r})I(\mathbf{r})/I_{max}$ describes the effective shape of the fluorescence detection volume and $q(t)= I_{max}\, E\, \sigma_{exc}\, \eta(t)$ is the molecular brightness of the fluorophore.

Let us consider a two-dimensional sample of infinite extent, illuminated by a laser beam with a Gaussian intensity profile. Then

$$W(\mathbf{r}) = W_0 e^{-\frac{2(x^2+y^2)}{w_0^2}} \tag{2.4}$$

where w_0 indicates the spatial extension of the focused beam and I_0 is a constant.

In a first approximation, we can consider all the parameters constant (i.e. $q(t)=q$) and assume that the only cause of fluctuations in fluorescence signal is fluctuations in the concentration of fluorophores at position **r** and time *t* from the average value $\langle c \rangle$. In this case we can write:

$$\langle F \rangle = q \langle c \rangle \int W(\mathbf{r}) dV \tag{2.5}$$

$$\delta F(t) = q \int W(\mathbf{r}) \delta c(\mathbf{r},t) dV \tag{2.6}$$

The normalized autocorrelation function can thus be written as:

$$G(\tau) = \frac{\iint W(\mathbf{r}) W(\mathbf{r}') f(\mathbf{r},\mathbf{r}',\tau) dV dV'}{\left[\langle c \rangle \int W(\mathbf{r}) dV\right]^2} \tag{2.7}$$

with

$$f(\mathbf{r},\mathbf{r}',\tau) = \langle \delta c(\mathbf{r}', t+\tau) \delta c(\mathbf{r},t) \rangle = \langle \delta c(\mathbf{r}',\tau) \delta c(\mathbf{r},0) \rangle \tag{2.8}$$

Equation 2.8 is the correlation function of a concentration fluctuation at position **r** with a concentration fluctuation at position **r′** and time τ and it holds true if the sample is stationary.

For non-interacting solutes, concentration fluctuations are correlated in the same instant only in the same position, i.e.:

$$f(\mathbf{r},\mathbf{r}',0) = \langle c \rangle \delta(\mathbf{r}-\mathbf{r}') \tag{2.9}$$

where δ is the Dirac delta function. According to equation 2.7 and 2.9, the amplitude *G(0)* of the correlation curve is inversely proportional to the concentration of fluorescent molecules in solution:

$$G(0) = \frac{1}{\langle c \rangle} \frac{\left[\int W(\mathbf{r}) dV\right]^2}{\int W(\mathbf{r})^2 dV} \tag{2.10}$$

. It is thus possible to define the number of molecules in the focal volume as

$$G(0) = \frac{1}{N} \tag{2.11}$$

and an effective volume V_{eff} so that:

$$V_{eff} = \frac{\left[\int W(\mathbf{r}) dV\right]^2}{\int W(\mathbf{r})^2 dV} \tag{2.12}$$

From Equations 2.10, 2.11 and 2.12, it results $N = c \cdot V_{eff}$.

The analysis of the temporal decay of the correlation curve provides information about the dynamical process causing the fluorescence fluctuations. For the experiments described in this

thesis, it is possible to assume that the fluorescent signal fluctuates only because of two-dimensional diffusion of fluorescent molecules in and out of focus. Combining the description of the detection volume, the definition of the correlation function and a model that accounts for the concentration fluctuations, the autocorrelation function can be written (12):

$$G(\tau) = \frac{1}{N} \frac{1}{1 + \frac{\tau}{\tau_D}} \tag{2.13}$$

where τ_D is the so-called diffusion time and is related to the diffusion coefficient D according to: $\tau_D = w_0^2/4D$. The diffusion time of a fluorescent molecule can be thus easily obtained by fitting the experimental correlation curves. Independent measurements of the waist w_0 are critical for determining absolute diffusion coefficients but they often result in imprecise estimations of D (11). Absolute diffusion coefficients can also be determined, independently of any calibration method, using variations of "classic" FCS, namely: z-scan method, 2-focus FCS and scanning FCS. These methods are described in section 2.4 of this thesis. The general expression of Equation 2.13 for multiple optical diffusing species, with different quantum yields or brightness is:

$$G(\tau) = \frac{\gamma \sum_{i=1}^{R} q_i^2 \langle N_i \rangle \left[1 + \frac{\tau}{\tau_{D,i}} \right]^{-1}}{\left[\sum_{i=1}^{R} q_i \langle N_i \rangle \right]^2} \tag{2.14}$$

where each τ_{Di} is equal to $w_0^2/4D_i$. It is worth noting that, in the case of multiple diffusing species, the amplitude of the correlation curve depends on the average of the particle number, weighted on their relative quantum yield.

In the case of three-dimensional diffusion, Equations 2.13 and 2.14 are not valid anymore because the focal volume is no longer approximated by Equation 2.4. Nevertheless, in almost every FCS setup normally used, the focal volume can also be limited in the z-direction by using confocal geometry (see next paragraph). If a pinhole is placed in front of the detector, out-of-plane light can not be measured anymore and the laser focus profile can be approximated by a three-dimensional Gaussian. Within this simple approximation, Equation 2.13 would become:

$$G(\tau) = \frac{1}{N} \frac{1}{1 + \frac{\tau}{\tau_D}} \bullet \frac{1}{\left(1 + \frac{\tau}{SP^2 \tau_D} \right)^{1/2}} \tag{2.15}$$

where $SP = z_0/w_0$ is the "structure parameter", and z_0 is the width of the Gaussian curve describing the z-extension of the focal volume.

It is important to stress that Equations 2.13, 2.14, and 2.15 are valid if the signal fluctuations are solely due to Brownian diffusion of fluorescent molecules through the focal volume. Of course, in more complex systems, there might be different sources of signal fluctuations, like chemical reactions, rotational diffusion, triplet blinking and so on (for a review, see Ref 12). These contributions are nevertheless not important for the experiments described in this thesis.

2.3 Experimental setup

As already mentioned in the previous paragraph, FCS is based on the detection of the fluorescence signal from a very small open volume. The dimensions of the observation volume are important in determining the amplitude of the fluctuations with respect to the overall fluorescence signal. Also because of this reason, the real breakthrough of this technique was when Rigler et al. (13) used the confocal geometry to confine the detection volume in all three dimensions, finally reaching single-molecule sensitivity and dramatically increasing the signal-to-noise ratio. While confinement of the volume in the x-y direction could already be easily accomplished focusing the laser light with a high numerical-aperture objective, the additional confinement in the z-direction provided by a pinhole strongly reduced the out-of-focus background signal.

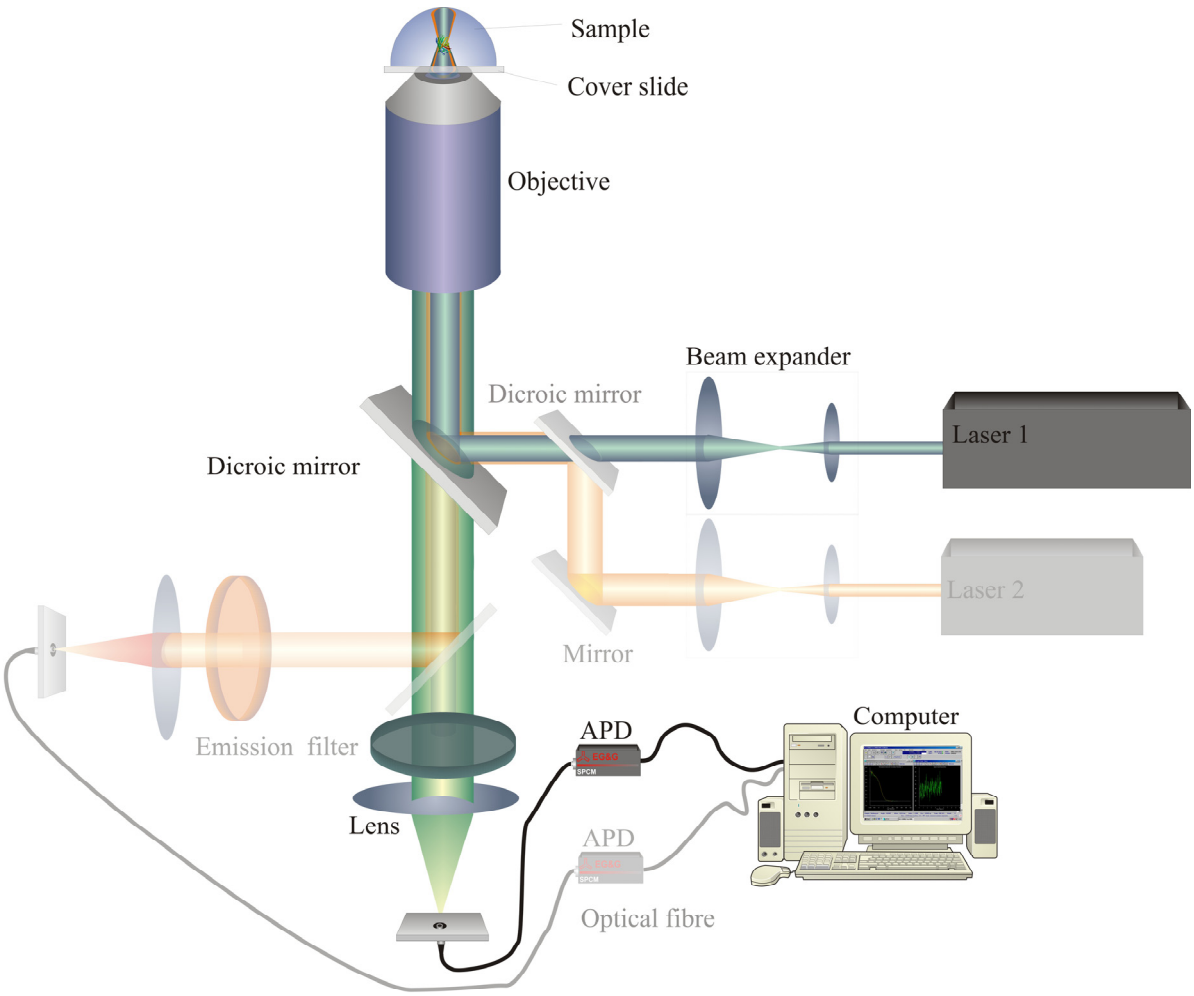

Figure 2.1 *Setup for a FCS experiment. A laser beam is reflected by a dichroic mirror and focused by a microscope objective into the sample. Fluorescence light is collected by the same objective. Residual excitation light is removed by a band-pass filter before the light is directed onto the detectors. The fluorescence signals are hardware-correlated by a commercial PC card. The elements drawn in lighter colors are needed to perform a FCCS experiment (see text). Adapted from Haustein et al. (14).*

Figure 2.1 illustrates a typical FCS apparatus. The excitation light from a laser source (Laser 1) is reflected by a dichroic mirror and focused on the sample by the objective, through which a diffraction-limited illumination is achieved. In order to obtain a small focal volume and to collect as many photons as possible, high numerical-aperture objectives must be used. The fluorescence signal is collected back through the same optical path and is transmitted through the dichroic mirror. After passing through an emission filter, the light is focused on an optical fiber connected to an avalanche photodiode (APD). The optical fiber itself acts as a pinhole and provides a slicing of the sample along the optical axis. The light that does not originate from the focal plane, in fact, is focused outside the pinhole and cannot reach the detector. Finally the signal is elaborated by a hardware or software correlator. In case two optical species (with different absorption and/or emission spectra) are studied at the same time, a second laser line (Laser 2) and a different detection pathway can be used. It is then possible to cross-correlate the signal (dual color Fluorescence Cross-correlation Spectroscopy, dcFCCS) from the two detectors to obtain useful information about the interactions between the different molecular species (see Haustein et al. (14) for a review).

With very small changes, the same experimental apparatus and the same optical paths can be used to perform Laser Scanning Microscopy (LSM) imaging. The focal volume is scanned through the sample in the x-y plane using mirrors and the signal is measured by APDs or photomultipliers (PMT). For each portion of the sample (corresponding to a pixel of the final image) the average fluorescent intensity is recorded and displayed. Thanks to the confocal geometry, the same procedure can be repeated at different z-positions and the acquired optical slices can be eventually reassembled together via software to obtain a three-dimensional reconstruction of the sample.

In this thesis, all the experiments regarding fluorescence imaging were performed using a Zeiss (Jena, Germany) inverted microscope equipped with a META 510 scanning unit. FCS measurements were performed using a home-built setup coupled to the fiber output of the LSM scanning unit. A more detailed description of the experimental apparatus is presented for each experiment in chapters 4, 5, 6, 7, and 8.

2.4 Z-scan method, Two-focus FCS and Scanning FCS

In order to extract absolute values for diffusion coefficients and concentrations from the analysis of fluorescence temporal fluctuations, it is necessary to know the exact dimension of the detection volume. The most common method to calibrate the FCS apparatus is to measure the diffusion time of a fluorescent molecule with known diffusion coefficient. Unfortunately, it is hard to find such a reliable standard (12) and, furthermore, these calibration measurements must be performed in the exact same conditions of the actual experiment. If not so, even very small changes in the refraction index of the used media, temperature, or in the thickness of the support between the sample and the objective can affect the shape of the focal volume and the diffusion time measurements (11). Additionally, this calibration method and the determination of its parameters w_0 and SP –i.e. waist and structure parameter- rely on the three-dimensional Gaussian approximation of focal volume shape. In case of application to two-dimensional diffusion measurements (e.g. in planar lipid membranes), this could result in a systematic error due to the fact that the Gaussian shape of the focal volume is anyway a poor approximation (12) and the geometry of its intersection with the plane of the membrane exhibits strong dependence from the z position.

Alternatively, if these deviations are taken into account, it is possible to perform absolute measurements in membranes using the so-called “z-scan method” (15). If the sample consists only of a fluorescently-labeled planar membrane, the effective detection volume can be

considered as the intersection between the plane of the membrane and the focal volume. Differently from what one would expect from the three-dimensional Gaussian approximation of the focal volume, this surface changes as a function of the distance Δz between the focus and the membrane. In particular, due to the widening of the focal volume's cross sections far from the center, the measured number of particles and their diffusion time should grow with Δz, according to:

$$\tau_D = \frac{w_0^2}{4D}\left(1 + \frac{\lambda_0^2 \Delta z^2}{\pi^2 n^2 w_0^4}\right) \tag{2.16}$$

$$N = \pi c w_0^2 \left(1 + \frac{\lambda_0^2 \Delta z^2}{\pi^2 n^2 w_0^4}\right) \tag{2.17}$$

where w_0 is the radius of the beam in the focal plane, D is the lateral diffusion coefficient, c is the average concentration of diffusing fluorescence molecules in the illuminated area, n is the refractive index of the medium, λ is the wavelength of the excitation light, and Δz is the distance between the sample position z_0 and the position of the beam diameter minimum z. If autocorrelation functions are acquired at different heights with respect to the plane of the membrane, the obtained parameters N and τ_D can be fit using Equations 2.16 and 2.17. This procedure directly yields: the diffusion coefficient D, the waist w_0 and the concentration of fluorophores c. Compared to the three-dimensional focal volume calibration method described above, the z-scan method has two advantages: (a) it does not suffer from systematic errors introduced by inaccurate positioning of the focus with respect to the plane of the membrane and (b) it determines directly the lateral diffusion coefficient D without any need for calibration measurements using an external standard.

Apart from the z-scan, there are other methods which allow FCS measurements without need for external calibration. Dertinger et al. (16), for example, used two partially overlapping but still distinct excitation volumes. The signal from the two foci was then cross-correlated to obtain the average time needed by the fluorophores to move from one focus to the other. Knowing the exact geometry of the double excitation volume, the obtained time can be converted in an absolute diffusion coefficient. Like in the case of the z-scan method, two-focus FCS does not need any external calibration apart from the measurement of the distance between the two foci. The same principle was applied by Ries and Schwille (17), who used a laser scanning microscope to measure fluorescence signal from two parallel lines scanned perpendicularly to vertical membranes of large lipid vesicles or cells. The two intersections between each of the scanned line and the membrane can be considered as two effective excitation volumes. The signal from these two volumes can be then cross-correlated to obtain again an absolute diffusion coefficient. The same approach can be used also if the scanned lines and the membrane lay parallel to each other (18, see chapter 4 for more details).

This last two-focus FCS variation belongs to the larger group of scanning FCS methods, where the volume is somehow moved with respect to the sample in a periodic fashion (19). Scanning FCS has in general several advantages over standard FCS, e.g.: it can improve statistical accuracy by measuring the autocorrelation function in several independent volumes during the same scan (20), it does not need external calibration if the geometry and the speed of the scanning are known (21), it decreases the photobleaching, and can measure the dynamics of slowly-diffusing or even immobile molecules (22). These last two features are particularly important if, for example, the lateral organization of receptors in highly viscous cell membranes are to be studied. This approach was used for the first time in the work described in this thesis and is described in chapter 8.

2.5 References

(1) Magde D., Elson E., and Webb W. W. 1972, Phys. Rev. Lett. 29, 705-708.

(2) Wright L. L., Palmer A. G., and Thompson N. L., 1989, Mat. Res. Soc. Symp. Proc. 111, 419-424.

(3) Koppel, D. E., Axelrod D., Barak L. S., Wolf D. E., Elson E. L. and Webb W. W., 1976, Biophys. J. 16, 1315-1329.

(4) Heikal A. A., Hess S. T., and Webb W. W., 2001, Chem. Phys. 274, 37-55.

(5) Schwille P., Kummer S., Heikal A. A., Moerner W. E., and Webb W. W., 2000, Proc. Natl. Acad. Sci. USA 97, 151-156.

(6) Schwille P., Bieschke J., and Oehlenschlager F., 1997, Biophys. Chem. 66, 211-228.

(7) Heinze K. G., Rarbach M., Jahnz M., and Schwille P., 2002, Biophys. J. 83, 1671-1681.

(8) Saxton M. J., 1997, Biophys. J. 72, 1744-1753.

(9) Axelrod D., Koppel D. E., Schlessinger J., Elson E., and Webb W. W., 1976, Biophys. J. 16, 1055-1069.

(10) Born M., and Wolf E., 1997, Principles of optics: electromagnetic theory of propagation, interference and diffraction of light, Cambridge University press, Cambridge.

(11) Enderlein J., Gregor I., Patra D., Dertinger T., and Kaupp U. B., 2005, Chemphyschem, 6:2324-2336

(12) Petrov E., and Schwille P., 2008, Standardization in Fluorometry: State of the Art and Future Challenges; Resch-Genger, U., Ed.; Springer: Berlin, in press

(13) R. Rigler and J. Widengren *Bioscience* **3** (1990), pp. 180–183

(14) Haustein E., and Schwille P., 2003, Methods, 29:153-166.

(15) Benda A., Benes M., Marecek V., Lhotsky A., Hermens W. T., and Hof M., 2003, Langmuir, 19:4120-4126.

(16) Dertinger T., Pacheco V., von der Hocht I., Hartmann R., Gregor I., and Enderlein J., 2007, Chemphyschem, 8:433–443.

(17) Ries J., and Schwille P., 2006, Biophys. J., 91:1915–1924.

(18) Chiantia S., Ries J., Kahya N., and Schwille P., Chemphyschem, 7:2409-2418.

(19) Petrásek Z., and Schwille P., 2007, Single Molecules and Nanotechnology, Springer, Volume 12.

(20) Weissman M., Schindler H., and Feher G., 1976, Proc. Natl. Acad. Sci., 73:2776-2780.

(21) Petrásek Z., and Schwille P., 2007, Biophys. J., 10.1529

(22) Chiantia S., Ries J., G., Carrer D., Li Z., Bittman R., Schwille P., 2007, Biochim. et Biophys. Acta, submitted

(23) Kahya N., 2003, Lipid and protein dynamics in model membranes, PhD Thesis.

Chapter 3 – Biological membranes, lipid domains and model membranes

3.1 Cell membranes and lipid domains

Biological cells are distinguished and physically separated from the external environment by the presence of a lipid membrane. Eukaryotic cells, in addition, contain several internal membranes that constitute specialized compartments where specific biochemical reactions are isolated. Far from being mere physical confinements, membranes have a multitude of complex functions. Through the action of membrane-embedded channels and transporters, or through membrane fission and fusion, biological membranes can control the flux of energy and matter between the cell and the external medium. In the same way, also the exchange of information and cell-cell communication are regulated at the level of the membrane: signal transduction is performed for example by receptors undergoing changes in conformation and in spatial organization. Furthermore, cell membranes also host different enzymes catalyzing biochemical reactions and participate in mechanical processes involving the whole cell, like motility and growth of tubular structures (1).

From a molecular point of view, cell membranes are constituted by a fluid double layer of anphipatic molecules called (phospho)lipids and a number of membrane proteins that are associated to the bilayer to different extents (2). Lipids are organized so that their hydrophobic moieties face the interior of the bilayer, while their hydrophilic parts constitute the surfaces of the layer, either facing the extra- or the intra-cellular water environment. In this two-dimensional fluid, molecules exchange slowly between leaflets but are mobile within the leaflets. Phospholipids are derived either from a glycerol (glycerophospholipids) or a sphingosine (sphingolipids) backbone.

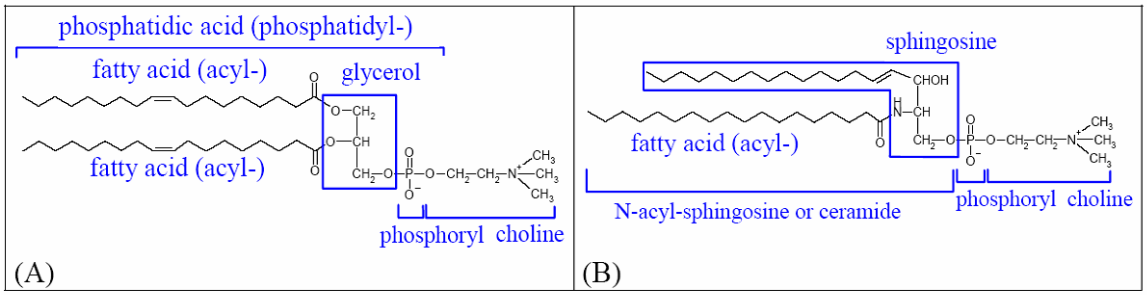

Figure 3.1 *Schematic representation of a glycerophospholipid (i.e. dioleoyl-phosphatidylcholine, panel A) and a sphingolipid (stearoyl-SM, panel B). From ref. (3).*

Glycerophospholipids have two fatty acids esterified to the first two carbons of the glycerol. The third carbon is esterified to a phosphoric acid group which is, in turn, esterified to an alcohol, e.g. ethanolamine (phosphatidylethanolamine, PE), choline (phosphatidylcholine, PC), serine (phosphatidylserine, PS) or inositol (phosphatidylinositol, PI). Sphingolipids have a sphingosine backbone that already contains a long saturated hydrocarbon chain and it is again ester-linked to a fatty acid. Very common sphingolipids are: ceramide (Cer), which consists exclusively of the sphingosine backbone and the ester-linked fatty acid; sphingomyelin (SM), in which the sphingosine is esterified to a phosphoric group linked to a

choline; gangliosides, like G_{M1}, in which the sphingosine is linked to a ramified polysaccharide moiety. Another molecule which is found in almost all eukaryotic membranes is cholesterol (4). Cholesterol is the most common and studied sterol in animal cells, as its concentration in plant cells is very low. Other sterols can play similar roles in different organisms, like the case of ergosterol in yeast. The planar structure of this molecule allows favorable van der Waals interactions with the lipid chains of phospholipids and its hydroxyl group can establish hydrogen bonds with their polar heads. Additionally, cholesterol is involved in the production of bile salts and steroid hormones, like androgens, estrogens, and glucocorticoids (2).

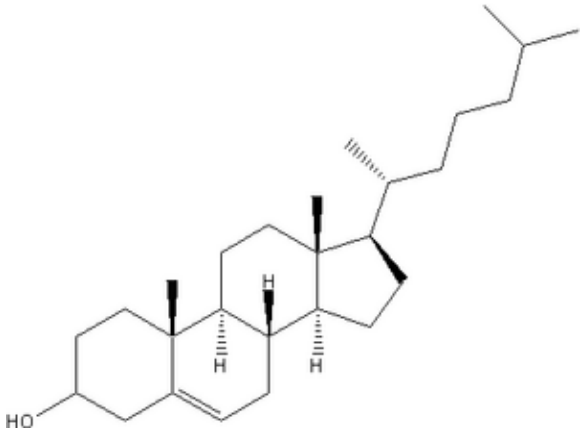

Figure 3.2 *Molecular structure of cholesterol. From www.worldofmolecules.com*

The exact lipid composition in natural membranes depends on the cell type and membrane location. For example, the weight percentages of glycerophospholipids, sphingomyelin and cholesterol range from ca. 50, 20 and 20% respectively in human erythrocyte membranes, to 40, 7 and 8% in liver Golgi membranes (5).

Apart from lipids, the other main components of cell membranes are proteins. Membrane proteins can be inserted in the membrane exposing hydrophobic residues to the lipid chains, either through the whole bilayer, or only in one leaflet. Alternatively, they can be inserted through lipid anchors like fatty acids (e.g. palmitic acid), prenyl groups (e.g geranyl-geranyl) or C-terminally linked glycolipids (e.g. glycosyl-phosphatidyl-inositol (GPI) anchor). Finally, a protein can be attached to the membrane via non-covalent interactions with the polar heads of lipid or with other proteins (6,7).

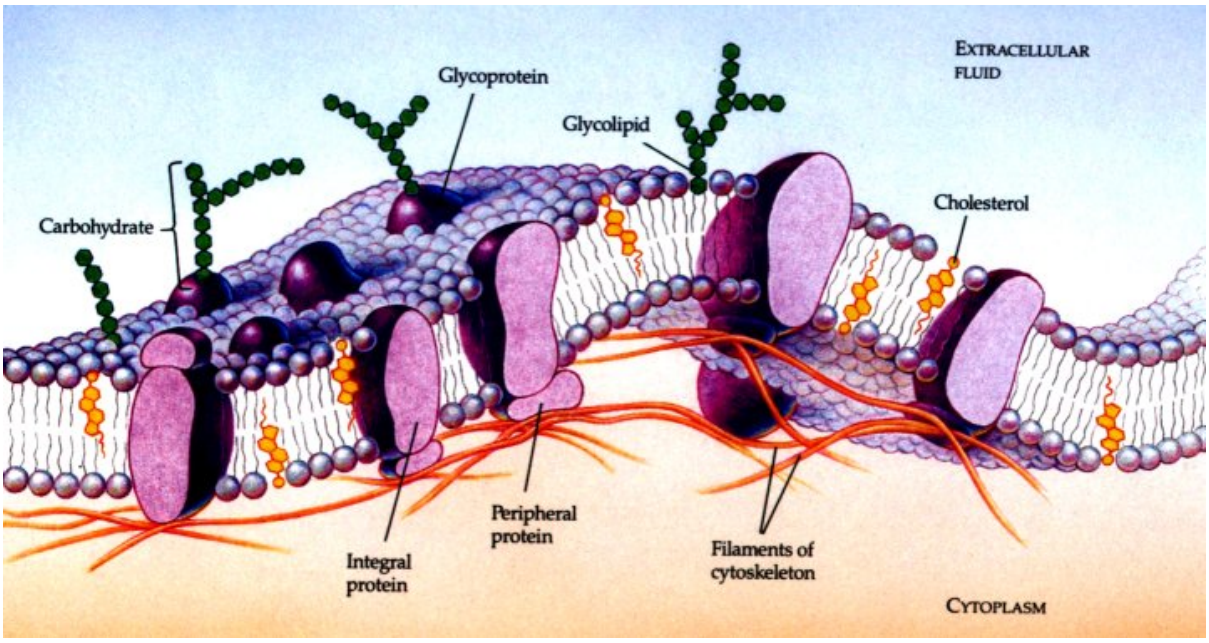

Figure 3.3 *Fluid mosaic model. The membrane is a two-dimensional fluid in which proteins are solved and can diffuse freely (8). From med.tn.tudelft.nl.*

According to the fluid mosaic model (8), all lipid and proteins are mixed together to form a homogenous two-dimensional fluid. This so-called "fluid mosaic model" was based on the observation that most of the lipids in natural membranes exist in a liquid state at physiological temperature. However, this model cannot be entirely accurate because cell membranes contain a considerable amount of lipids, such as the long-chain saturated sphingolipids described above, which exhibit the tendency to form a solid state at 37°C. Furthermore, the lipid bilayer of eukaryotic cell membranes is asymmetric, the outer –exoplasmic- leaflet being enriched in PC and the inner leaflet enriched in PS and PE. Also, sphingolipids are mostly localized in the outer leaflet while sterols are present in both leaflets. Similarly, an uneven distribution of sphingolipids and glycerophospholipids is usually observed among different cellular organelles, the plasma membrane being for example enriched in SM and glycosphingolipids (9). In contrast with the hypothesis of a simple homogenous fluid, recent evidences have shown that lipids are heterogeneously arranged in the plane of the membrane. For example, caveolae –small invaginations in the plasma membrane- are enriched in glycosphingolipids (10). One key finding regarding the existence of lipid-driven phase separation was the selective co-clustering of some membrane components and the segregation from others, as response to antibody application to living cells. In particular, it was shown that antibody-mediated clustering of a specific ganglioside caused capping and that another ganglioside redistributed inside the cap (11). In general, simultaneous addition of two antibodies against different homogenously distributed surface antigens could lead to either co-clustering or to their segregation (12). These findings were interpreted postulating that certain proteins reside in small ordered lipid domains, below the light resolution in size, while other proteins are excluded from them. Upon clustering using antibodies, these small domains coalesce into large stable platforms that contain several specific proteins. The antigens that were initially excluded from the ordered environment are also excluded from these large domains and form spatially separated clusters. Further support to this hypothesis came from the observation that cell membranes are differentially susceptible to extraction by detergents like Triton X-100 at 4°C, with some components being completely solubilized while other lipid and proteins forming so called "detergent resistant membranes" (DRM (13)). This finding suggested that cell membranes contained in fact microdomains where lipid and proteins were more tightly

packed and thus less accessible to the detergent. These lipid assemblies were called “rafts” and were described as enriched in cholesterol, sphingolipids and a certain subset of membrane proteins (14). The core of the raft concept is that cell membranes can phase separate into different domains and that this is a lipid-driven process. Nevertheless, it is now widely accepted that DRMs have not a specific *in vivo* correlate, because they are formed during the detergent treatment (15). Also for this reason, the raft hypothesis is currently under debate (16). In spite of the different biophysical methods so far used to investigate the existence of such domains in cell membranes, only indirect evidences have been presented. Experiments with environment-sensitive fluorescent probes like LAURDAN and DPH-PC, showed the existence of ordered domains in living cell membranes (17,18). Other experiments using single molecule tracking (SMT) (19), electron microscopy (20) (EM) and fluorescence resonance energy transfer (FRET) (21) reached inconclusive results regards the dimension of rafts. The difficulties encountered in trying to visualize microdomains *in vivo*, have led to alternative explanations describing rafts as very small (less than 20 nm) dynamical protein-driven entities. Such molecular complexes would coalesce only following stimulation and clustering (22,23). In conclusion, while the steady-state existence, size and shape of ordered domains in living cell is still subject of debate, agreement has been reached on the fact that native cell membranes can exhibit phase separated domains and that such domains coalesce upon cross-linking to form signalling and sorting platforms (24). This view comes mainly from the co-clustering data (12), the visualization of ordered domains in living cells (18) and from the variety of data about phase separation in model membranes (see next paragraph).

3.2 Phase separation in model membranes

Lipids can exist in a variety of phases and three-dimensional structures. In this thesis, we will focus on lamellar (bilayer) phases. (1,5).

At low temperature, the hydrocarbon chains are as extended as possible, with all the single C-C bonds in the all-trans configuration, thus maximizing van der Waals interactions (high configurational order of the lipids). The bilayer is also characterized by a long-range translational order, impeding lateral movements of the membrane components. This phase is called gel (L_β, $L_{\beta'}$ or $L_{\beta I}$ depending on the exact three-dimensional chain configuration) or, more simply, solid ordered (s_o) phase.

If the temperature is increased above a melting point T_m, the gel phase becomes the so-called liquid-crystalline phase (L_α). This lipid phase is characterized by both low configurational and translational order. In other words, the carbon chains increase the amount of cis bonds, thus resulting in short-range internal order and free diffusion of membrane components. For these reasons, the L_α phase has been recently named liquid-disordered phase (L_d) (25).

The addition of sterols has the effect of broadening the temperature range in which the transition between s_o and L_d phases takes place. The loss of cooperativity in the transitions was explained with the introduction of a new equilibrium phase identified via NMR studies: (26) the liquid-ordered phase (L_o). This lipid phase is characterized by high configurational order and low translational order being, in fact, an intermediate between the L_α and the L_β phases. Interestingly, the L_o phase was never found in single lipid systems.

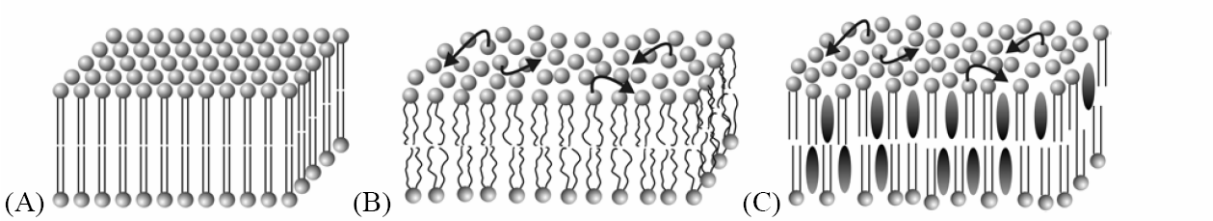

Figure 3.4 *Schematic representations of different lamellar phases: A) gel, solid-ordered phase; B) liquid-crystalline phase; C) liquid-ordered phase. The lipids´ polar heads are represented by spheres, the lipid chains by lines. Ovals represent cholesterol molecules. From Ref. 3.*

In the case of complex eukaryotic membranes containing cholesterol and a multitude of different lipids, it is difficult to monitor the characteristics and the transitions among the different phases. Nevertheless, studying simple systems with identifiable phases might give further insight into phenomena that could be present in real cell membranes, like local formation of ordered domains (rafts), partition of membrane components and "local lipid melting" in the vicinity of membrane proteins. For this reason, various model membrane systems have been used to study phase separation in lipid mixtures.

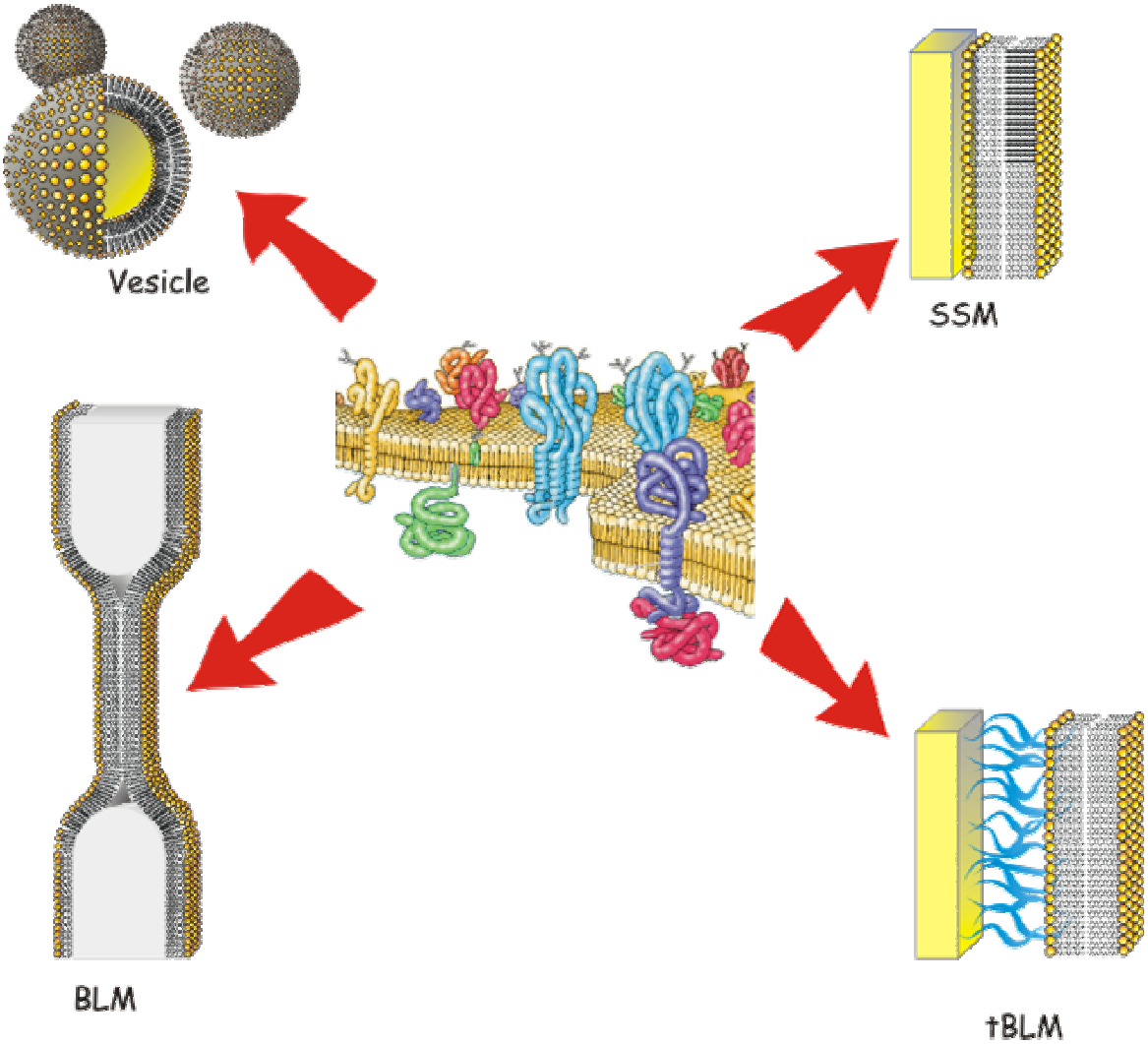

Figure 3.5 *Different model membranes: vesicles, solid supported membranes (SSM), tethered bilayer lipid membrane (tBLM), black lipid membranes (BLM). From mpip-mainz.mpg.de.*

Vesicles, or liposomes, are closed bilayers in which the hydrophilic part of the membrane faces the water environment both outside and in the inner core (27). They can be constituted of a single bilayer (unilamellar) or more than one, in an onion-like structure (multilamellar vesicles, MLV). Unilamellar vesicles are distinguished based on size, from small unilamellar vesicles (SUV) with a radius of few nm to giant unilamellar vesicles (GUV) with radius of several micrometers. Liposomes can be obtained in several ways. Most often, simple rehydration of a dry lipid film will produce MLVs. Through extrusion with size-defined pores, freeze-thaw cycles or sonication, MLVs are transformed in unilamellar vesicles (see chapter 5). SUVs can be easily obtained simply via sonication, but their curvature is extremely high and most of the lipids are in the outer leaflet. GUVs, on the other side, have a curvature which resembles more that of a cell membrane but are more complex to produce. In this case, the electroformation method is usually used (see chapter 6). If membrane proteins are to be reconstituted in the bilayer, detergents have to be included in the preparation procedure and, eventually, removed by gel filtration or dialysis (see chapters 4 and 8).

SUVs can also adhere and spontaneously fuse on a solid hydrophilic support, like glass or mica, to produce a continuous planar membrane (solid supported bilayer SSB or supported lipid bilayer SLB) (28). While the preparation procedures are relatively simple and these model membranes are stable for long time, the presence of the solid support might affect the structural and dynamic properties of the lipids and proteins. The spacing between the membrane and the support is usually 1-2 nm, but this could be increased using polymer spacers (tethered bilayer lipid membranes, tBLM). This procedure might decouple the lipid bilayer from the influence of the support. More details are presented in chapter 4 of this thesis.

As an alternative to solid supports, lipid monolayers can be prepared at the interface between water and air or water and organic solvent (29). Also in these systems, the lipids are all aligned with the polar heads facing the water phase. The lipid composition and important physical parameters like the lateral pressure can be easily controlled (29). Their ability to mimic biomembranes, though, can be questioned as they lack the second leaflet to form a bilayer.

Finally black lipid membranes (BLM) are obtained by using a small aperture (100-200 micrometers) in a thin partition (septum) between two aqueous containers (30.). An organic solution of lipids is brushed over the hole and then the compartments are filled with water. For good BLMs, measuring the light reflected on the septum will result in the observation of a black spot. Although the lipid composition of the different leaflets can be easily controlled, this method will yield unstable bilayers making equilibrium studies or protein reconstitution more difficult.

Depending on the specific model membrane, different methods can be used to investigate lipid phase separation. For example, SUVs dimensions are below the optical resolution and are typically used in bulk measurements, like fluorescence anisotropy, FRET or fluorescence quenching (31). Nuclear magnetic resonance (NMR) and differential scanning calorimetry (DSC) can also be successfully used in small vesicles to study lipid organization (33,34). Conversely, SLB and GUVs are more appropriate for optical investigation like confocal laser scanning microscopy (LSM), FRAP or fluorescence correlation spectroscopy (FCS). Supported bilayers have also the additional advantage of being suitable for surface techniques like scanning near field optical microscopy (SNOM) (34) or AFM. It is worth noting that there is a direct connection between phase separation and the topography of the bilayer visualized via AFM, as the thickness of a membrane depends on the degree of conformational order of the acyl chains.

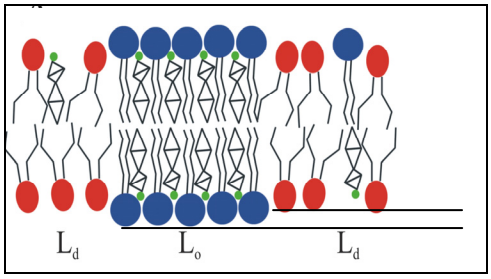

Figure 3.6 *Schematic model for L_d/L_o phase separation. The lipid molecules represented are: DOPC (red), SM (dark blue), cholesterol (green). The distance between the two solid lines is ca. 7 Å.*

For this reason, the work described in this thesis is based mostly on the use of SSMs. The advantages deriving from the combined use of fluorescence microscopy and AFM on SLBs will be described in the next chapter of this thesis.

The basic principles of lipid phase separation were established with binary mixtures but, recently, also ternary mixtures, more closely mimicking cell membrane compositions, have been used. These mixtures usually contain a lipid species with high T_m, one with low T_m, and cholesterol, thus giving rise to L_o/L_d phase coexistence. Ipsen et al. were the first to describe the formation of a L_o phase using cholesterol and saturated phospholipids (35). In the context of simple model membranes, it was easy to characterize this novel lipid phase which was described as follows: "the dynamics of a lipid molecule within the L_o phase are similar to that in a fluid membrane, while the cis/trans configuration of the lipid chains is more similar to that in a gel state" (36). The formation of this peculiar phase was attributed to the specific properties of cholesterol (37), but it was eventually shown that many sterols can form a L_o phase (38). The interaction of cholesterol with the other lipids in the L_o phase depends on the nature of their hydrocarbon chains and, partially, on their headgroups. More specifically, the interaction preference decreases from SM to PS, PC and PE and with increasing unsaturation of the acyl chains (39). For these reason, a "typical" L_o phase can be pictured as constituted of SM and cholesterol. The first visualization of L_o/L_d phase coexistence was finally achieved by Dietrich et al. (40). Eventually, mixtures of SM, PC and cholesterol were studied at 37 °C, demonstrating liquid-liquid phase separation for a wide range of lipid compositions mimicking the outer leaflet of cell membranes (41). On the contrary, no phase separation was observed for model membranes mimicking the composition of the inner leaflet of the plasma membrane (42). It is worth noting that the domains observed in model membranes at the equilibrium are rather large (several micrometers) while domains in cells are expected to be small, possibly because cell membranes are not at equilibrium and/or because the cytoskeleton can hinder domain growth (43).

Finally, only few experiments have been performed to study the partition of membrane proteins in the different lipid phases, mostly because of experimental difficulties. The study of some membrane associated proteins or peptides (44,45) have shown that inclusion in the L_o phase might depend on the specific bilayer thickness. Another factor determining protein partition in a lipid phase could be the orientation of its dipole moment (46) as the membrane dipole moment is stronger and more uniformly oriented in the ordered phase. Nevertheless, the knowledge about lipid-protein interaction is still scarce and this area of research is challenging. In the next chapters, we will present technical advances that proved to be useful for lipid domain visualization and characterization, also in the presence of membrane proteins.

3.3 References

(1) Gennis R. B., 1989, Biomembranes: molecular structure and function, Springer.
(2) Voet D., and Voet J. G., 1995, Biochemistry, J. Wiley & Sons.
(3) Bacia K., 2006, Dynamic Processes in Membranes Studied by Fluorescence Correlation Spectroscopy, PhD Thesis, TU Dresden.
(4) Yeagle P. L., 1991, The structure of biological membranes, CRC Press
(5) Lipowsky R., and Sackmann E., 1995, Handbook of biological physics, Elsevier.
(6) Stryer L., Tymoczko J. L., and Berg J., 2002, Biochemistry, Freeman
(7) Alberts B., Johnson A., Lewis J., Raff M., Keith R., Walter P., 2002, Molecular biology of the cell, Garland
(8) Singer, S. J., and G. L. Nicolson. 1972. Fluid mosaic model of structure of cell-membranes. Science. 175:720-731.
(9) Allan D., 1996, Mol. Membr. Biol., 13:81-84.
(10) Tran D., 1987, Proc. Natl. Acad. Sci USA, 84:7957-7961.
(11) Spiegel S., 1984, J. Cell. Biol., 99:1575-1581.
(12) Harder T., 1998, J. Cell. Biol., 141:929-942.
(13) Brown D. A., and London E., 1998, Annu. Rev. Cell, Dev. Biol., 14:111-136.
(14) Simons K., and Ikonen E., 1997, Nature, 387:569-572.
(15) Lichtenberg D. M., Goni F. M., and Heerklotz H., 2005, Trends Biochem. Sci., 30:430-436.
(16) Munro S., 2003, Cell, 115:377-388.
(17) Gidwani A., Holowka D., and Baird B., 2001, Biochemistry, 40:12422-12429
(18) Gaus K., 2003, Proc. Natl. Sci. USA, 100:15554-15559.
(19) Pralle A., 2000, J. Cell. Biol., 148:997-1008.
(20) Prior I. A., 2003, J. Cell. Biol., 160:165-170.
(21) Sharma P., 2004, Cell, 116:577-589.
(22) Kusumi A., Koyama-Honda and Suzuki K., 2004, Traffic, 5:213-230.
(23) Fujiwara T., 2002, J. Cell. Biol., 157:1071-1081.
(24) Lafont F., 1998, J. Cell. Biol., 142:1413-1427.
(25) Meyer H. W., Semmler K., and Quinn P. J., 1997, Mol. Membr. Biol., 14:187-193.
(26) Vist M. R., and Davis J. H., 1990, Biochemistry, 29:451-464.
(27) Walde P., Ichikawa S., 2001, Biomol. Eng., 18:143-147.
(28) Sackmann E., 1996, Science, 271:43-48.
(29) Lipp M. M., Lee K. Y. C., Zasadzinsky J. A., and Waring A. J., 1996, Science, 273:1196-1199
(30) Müller P., Rudin D. O., Tien H. T., and Wescott W. C., 1996, Nature, 194:979-981
(31) Xu X., and London E., 2000, Biochemistry, 39:843-849.
(32) McElhaney R. N., 1982, Chem. Phys. Lipids, 30:229-259.
(33) Van Duyl B. Y., Ganchev D., Chupin V., de Kruijff B., Killian J. A., 2003, FEBS Lett., 547:101-106.
(34) Burgos P., Yuan C., Viriot M. L., and Johnston L. J., 2003, Langmuir, 19:8002-8009.
(35) Ipsen J. H., 1987, Biochim. Biophys. Acta, 905:162-172.
(36) Ipsen J. H., Mouritsen O. G., and Zuckermann M. J., 1989, Biophys. J., 56:661-667.
(37) Miao L., 2002, Biophys. J., 82:1429-1444.
(38) Xu X., and London E., 2001, J. Biol. Chem., 276:33540-33546.
(39) Leventis R., and Silvius J. R., 2001, Biophys. J., 81-2257-2267.
(40) Dietrich C., 2001, Biophys. J., 80:14-17-1428.
(41) De Almeisa R. F., Fedorov A., and Prieto M., 2003, Biophys. J., 85:2406-2416.
(42) Wang T. Y., and Silvius J. R., 2001, Biophys. J., 81:2762-2773.
(43) Yethiraj A., and Weisshaar J. C., 2007, Biophys. J., 93: 3113-3119

(44) Dietrich C., 2001, Proc. Natl. Acad. Sci. USA, 98:10642-10647.
(45) McIntosh T. J., Vidal A., and Simon S. A., 2003, Biophys. J., 85:1656-1666.
(46) Estronca L. M., 2002, Biochem. Biophys. Res. Commun. 296:596-603.

Chapter 4 – Combination of AFM and FCS on supported membranes

The experiments described in this chapter have been performed in collaboration with Jonas Ries, Ana García-Sáez and Lars Renner.

4.1 Introduction

As already mentioned in the previous chapters, increasing evidence about the role of lateral organization in biological membranes has been presented in the last years (see for example Simons et al.(1)). In particular, great interest has arisen in specific microdomains, enriched in sphingolipids and sterols, commonly termed as membrane rafts(2-9). Although a full characterization and even the existence of raft domains *in vivo* is still under debate (10), studies on model membranes composed of sphingolipids, cholesterol and glycerophospholipids have contributed in shedding light on the physical principles behind the L_o-L_d phase separation (4). Both structural and dynamical properties of such "artificial rafts" have been investigated with many different techniques, including single particle tracking,(11) fluorescence recovery after photobleaching (FRAP)(12), x-ray diffraction (13), nuclear magnetic resonance (NMR)(14), confocal fluorescence imaging, also combined with atomic force microscopy (AFM)(15), or fluorescence correlation spectroscopy (FCS) (16). AFM has been used successfully to study the structure of lipid domains based on the height differences between the L_d and L_o phases with nanometric spatial resolution (17,18,19,20,21). As the conformational order of the lipid chains increases going from the L_d to the L_o phase (see paragraph 3.2), the thickness of the membrane increases accordingly. Furthermore, force measurements have been performed on single-phase model membranes to probe the mechanical response and even the line tension associated to the creation of holes by means of the AFM tip (see paragraph 1.4 and Ref.22,23,24). FCS has been performed on raft-exhibiting free standing membranes to monitor the partition and diffusion of several fluorescent probes and, hence, the lipid microenvironment in the different domains (25).

As commonly accepted, proteins are most likely involved in determining both raft structure and dynamics *in vivo*. For this reason, a more accurate physical model should incorporate proteins, both raft- and non raft-associated, in order to investigate their partitioning behavior, dynamics and, in general, their effects on the lateral organization of the membrane (26). With regard to this, interesting results were obtained studying the behavior of the GPI-anchored, raft associated, protein human placental alkaline phosphatase (PLAP) in DOPC/SM/cholesterol bilayers using FCS(27) or AFM (20,28). The latter studies showed that PLAP partitions strongly into L_o domains, in contrast with FCS measurements that showed only a modest, though significant, partition in such domains. The discrepancy has been ascribed to the presence of the solid membrane support and, in general, to the different experimental conditions but its origin is still not fully understood.

Both AFM and FCS are powerful techniques for the study of the lateral organization of biological membranes from multiple points of view. While AFM can provide structural information down to nanometric resolution, it remains a slow technique. A few minutes are usually required to produce a topographic image of the bilayer. On the other hand, fluorescence imaging gives information about the lateral distribution of up to three different fluorescent molecules in the bilayer in just a few seconds. Nevertheless, no topographical information is provided and the lateral resolution is 100-fold lower if compared to AFM. Finally, both imaging techniques lack dynamic information about the in-plane diffusion or interactions between the membrane components which might be provided, on the other hand,

by FCS. For these reasons, it is easy to imagine that a combined approach of all these techniques can offer a deeper insight into the physical properties of the sample.

In this chapter, we present a combination of AFM imaging, force measurements, fluorescence imaging and 2-focus scanning fluorescence correlation spectroscopy (2-focus SFCS) on a raft-exhibiting DOPC/SM/cholesterol model membrane, also in the presence of membrane proteins. The use of these complementary techniques on a single sample clarifies the discrepancies and solve the technical problems mentioned above, thus providing further insight into this biologically relevant model system. AFM height imaging provides high-resolution information about the structural organization of proteins and lipids in the membrane, force measurements allow the determination of the line tension and stability of the lipid bilayer (30) and AFM phase contrast imaging conveys information about surface charge, stiffness or viscoelasticity (31) of the sample. Fluorescence imaging and FCS can provide information about the dynamics involved in lipid-lipid and lipid-protein interactions. In particular, we show that 2-focus SFCS is able to give reliable partition and absolute (i.e. calibration free) diffusion coefficients for several fluorescent proteins and lipids, at the same time in different parts of the sample (32). We directly compare dynamical properties in the L_o and L_d phases obtained with FCS with the mechanical properties probed by AFM force measurements. Finally we show how the combination of such different approaches is effective in reducing artifacts deriving from the use of a single technique.

4.2 Materials and Methods

4.2.1 Chemicals

1,2-dioleoyl-*sn*-glycero-3-phosphocholine (dioleoylphosphatidylcholine; DOPC), N-stearoyl-D-erythrosphingosylphosphorylcholine (stearoyl sphingomyelin; SM) and cholesterol were purchased from Avanti Polar Lipids (Alabaster, AL) and used without further purification. 1,1'-Dioctadecyl-3,3,3',3'-tetramethylindodicarbocyanine perchlorate (DiD-C_{18}, DiD), 3,3'-dioctadecyloxacarbocyanine perchlorate (DiO-C_{18}, DiO), BODIPY® FL C_5-ganglioside G_{M1} (BodGM$_1$), Alexa Fluor 488 cholera toxin subunit B (Alexa488CholTox), cholesteryl 4,4-difluoro-5,7-dimethyl-4-bora-3a,4a-diaza-*s*-indacene-3-dodecanoate (cholesteryl BODIPY® FL C_{12},, BODIPY-CholE), Lissamine rhodamine B 1,2-dihexadecanoyl-*sn*-glycero-3-phosphoethanolamine triethylammonium salt (rhodamine DHPE, RhoPE), N-4,4-difluoro-5,7-dimethil-4-bora-3a,4a-diaza-s-indacene-3-propionyl-1,2-dihexadecanoyl-*sn*-glycero-3-phosphoethanolamine triethylammonium salt (Bodipy FL DHPE, BodDHPE), N-4,4-difluoro-5,7-dimethil-4-bora-3a,4a-diaza-s-indacene-3-pentanoyl-sphingosine (Bodipy FL C_5-ceramide, BodCer), were purchased from Molecular Probes (Eugene, OR). The detergent 3-((3-cholamidopropyl)dimethylammonio)-1-propanesulfonic acid (CHAPS) and alkaline phosphatase from human placental tissue (PLAP) was purchased from Sigma. Before use, PLAP was purified and labeled with NHS-rhodamine (Pierce, Rockford, IL) as previously described 27,32b).Optical Adhesive 71, used to glue the mica on coverslips, was purchased from Norland Products Inc. (Cranbury, NJ). Three different buffers were used for sample preparation and imaging: 3 mM KCl, 1.5 mM KH_2PO_4, 8 mM Na_2HPO_4, 150 mM NaCl, pH 7.2 (buffer A); 3 mM $CaCl_2$, 150 mM NaCl, 10 mM Hepes, 3 mM NaN_3, pH 7.4 (buffer B); 150 mM NaCl, 10 mM Hepes, 3 mM NaN_3, pH 7.4 (buffer C). All buffers were filtered through a 200 nm filter (Nalgene, Rochester, NY) prior to use.

4.2.2 Supported lipid bilayers

Planar bilayers were preparated as already described by Chiantia et al. (19) Briefly, DOPC, cholesterol, SM and several fluorescent probes were dissolved in organic solutions with 1:0.7:1:(1-6·10^{-4}) molar proportion . The solvent was evaporated under nitrogen flux and then under vacuum for 30 minutes. The lipids were rehydrated with buffer A and resuspended by vigorous vortexing. After sonicating the suspension at 60° C, a small aliquot was diluted in buffer B and deposited on a ~10 μm thick piece of freshly cleaved mica that had been glued to a glass coverslip. The coverslip was sealed in the temperature-controlled Biocell stage (JPK Instruments, Berlin, Germany), transferred to the microscope and incubated at 55° C for 3 minutes. After that, the sample was rinsed at least 10 times with buffer C and then allowed to cool down to 25° C. Supported bilayers produced this way are stable for several hours. Samples prepared without heating and cooling cycles resulted in irreproducible results.

In the case of membranes containing RhoPLAP, the liposomes were used to produce proteoliposomes before deposition on mica using a simplified version of the procedure described by Kahya et al. (27). In particular, the protein and the liposomes were mixed in buffer A with final concentrations 2.5 mg/ml and 60 μg/ml respectively, in presence of 2% CHAPS. The expected protein/lipid ratio is then ~1:5000. After 24h dialysis against buffer A, a small aliquot was diluted 10 times in buffer B and deposited on mica as it was described above for the normal, protein-free, liposomes. In the case of staining with Alexa488CholTox, the supported bilayers contained 0.01% mol unlabeled GM_1; the toxin (10 μg/ml) was added and washed away after 2 minutes incubation.

4.2.3 Optical setup

Confocal imaging and scanning FCS measurements were performed on a LSM Meta 510 system (Carl Zeiss, Jena, Germany) using a 40× NA 1.2 UV-VIS-IR C-Apochromat water immersion objective and a home-built detection unit at the fiber output channel. An appropriate bandpass filter was used behind a collimating achromat to reject the residual laser and background light. Another achromat (LINOS Photonics, Goettingen, Germany) with a shorter focal length was used to image the internal pinhole onto the aperture of the fiber connected to the avalanche photo diode (APD, PerkinElmer, Boston, MA). The photon arrival times were recorded in the photon mode of the hardware correlator Flex 02- 01D (Correlator.com, Bridgewater, NJ). All filters and dichroic mirrors were purchased from AHF Analyse Technik, Tuebingen, Germany. The movement of the detection volume was controlled directly with the Zeiss LSM operation software.

4.2.4 2-focus SFCS data acquisition and analysis

Here we employ 2-focus SFCS for accurate measurements of diffusion constants as described by Ries et al. (32). In short, two parallel lines separated by a distance *d* are scanned alternately within the membrane, as depicted in figure 4.1b, using the imaging frame mode with 32x2 pixels. The use of the multiple track mode improved the parallelism but still the distance *d* varied by approx. 10% along the scan. The distance *d(x)* was well reproducible and it was determined with an accuracy of 3% by repeatedly scanning over a film of dried fluorophores and measuring the distance between the bleached traces in a high resolution

LSM image. Depending on the position x of the scanned line portion used to construct the correlation curves, the corresponding distance $d(x)$ was used for the fit.

The molecule detection function is given by the convolution of the Gaussian detection area with a step function of length s describing the scanning in x-direction. The resulting cross correlation curve $G(\tau)$ at lag times τ used to fit the data is (32):

$$G^{x}(\tau) = \frac{1}{c\pi s^{2}} \exp\left(-\frac{d^{2}}{w_0^{2}+4D\tau}\right)\left[\frac{\sqrt{\pi}s}{\sqrt{w_0^{2}+4D\tau}}\operatorname{erf}\left(\frac{s}{\sqrt{w_0^{2}+4D\tau}}\right)+\exp\left(-\frac{s^{2}}{w_0^{2}+4D\tau}\right)-1\right] \quad (4.1)$$

where c denotes the concentration, w_0 the $1/e^2$ radius of the detection area and D the diffusion coefficient. The auto correlation curve follows from Equation1 for $d = 0$. Because of the alternating data collection in the two foci, the resulting cross-correlation curve is shifted by the delay time t_d (32). If t_d is not much smaller than the diffusion time $\tau_D = w_0^2 / 4D$, this shift needs to be taken into consideration in performing the fit.

Data analysis was performed with software written in MATLAB (Math-Works, Natick, MA). The photons from corresponding parts of the sample (denoted by a box) of length s belonging to an equivalent time window were binned in bins of 2 µs, arranged as a matrix such that every row corresponds to one line scan and summed for each scan. These intensity values form the discrete time traces F_i and H_i which are used to calculate the auto and cross correlation curves $G(\tau_i)$ using a multiple τ correlation algorithm(32c). τ_i are integer multiples of the scanning period T. The correlation curves were fitted globally with a nonlinear least squares fitting algorithm to Equation1 to obtain one set of fit parameters. Errors given in the figures are the 95% confidence intervals on the nonlinear least squares parameter estimates.

4.2.5 AFM imaging and force measurements

AFM measurements were performed using a NanoWizard system (JPK Instruments, Berlin, Germany) mounted on the LSM Meta 510 system which is described in the Optical setup paragraph. Contact mode topographic images were taken in the constant-deflection mode, using uncoated silicon cantilevers (MikroMasch, Spain) with a typical spring constant of 0.03 N m^{-1}. For intermittent contact imaging, analogous cantilevers with a typical spring constant of 0.08 N m^{-1} were used. The force applied on the sample was maintained at the lowest possible value by continuously adjusting the setpoint during imaging. For non-contact imaging, the cantilever oscillation was tuned to a frequency between 5 and 10 KHz, and the maximum amplitude was set between 0.1 and 0.15 V (5-7.5 nm). The scan rate was set between 1 and 2 Hz for contact mode and between 0.7 and 1 Hz for intermittent contact mode. Height, deflection and phase shift signal were collected, simultaneously, in both trace and retrace directions. Images were line-fitted as required. Occasionally, isolated scan lines were removed.

Force measurements were performed using V-shaped silicon nitride cantilevers (Veeco,Santa Barbara, CA) with a nominal spring constant of 0.12 N/ m^{-1}. Calibration of both sensitivity, resonance frequency and effective spring constant (via thermal noise method)(32d) were performed before and after each experiment. The total z-piezo displacement was always 300 nm and the indenting speed was set to 800 nm/sec for all the experiments, so that the effect of speed on the breakthrough force could be neglected. The approach curves were analyzed using the free software Punias (P. Carl and P. Dalhaimer, ® 2004) and the threshold yield was measured for 200-400 different curves in each sample and plotted in histograms (22). The histograms were then fitted as described in section 1.4 of this thesis.

4.3 Results and Discussion

4.3.1 Structure and dynamics on raft-exhibiting supported bilayers

Mica-supported bilayers were prepared using DOPC, SM and cholesterol in 1:1:0.7 proportions. Figure 4.1a shows the typical topographical features of such a sample, observed using contact-mode AFM imaging. In line with previous results (21,19,33), two different phases can be observed: the lower, DOPC-rich, L_d phase and the higher, SM- and cholesterol-rich, L_o phase. The latter is organized in microscopic round L_o domains, ~0.8 nm higher than the surrounding phase.

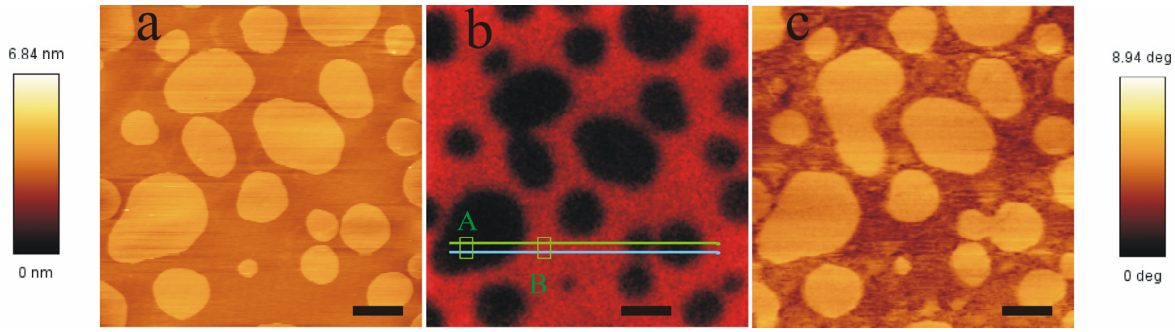

Figure 4.1 *Supported lipid bilayer composed of SM/DOPC/cholesterol 1:1:0.7 imaged at 25°C using different techniques in parallel. Panel a) shows the AFM topographical image of the supported membrane, obtained in contact mode. The light-coloured domains are ~0.8 nm higher than the rest of the membrane. Panel b) shows the confocal fluorescence image of the same part of the sample. The fluorescent probe was DiD, used at 0.1% molar concentration. The dark patches in the membrane consist of lipids in L_o phase, which tend to exclude bulky fluorophores. Such ordered domains are coincident with the higher domains shown in panel a). The two horizontal lines represent a typical scanning path used for the laser in the 2-focus SFCS measurements. The boxes A and B represent portions of the above mentioned lines used to calculate auto- and cross-correlation curves in different lipid domains. Panel c) shows the AFM phase-contrast image of the same part of the sample, obtained in intermittent-contact mode, few minutes after collecting the images in panels a) and b). The light coloured zones indicate parts of the samples for which a significant phase shift in the cantilever oscillation is measured, compared to the rest of the sample. The differently coloured regions in the phase image indicate parts of the samples with different phase shifts in the cantilever oscillation. This contrast is related to the mechanical response of the membrane. Scale bar = 2 μm.*

The phase assignment is also confirmed by the partition of 1,1'-Dioctadecyl-3,3,3',3'-tetramethylindodicarbocyanine perchlorate (DiD), as shown in figure 4.1b. The fluorescent dye is excluded from the more ordered raft-like domains. Figure 4.1c shows the intermittent-contact mode AFM phase imaging on the same part of the sample. Briefly, in contact mode imaging the AFM tip is scanned over the surface with a constant force, measured by the deflection of the cantilever. In intermittent contact mode, the cantilever is oscillated and the scanning is controlled using the oscillation amplitude. The phase difference between the cantilever response and the driving oscillation can also be measured, and the changes over

different parts of the sample show contrast from sample properties such as adhesion and viscoelasticity (31,34). The data shown in this panel indicate, in a qualitative way, that the two lipid phases are not only characterized by a different height but, as can be expected, also by a different stiffness. They were collected few minutes after those presented in figure 4.1a and b. The changes in the shape of the domains between the three different panels illustrate the dynamic nature of the L_o domains, as a consequence of their low degree of translational order compared to lipids in the gel state (1). Such changes are also observable using confocal fluorescence microscopy alone, and this excludes the possibility of tip-induced artifacts (data not shown).

In order to obtain quantitative information about the microviscosity in both L_d and L_o phases in supported bilayers, we performed 2-focus SFCS measurements using different fluorescent probes (see experimental section). The laser was focused by the objective on the plane of the membrane and the detection volume was scanned through the sample in two parallel lines, as depicted in figure 1b for the bilayer containing DiD. Fluorescence intensity was collected from equivalent time windows from corresponding parts of the sample (e.g. boxes A or B in figure 4.1b), summed up, and finally auto- and cross correlation curves were calculated. Global fitting of these three curves provides the concentration of the diffusing molecules c, the focus waist w_0 and the diffusion coefficient D. During the measurement time of 5-20 min, the sample was relatively stable, thus allowing acquisition of high signal-to-noise ratio correlation curves with low average laser power. In this regard, we observed that the thickness of the mica support and of the glue (see Materials and Methods section) is critical for the optimization of the fluorescence signal detection. Poor results were obtained if the total thickness of the glass coverslip, glue layer and mica was larger than 180-190 μm (data not shown). Thicker supports cause spherical aberrations which cannot be corrected by the adjustment collar of the objective. Depending on the parts chosen to calculate the correlation curves (see e.g. boxes A and B in figure 4.1b), we obtained values for diffusion coefficients and fluorophores concentrations in both the L_o and L_d phases within a single measurement. Figure 4.2 shows typical results obtained for a sample containing 0.004% cholesteryl-Bodipy FL (BODIPY-CholE).

The upper panel shows three different curves. The triangles and the diamonds are the two auto-correlation curves, each computed from a portion of one line scan located in a L_o domain (see e.g. box A in figure 1b for a DiD-containing sample). The third experimental curve (circles) is the cross correlation between the fluorescence signals coming from the above mentioned line portions. The second panel in figure 4.2 shows analogous data measured for a portion of the line scan which was positioned in L_d phase (see e.g. box B in figure 4.1b for a DiD-containing sample). The two lowest panels in figure 4.2 finally show histograms of all the measured diffusion coefficients we collected for this type of lipid mixture.

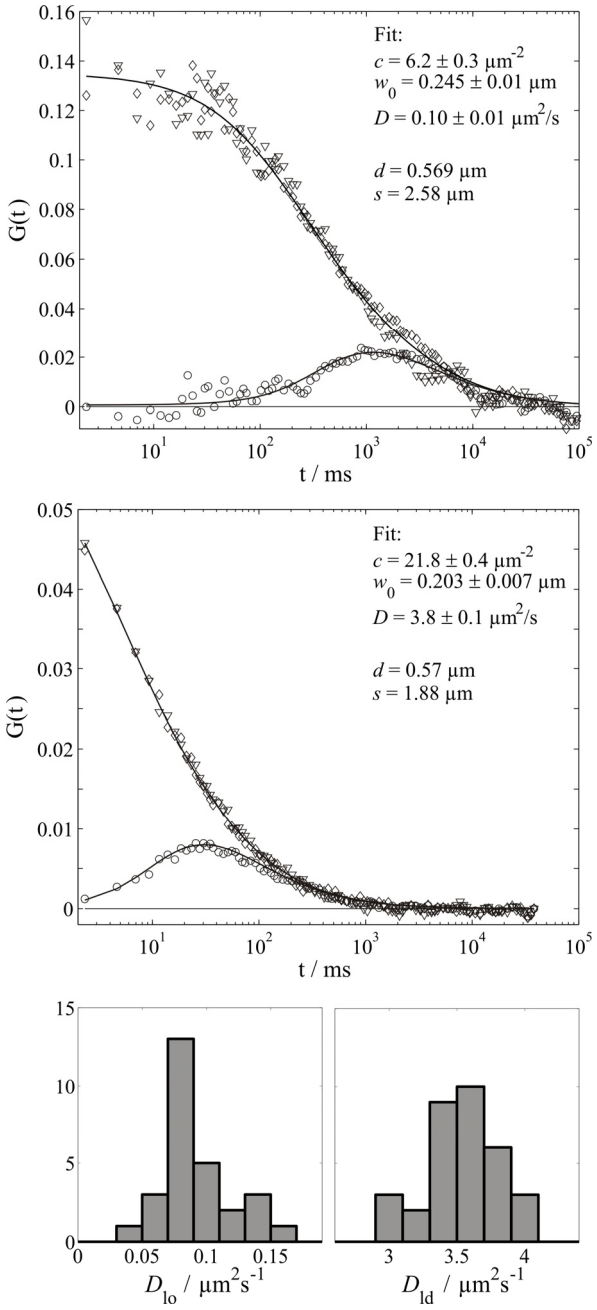

Figure 4.2 *Typical auto- and cross-correlation curves obtained with 2-focus SFCS in the L_o (upper panel) and L_d (middle panel) phase for the diffusion of BODIPY-CholE 0.004% mol in the membrane at 25°C. For each phase, the two auto-correlation curves (triangles and diamonds), the cross-correlation (circles) and the fitted curves (solid lines) are shown. The reported fit parameters indicate the concentration of fluorophores in the membrane, c, the laser spot radius, $w_{0,}$ the diffusion coefficient, D, the distance between the scanning lines, d, and the length of the line portions used to calculate the cross-correlation curves, s. The lower panels show the results obtained for all the examined samples containing 0.004% mol BODIPY-CholE for the L_o and L_d phases respectively.*

Table 1 shows the measured diffusion coefficients (D) and the ratio between the number of molecules in the L_o and L_d phase $K(L_o/L_d)$ for several fluorescent probes. It is evident that, especially for the L_d phase, the diffusion coefficients slightly depend on the structure of the different probes, although all are comparable to what has been measured for non-fluorescent lipids in similar model membranes (14,35).

Dye (molar concentration)	D_{Ld} ($\mu m^2/s$)	D_{Lo} ($\mu m^2/s$)	$K(L_o/L_d)$
BodCer (0.005%)	2.7±0.3	0.15±0.03	0.30±0.10
BODIPY-CholE (0.004%)	3.4±0.3	0.11±0.02	0.16±0.03
BODIPY-CholE (0.01%)	3.8±0.4	0.08±0.02	0.16±0.02
$BodGM_1$ (0.02%)	4.3±0.6	0.16±0.02	0.08±0.02
BodDHPE (0.005%)	2.9±0.6	0.12±0.03	0.075±0.005
DiO (0.005%)	1.73±0.12	0.090±0.014	0.020±0.002
DiD (0.01%)	1.5±0.1	0.16±0.04	0.004±0.002
RhoPE (0.005%)	2.4±0.8	-	<0.001
Alexa488CholTox [a]	1.1±0.4	0.040±0.008	11±5
RhoPLAP [b]	2.8±0.5	0.10±0.02	0.66±0.17

Table 1. *Diffusion coefficients in the different phases and partition coefficients for all the studied dyes. The table shows, for all the examined samples, the diffusion coefficient relative to the L_d phase and to the L_o phase. $K(L_o/L_d)$ represents the ratio of the fluorophore concentrations between the two phases. (a) This sample contained 0.01% mol ganglioside G_{M1}. (b) The initial protein molar concentration was ~0.02% mol.*

A dependence of the diffusion behavior on the used probe was also observed for free-standing membranes, and it is indeed reasonable to assume that small changes in structure might induce significant changes in intra- and intermolecular interactions among the membrane constituents (26). In line with previous observations (21,29), the diffusion coefficients we measured in the L_d phase of supported bilayers are generally small, if compared with other model systems. The diffusion of BODIPY-CholE, for example, is ~25% slower than what is measured in free-standing bilayers using classic FCS with a focal volume calibrated via diffusion of dye in water (Hartmann H., Bacia K. and P. Schwille, unpublished data). Possible reasons for these discrepancies could be ascribed back to 1- the different method used to calibrate the focal volume for FCS measurements, 2- the presence of 150 mM NaCl in the case of the supported membranes (36), or 3- the presence of the solid support. Regarding the last two possibilities, it is worth noting that we observed a correlation between the dynamics of different dyes and their charges. In particular, DiD and 3,3'-dioctadecyloxacarbocyanine perchlorate (DiO) are positively charged and, interestingly, exhibit the lowest D_{ld} among those we measured. The dyes with no charge -BODIPY-CholE, Bodipy FL C5 ganglioside G_{M1} ($BodGM_1$), and Bodipy FL C5 ceramide (BodCer)- are those that diffuse fastest. Such dependence of diffusion behavior on the charge of the fluorescent lipid analogue might origin either from electrostatic interaction with the negatively charged mica surface and/or from the presence of slower lipid clusters induced by the ions in the solution (36).

For the case of the L_o phase, a greater slowing effect (up to 75%) is observed in supported bilayers. In addition to the above mentioned reasons for the L_d phase, it is important to note that even small variations of the lipid mixture (e.g. cholesterol content) can dramatically change the diffusion coefficient in the L_o phase, leaving that of the Ld phase almost unaltered (25).

Finally, the partition behavior of the two last fluorescent probes shown in table 1 differs notably from the other lipophilic dyes. Both the fluorescent-labelled proteins PLAP and Alexa488-cholera toxin subunit B (Alexa488CholTox) show a higher affinity for the L_o phase than the fluorescent lipid analogues we examined in this work. While the high affinity of Alexa488CholTox for ordered domains and its dynamics in fluid bilayers are well characterized (16,37,29), the partitioning behaviour of the GPI-anchored protein PLAP is still controversial (38). Both the dynamics and the lateral organization on PLAP will be further analyzed in the following paragraphs.

The hindered dynamics that we reported here are a general demonstration of the strong interaction between the SLB and the solid support. The same non specific interactions could also cause problems regarding the mobility, integrity and function of trans-membrane proteins embedded in the bilayer (38b). As already mentioned in section 3.2 of this thesis, there have been a lot of efforts in developing alternative methods to create planar membranes with a spacer between the support and the bilayer (38c,38d). Renner et al. (38e) reported about a specific "cushioned" bilayer lipid membrane based on an anionic maleic acid copolymer substrate (38f) exhibiting a thickness of up to 60 nm in aqueous buffer solution (38e). Such system can be effectively characterized by the combined approach of AFM, LSM and FCS, as shown in Figure 4.3. Following the bilayer formation, it was possible to use the AFM to image and manipulate the lipid membrane on top of the polymer cushion. The lipid composition was a mixture of glycerophospholipids and cholesterol, including the fluorescent cholesterol analogue BODIPY-CholE. Figure 4.3a shows the topography of the sample, after a portion of the membrane was removed via controlled high-force scanning of the surface. This portion of the sample is represented in the height image by a dark square. Fig 4.3b shows the cross section indicated by the solid line in panel a. The average depth of the zone from where the sample was removed is around 8 nm, corresponding to the typical thickness of a lipid membrane, plus a ca. 2 nm thick water layer. As expected, no fluorescent signal was observed via LSM in the manipulated region (data not shown). Finally, figure 4.3c shows a FCS correlation curve obtained monitoring the diffusion of BODIPY-CholE. The diffusion coefficient of 2.5±0.2 $\mu m^2/s$ was similar to that measured for other membranes in the liquid phase (see e.g. Table 1). Thanks to the large distance between the bilayer and the solid support, this model membrane might be used for successful reconstitution of membrane proteins, also in the presence of large cytosolic domains which would normally interact with the support (38e).

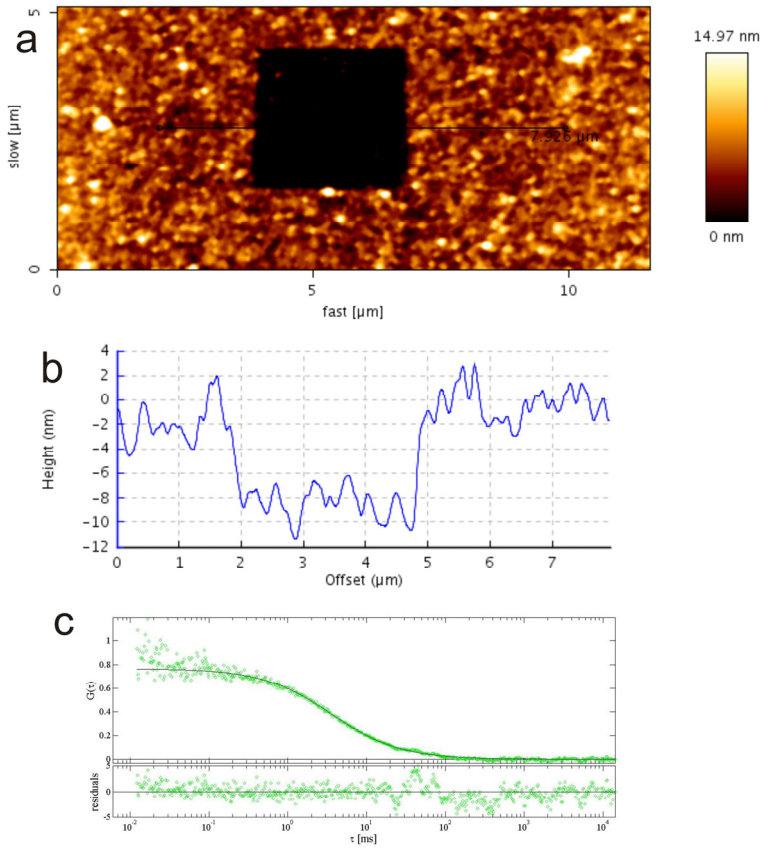

Figure 4.3 *Panel a) shows the AFM topography image of a lipid membrane supported on poly(ethylene-alt-maleic anhydride). The dark zone represents a portion of the sample in which the membrane was removed via controlled AFM micromanipulation. The solid line indicates a cross section which is displayed in panel b). Panel c) represents the FCS correlation curve obtained from the fluorescence signal of BODIPY-CholE diffusing in the membrane.*

4.3.2 Apparent two-component diffusion in supported bilayers

It was recently reported that small fluorescent aggregates or non-fused liposomes, moving slowly on the surface of the supported membrane, can severely distort the autocorrelation curve when performing FCS on dyes diffusing in the bilayer (21). The impurities, while resisting intensive rinsing, can be gently wiped away by the AFM tip, without damaging the sample. Figure 4.4 shows, on the left, a confocal fluorescence image for a SM/DOPC/cholesterol sample containing 0.01% mol BODIPY-CholE.

Due to the low degree of fluorescence labeling, small bright aggregates and vesicles are easily distinguished from the supported bilayer beneath them. The red square identifies a part of the membrane which was previously cleaned by AFM. Performing either standard FCS or 2-focus SFCS for the L_d phase (upper right panel) on a part of the membrane which contains such fluorescent impurities produced irregular results. In particular, a single-component 2-D diffusion model fitted the two auto-correlation curves (red and green) and the cross-correlation curve (blue) only poorly. The use a two-component 2-D diffusion model results in a dramatic improvement of the fit quality for the auto-correlation curves, suggesting the actual presence of much slower additional diffusion dynamics. Interestingly, no improvement of the fitting quality was observed for the cross-correlation curve (data not shown). FCS or 2-focus SFCS curves obtained on a "clean" part of the membrane, devoid of fluorescent impurities (lower right panel), could be successfully fitted with a one-component model. Similar distortions of the auto- and cross-correlation curves were observed occasionally when samples were not mechanically stable.

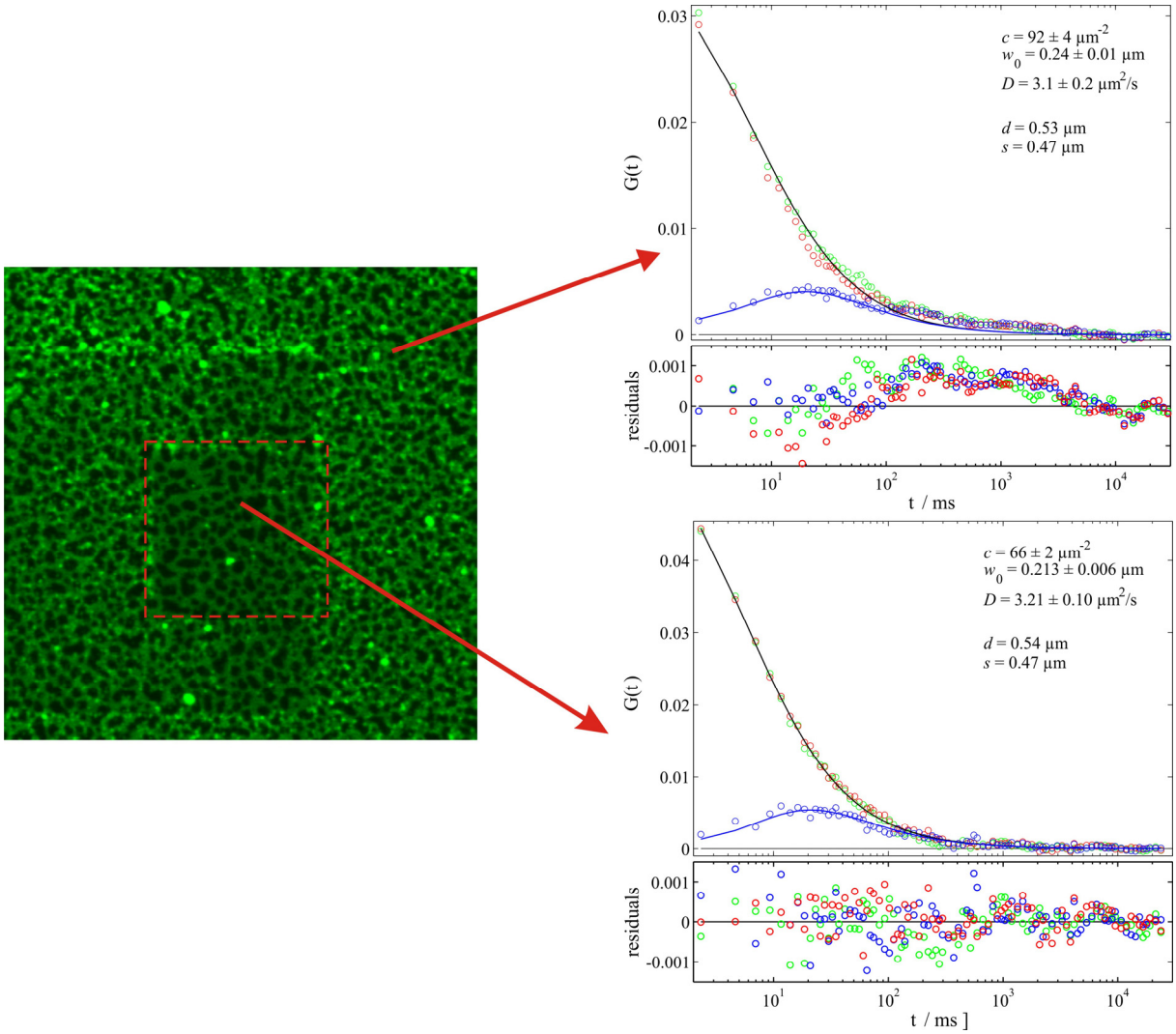

Figure 4.4 *Effect of fluorescent impurities on FCS data collection. On the left, a confocal image of a SM/DOPC/cholesterol 1:1:0.7 bilayer containing 0.01% BODIPY-CholE at 25°C. The dark parts in the membrane represent the L_o domains from which the BODIPY-CholE is excluded. Nonfused liposomes or fluorescent aggregates can be observed almost everywhere on the surface of the bilayer. The red square indicates a zone that was previously cleaned by scanning the AFM tip on the surface of the membrane. On the right side, the upper panel shows the 2-focus SFCS data collected for the L_d phase where the above mentioned fluorescent aggregates where still present. The two auto-correlation curves are shown in red and green and the cross-correlation is shown in blue. The solid lines represent the fit to a single component diffusion model. The residuals are shown with the same colours. Analogous experimental data, fit and residuals are shown in the lower right panel, for the L_d phase in the part of the bilayer that was cleaned by the AFM tip. The reported fit parameters are as for Figure 4.2.*

These results suggest that, if a single component diffusion model in supported membranes fails, simple experimental problems could be responsible: slow movements of the membrane in and out of the focal volume due to occasional mechanical instabilities of the system (e.g. objective, water, sample and sample holder), or the presence of slowly diffusing fluorescent particles should firstly be ruled out. More complex possibilities, like interactions with the support or local distortion and inhomogeneities of the membrane (39,29), can then be eventually considered.

4.3.3 Lateral organization and dynamics of PLAP in raft-exhibiting bilayers

Many different proteins are associated with cellular membranes via a C-terminal post-translational lipid modification, commonly known as glycosylphosphatidylinositol (GPI) anchor (40,41). The GPI moiety has been shown to be more than just a membrane anchor, being indeed fundamental for the function and regulation of certain membrane-associated proteins (42). Furthermore, several experimental evidences suggested that GPI-anchored proteins, like PLAP, perform their function by association with cholesterol- and sphingomyelin-enriched "raft" domains *in vivo* (43,44,45). In order to further address this question, it is important to study the lateral organization of GPI-anchored proteins in simple model membranes which exhibit liquid-liquid phase separation. As already mentioned, contrasting data about PLAP partitioning between L_o and L_d phase can be found in the literature (38). More specifically, two AFM studies (20,28) reported that PLAP partitions almost exclusively into raft-like L_o domains in SM/DOPC/cholesterol membranes, both if externally added or if already included in the liposomes before the formation of the supported bilayer. In sharp contrast, analogue FCS studies performed on free-standing giant unilamellar vesicles (GUVs) showed that PLAP partitions only modestly in L_o domains (27). Such behavior does not contradict the assignment of PLAP to the group of "raft-associated" proteins because its partition coefficient $K(L_o/L_d)$ of ~0.7 is still significantly higher than those of other "non raft-associated" proteins (27). The origin of the discrepancy was attributed mainly to the presence of the support needed for the AFM studies (27,38). In order to shed light on this apparent contradiction, we performed combined AFM, confocal fluorescence imaging and 2-focus SFCS on supported bilayers, with lipid/protein mixtures analogous to those used in the above mentioned studies.

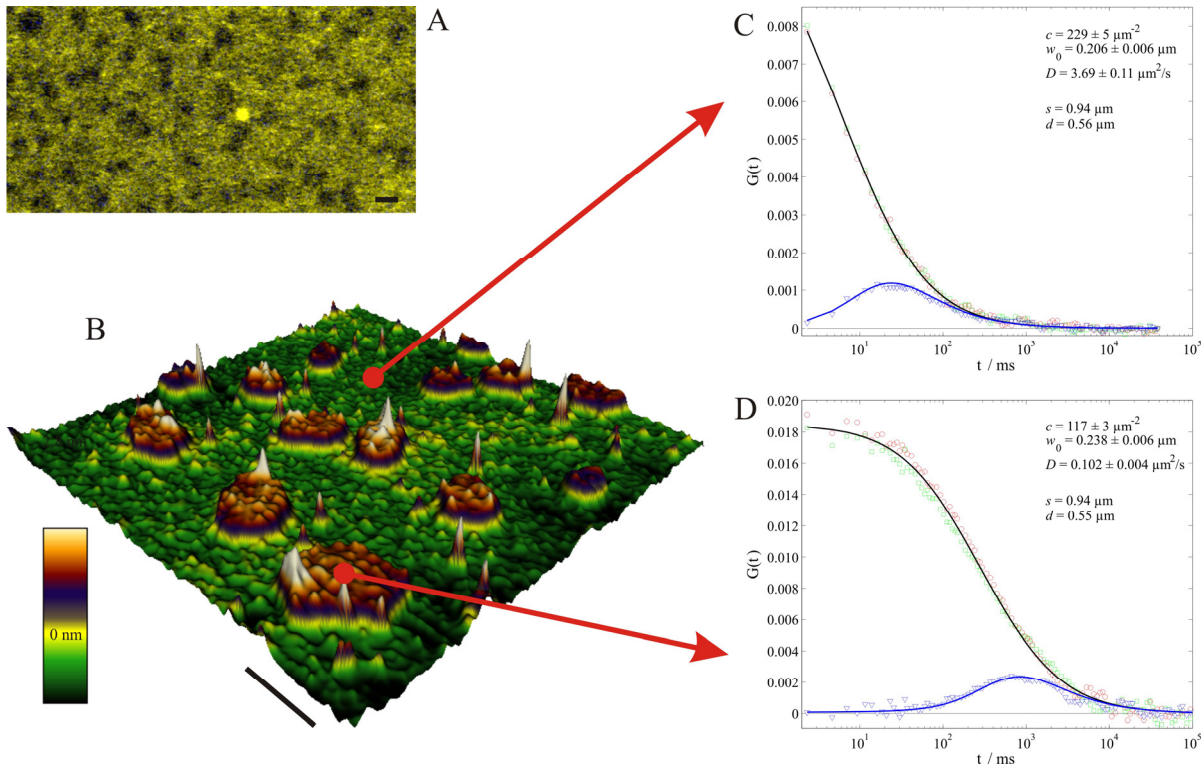

Figure 4.5 *Panel A) shows the confocal fluorescence image of a SM/DOPC/cholesterol supported bilayer containing the fluorescent protein RhoPLAP at 25°C. The darker patches can be identified as L_o domains which partially exclude the protein. The low contrast is due both to the low degree of labelling and to the significant affinity of the protein the L_o phase. Panel B) shows a 3-D topographical image of the same sample obtained by AFM. The protein*

can be visualized as white sharp spikes, a few nm higher than the lipid membrane. Panels C) and D) show 2-focus SFCS data for the diffusion of the PLAP in the plane of the membrane in both L_d and L_o phase respectively. For each panel, the two auto-correlation curves are shown in red and green and the cross-correlation is shown in blue. The solid lines represent the fit to a single component diffusion model. The reported fit parameters are as for Figure 4.2. Scale bar = 2 μm.

Panel b in figure 4.5 shows the AFM topographical image of a SM/DOPC/cholesterol bilayer, in the presence of ~0.02% mol NHS-rhodamine PLAP (RhoPLAP). Although a direct quantitative comparison is not possible because of small differences in sample composition and preparation procedures, our AFM results are in good agreement with those reported by Saslowsky et al. (20). The protein RhoPLAP, which can be visualized as 2-3 nm high spikes on the membrane topography, appears to partition preferably into L_o domains, with a partition coefficient $K(L_o/L_d)$ of ~3. It is important to point out that, in line with the abovementioned AFM study (20), the width of the spikes in figure 4.5b may indicate a degree of protein aggregation, especially in the L_o domains. Counting these larger spikes as single proteins, although leading to an underestimation of $K(L_o/L_d)$, does not affect the finding that AFM measurements indicate a fairly high affinity of RhoPLAP for L_o domains. Interestingly, this result is not confirmed by parallel confocal imaging of the protein distribution in the membrane. Figure 4.5a shows the signal coming from the fluorescent-labeled protein in a larger area of the sample. In spite of the low signal-to-noise ratio and the low contrast, small darker domains can be identified as L_o domains. It appears that the protein concentration in the surrounding L_d phase is higher than the concentration in the L_o phase. In order to confirm this result and to probe the dynamics of the protein in the membrane, we performed 2-focus SFCS on the same sample. Figures 4.5c and d show typical results obtained for PLAP diffusion in the bilayer, both in the L_d and in the L_o phases. A first remarkable result is that the concentration of the protein, either inside or outside the higher ordered domains, is $\sim 10^2$ higher than what is observed by AFM. Considering an occupied surface of roughly 0.5-1 nm^2/lipid, the effective protein:lipid ratio in our sample appears to be $\sim 1:10^6$ from AFM and $\sim 1:10^4$ from 2-focus SFCS, the latter being more comparable to the starting 1:5000 ratio used for preparing the sample (see Materials and Methods section). A second result is that PLAP seems to partition preferably in the L_d phase, with a partition coefficient $K(L_o/L_d)$ of ~0.7, more in agreement with the previous fluorescence-based measurements on GUVs (27). Finally, the protein diffuses in the membrane with diffusion coefficient D of 2.8 and 0.08 $\mu m^2/s$ in the L_d and L_o phases respectively. These values are comparable to those we measured for single fluorescent lipids in the membrane, in agreement with the Saffman-Delbrück theory according to which a monomeric GPI-anchored PLAP should diffuse in the membrane at approximately the speed of a lipid molecule (46). The correlation curves could be fitted with a single-component model, thus excluding a significant fraction of large slowly diffusing protein aggregates. The presence of smaller aggregates, however, cannot be ruled out since their diffusion coefficient would be reduced only slightly. Immobilized proteins would bleach quickly and would not contribute to the correlation curves.

We argue that the protein molecules visualized by AFM as immobile protuberances located preferably in the ordered domains, are only a small fraction (1-10%) of the total protein which is incorporated into the bilayer. This immobile fraction might originate, for example, from protein aggregation, unfolding and/or anomalous interactions with the mica support. The remaining fraction of PLAP, which is diffusing in the fluid membrane, might not be easily visualized by AFM, because of the relatively slow speed of the AFM tip scanning the surface of the membrane and, as a consequence, the long time needed for the imaging process. Even

in the case of a transient interaction of the tip with a fast moving particle on the membrane, the resulting signal could not be easily distinguished from noise. As a consequence, the apparent partition behavior could also be biased in some experiments, because the protein is more likely to be observed if it is not moving very fast, for example in more viscous domains or at the interface between different phases. In conclusion, we showed that AFM could be impaired in describing fast processes, like protein dynamics in fluid membranes. Coupling to a complementary technique, like FCS, can overcome this limitation allowing a more complete characterization of both nanoscopic structural organization and dynamics of the system of interest.

4.3.4 Force measurements, line tension and diffusion

Besides imaging, AFM can be applied to characterize the mechanical properties of supported membranes. The cantilever deflection is recorded as a function of the z-piezo displacement. This information is then transformed in a so-called force curve, which represents the force applied by the AFM tip on the sample versus the tip-sample distance. Measuring force curves on supported lipid bilayers, a discontinuity is often observed while the tip is compressing the sample. This discontinuity, or jump, is due to the rupture of the membrane, once a certain threshold force is reached (see Section 2.4 of this thesis and Ref. 24,47,48). The inset in Figure 4.6 shows two typical force curves measured in the two lipid phases of a SM/DOPC/cholesterol supported bilayer.

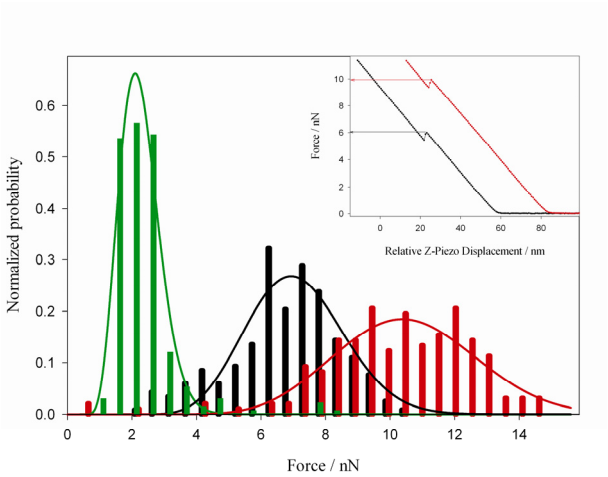

Figure 4.6 *Normalized histograms of the force needed to pierce the bilayer with the AFM tip (threshold yield), measured for different samples at 25°C. The green histogram bars refer to a piercing experiment performed on a DOPC supported bilayer. The red and the black histogram bars refer, respectively, to the L_o and L_d phase in a SM/DOPC/cholesterol bilayer. The number of measured points was between 200 and 400. The solid lines refer to the fit of the histograms to the model described by Butt et al. (24). Inset: typical force curves for L_o (red) and L_d (black) phase. The force applied by the cantilever is represented as a function of the z-piezo displacement. The horizontal lines indicate the jumps in the force curves (threshold yields) where the cantilever tip pierces the membrane.*

The threshold yields are represented in red and black for the L_o and L_d phases respectively, and they correspond to the maximum force the bilayer can withstand before being pierced through. For this reason, a quantitative analysis of the threshold yield distribution provides

information about membrane packing, stability, as well as inter-molecular interaction among lipid molecules (22).

Figure 4.6 shows, in the main panel, the histograms of the measured threshold yields for a raft-exhibiting supported bilayer, in the L_d (black) and in the L_o (red) phases. For comparison, the histogram from an analogous experiment is shown in green for a simple DOPC bilayer. The force needed to pierce the bilayer is significantly higher in the L_o, raft-like, phase suggesting a higher degree of conformational order, compared to the L_d phase or to the DOPC control sample. In order to derive microscopic parameters connected to the physical state of the membrane, we further analyzed these results using the model by Butt et al. based on the continuum nucleation theory (24). The distribution of forces needed to create a hole in the membrane is connected to the line tension Γ, which represents the free energy associated with the unsaturated bonds of the molecules at the periphery of the hole, and with the effective spreading pressure *S*, which is a parameter related to membrane adsorption to a solid surface. Fitting the histograms to this model (see Materials and Methods section) provided the quantitative results shown in table 2.

	D ($\mu m^2/s$)	$<F_t>$ (nN)	Γ (pN)	S (mN/m)
DOPC	5.8±0.4	1.7	3.9±0.3	1.0±0.6
Liquid-disordered	3.5±0.3	6.5	8.3±0.7	4±3
Liquid-ordered	0.1±0.02	10.2	11.2±1.0	4±4

Table 2. *Comparison between diffusion coefficients and fit parameters from force measurements. The table shows, for a pure DOPC sample and the two phases of a raft-exhibiting bilayer, the measured diffusion coefficient D, the average threshold yield $<F_t>$, the line tension Γ and the surface energy S.*

The estimated line tensions and spreading pressures are in the same range of those found in previous measurements (49,50,24). Furthermore, increasing line tensions are evidently related to decreasing diffusion coefficients, thus showing a clear connection between the inter-molecular forces detected by AFM and the microviscosity in the lipid environment, as detected by 2-focus SFCS. The same combined approach of AFM and fluorescence microscopy has been successfully applied by Garcia et al. (50b,50c) to study the line tension and the lateral membrane organization in similar lipid mixtures. More in detail, force measurements were used to investigate the effects of a pore-forming peptide on the line tension of the bilayer. Furthermore, the connection between line tension, phase separation and height mismatch of lipid components was thoroughly analyzed. In this case, the coupling between a fast technique like fluorescence imaging and a slower highly sensitive surface technique like AFM allowed the simultaneous study of domain formation kinetics and detailed spatial structure.

4.4 Conclusions

The structural, mechanical and dynamic properties of model membranes of biological relevance have been investigated. In particular, the liquid-ordered/liquid-disordered phase separation in DOPC/SM/cholesterol supported bilayers has been studied with a combined approach of AFM, confocal fluorescence imaging, force measurements and 2-focus SFCS, based on commercially available instruments. Precise diffusion coefficients for fluorescent lipids and two membrane proteins have been measured and shown to be comparable with

diffusion in free-standing membranes. Occasional distortion of auto-correlation curves, which might suggest the presence of different diffusing species, has been attributed to the presence of impurities on the membrane which can be effectively removed by the AFM tip. Furthermore, a clear relationship between the line tension in different lipid phases and their microviscosity, as probed by FCS, has been revealed. Finally, the combination of AFM and FCS on more complex model systems containing the GPI-anchored protein PLAP clarified the incongruences derived from separate fluorescence and AFM studies on similar systems.

In conclusion, the combination of AFM and single molecule fluorescence techniques in complex model membrane has been proved to be a promising approach to characterize the lipid-lipid and lipid-protein interactions driving the lateral organization of membrane components in living cells.

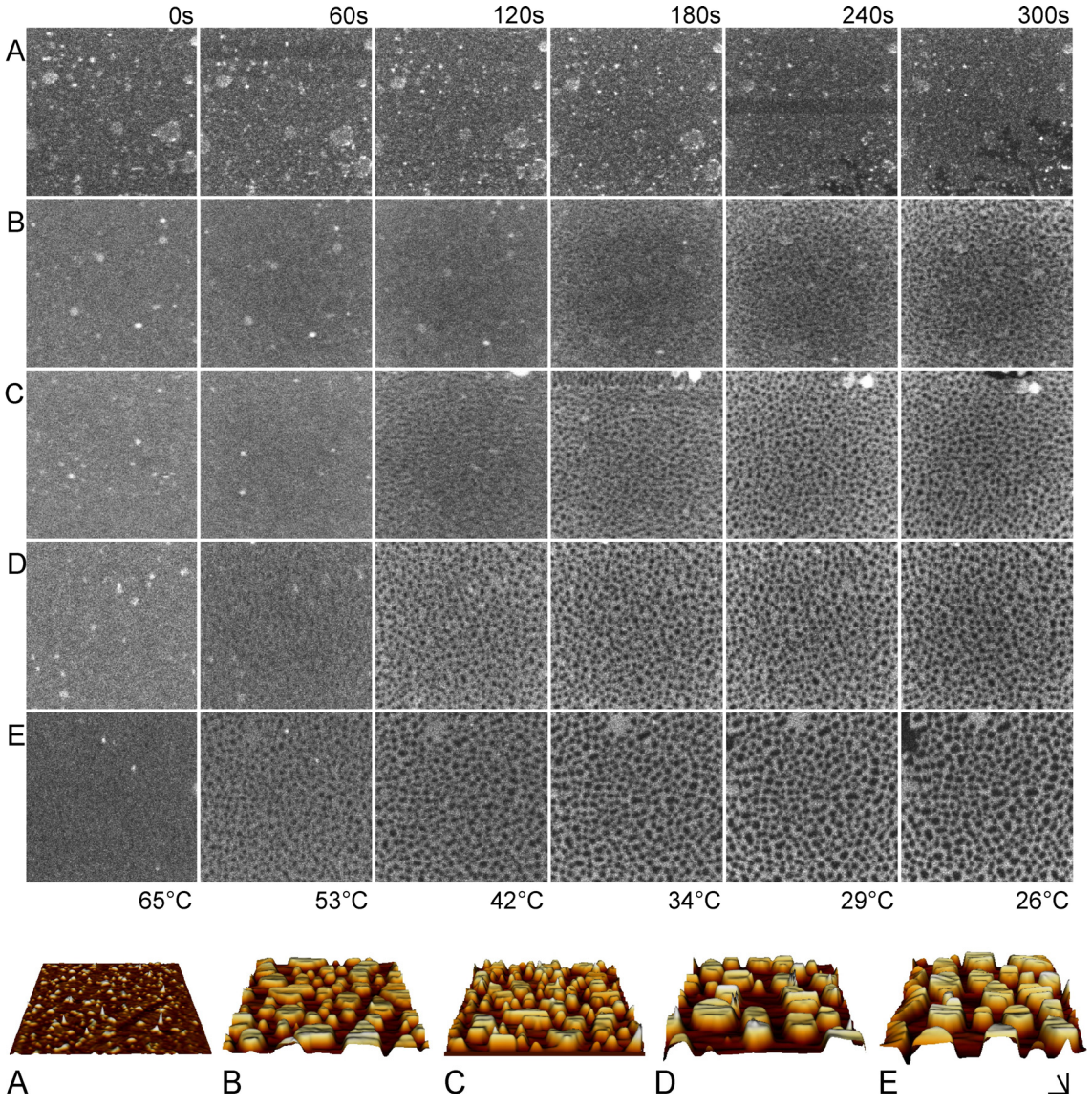

Figure 4.7 *Complementarity of AFM and fluorescence microscopy approaches. Supported membranes exhibiting L_o/L_d phase separation were prepared using PC with acyl chain length varying from 14 to 22 carbon atoms (samples A to E). Fluorescence LSM is used to monitor domain formation kinetics, in order to measure the demixing temperature of the lipid mixture. AFM can be then performed on the same samples to gain detailed topographical information and quantitative information about the height of lipid domains. Courtesy of Dr. Ana Garcia (50c).*

4.5 References

(1) K. Simons, W. L. C. Vaz, *Annu. Rev. Biophys. Biomol. Struct.* **2004**, *33*, 269-295.
(2) A. G. Lee, *Biochim. Biophys. Acta* **1977**, *472*, 285-344.
(3) K. Simons, E. Ikonen, *Nature* **1997**, *387*, 569-572.
(4) D. A. Brown, *Proc. Natl. Acad. Sci. U. S. A.* **2001**, *98*, 10517-10518.
(5) J. R. Silvius, *Biochim. Biophys. Acta, Biomembr.* **2003**, *1610*, 174-183.
(6) Y. Barenholz, T. E. Thompson, *Biochim. Biophys. Acta* **1980**, *604*, 129-158.
(7) R. G. W. Anderson, *Annu. Rev. Biochem.* **1998**, *67*, 199-225.
(8) S. Mayor, M. Rao, *Traffic* **2004**, *5*, 231-240.
(9) L. Rajendran, K. Simons, *J. Cell Sci.* **2005**, *118*, 1099-1102.
(10) M. Edidin, *Annu. Rev. Biophys. Biomol. Struct.* ***2003***, 32, 257-283.
(11) G. J. Schutz, H. Schindler, T. Schmidt, *Biophys. J.* ***1997***, 73, 1073-1080.
(12) E. Kalb, S. Frey, L. K. Tamm, *Biochim. Biophys. Acta* ***1992***, 1103, 307-316.
(13) M. Gandhavadi, D. Allende, A. Vidal, S. A. Simon, T. J. McIntosh, *Biophys. J.* ***2002***, 82, 1469-1482.
(14) A. Filippov, G. Oradd, G. Lindblom, *Biophys. J.* **2006**, *90*, 2086-2092.
(15) J. E. Shaw, R. F. Epand, R. M. Epand, Z. G. Li, R. Bittman, C. M. Yip, *Biophys. J.* **2006**, *90*, 2170-2178.
(16) K. Bacia, D. Scherfeld, N. Kahya, P. Schwille, *Biophys. J.* **2004**, *87*, 1034-1043.
(17) M. C. Giocondi, P. E. Milhiet, P. Dosset, C. Le Grimellec, *Biophys. J.* **2004**, *86*, 861-869.
(18) P. E. Milhiet, V. Vie, M. C. Giocondi, C. Le Grimellec, *Single Molecules* **2001**, *2*, 109-112.
(19) S. Chiantia, N. Kahya, P. Schwille, *Langmuir* **2005**, *21*, 6317-6323.
(20) D. E. Saslowsky, J. Lawrence, X. Y. Ren, D. A. Brown, R. M. Henderson, J. M. Edwardson, *J. Biol. Chem.* **2002**, *277*, 26966-26970.
(21) S. Chiantia, N. Kahya, J. Ries, P. Schwille, *Biophys. J.* **2006**, *90*, 4500-4508.
(22) S. Garcia-Manyes, G. Oncins, F. Sanz, *Biophys. J.* **2005**, *89*, 1812-1826.
(23) H. J. Butt, V. Franz, *Phys. Rev. E* **2002**, *66*.
(24) S. Loi, G. Sun, V. Franz, H. J. Butt, *Phys. Rev. E* **2002**, *66*.
(25) N. Kahya, D. Scherfeld, K. Bacia, B. Poolman, P. Schwille, *J. Biol. Chem.* **2003**, *278*, 28109-28115.
(26) N. Kahya, P. Schwille, *Mol. Membr. Biol.* **2006**, *23*, 29-39.
(27) N. Kahya, D. A. Brown, P. Schwille, *Biochemistry* **2005**, *44*, 7479-7489.
(28) P. E. Milhiet, M. C. Giocondi, F. Rouzon, B. Roux, C. Le Grimellec, *Mol. Biol. Cell* **2001**, *12*, 333A.
(29) A. R. Burns, D. J. Frankel, T. Buranda, *Biophys. J.* **2005**, *89*, 1081-1093.
(30) S. Garcia-Manyes, G. Oncins, F. Sanz, *Biophys. J.* **2005**, *89*, 4261-4274.
(31) M. Deleu, K. Nott, R. Brasseur, P. Jacques, P. Thonart, Y. F. Dufrene, *Biochim. Biophys. Acta, Biomembr.* **2001**, *1513*, 55-62.
(32) J. Ries, P. Schwille, *Biophys. J.* **2006**, *91*,1915-1924.
(2b) R. Schroeder, E. London, D. Brown, *Proc. Natl. Acad. Sci. U. S. A.* **1994**, *91*, 12130-12134.
(32c) D. Magatti, F. Ferri, *Applied Optics* **2001**, *40*, 4011-4021.
(32d) E. L. Florin, M. Rief, H. Lehmann, M. Ludwig, C. Dornmair, V. T. Moy, H. E. Gaub, *Biosens. Bioelectron.* **1995**, *10*, 895-901.
(33) P. E. Milhiet, V. Vie, M. C. Giocondi, C. Le Grimellec, *Single Molecules* **2001**, *2*, 109-112.

(34) C. Nicolini, J. Baranski, S. Schlummer, J. Palomo, M. Lumbierres-Burgues, M. Kahms, J. Kuhlmann, S. Sanchez, E. Gratton, H. Waldmann, R. Winter, *J. Am. Chem. Soc.* **2006**, *128*, 192-201.

(35) A. Filippov, G. Oradd, G. Lindblom, *Biophys. J.* **2004**, *86*, 891-896.

(36) R. A. Bockmann, A. Hac, T. Heimburg, H. Grubmuller, *Biophys. J.* **2003**, *85*, 1647-1655.

(37) K. Bacia, P. Schwille, T. Kurzchalia, *Proc. Natl. Acad. Sci. U. S. A.* a **2005**, *102*, 3272-3277.

(38) J. R. Silvius, *Biochim. Biophys. Acta, Mol. Cell Res.* **2005**, *1746*, 193-202.

(38b) E. Sackmann and M. Tanaka. *TIBTECH,* **2000***, 18*, 58.

(38c) M. K.Sharma and M. L. Gilchrist. *Langmuir,* **2007***, 23*, 7101.

(38d) S. Goennenwein, M. Tanaka, B. Hu, L. Moroder, and E. Sackmann. *Biophys. J.*, **2003,** *85*: 646.

(38e) L. Renner , T. Osaki, S. Chiantia , P. Schwille, T. Pompe, and Werner C., *Langmuir*, **2007**, submitted

(38f) T. Pompe, S. Zschoche, N. Herold, K. Salchert, M. F. Gouzy, C. Sperling, C. Werner, *Biomacromolecules* 2003, 4, 1072.

(39) A. Benda, M. Benes, V. Marecek, A. Lhotsky, W. T. Hermens, M. Hof, *Langmuir* **2003**, *19*, 4120-4126.

(40) S. Udenfriend, K. Kodukula, *Annu. Rev. Biochem.* **1995**, *64*, 563-591.

(41) S. Chatterjee, S. Mayor, *Cell Mol. Life Sci.* **2001**, *58*, 1969-1987.

(42) T. E. Ritter, O. Fajardo, H. Matsue, R. G. Anderson, S. W. Lacey, *Proc. Natl. Acad. Sci. U. S. A.* **1995**, *92*, 3824-3828.

(43) K. Simons, G. van Meer, *Biochemistry* **1988**, *27*, 6197-6202.

(44) T. Harder, P. Scheiffele, P. Verkade, K. Simons, *J. Cell Biol.* **1998**, *141*, 929-942.

(45) D. A. Brown, J. K. Rose, *Cell* 1992, *68*, 533-544.

(46) P. G. Saffman, M. Delbruck, *Proc. Natl. Acad. Sci. U. S. A.* **1975**, *72*, 3111-3113.

(47) V. Franz, S. Loi, H. Muller, E. Bamberg, H. H. Butt, Colloids and Surfaces B-Biointerfaces **2002**, *23*, 191-200.

(48) H. J. Butt, B. Cappella, M. Kappl, *Surf. Sci. Rep.* **2005**, *59*, 1-152.

(49) I. Genco, A. Gliozzi, A. Relini, M. Robello, E. Scalas, *Biochim. Biophys. Acta* **1993**, *1149*, 10-18.

(50) J. D. Moroz, P. Nelson, *Biophys. J.* **1997**, *72*, 2211-2216.

(50b) A. Garcia, S. Chiantia, J. Salgado, P. Schwille, *Biophys. J.,* **2007**, 93:103-112.

(50c) A. Garcia, S. Chiantia, P. Schwille, *J. Biol. Chem.,* **2007**, in press.

Chapter 5 – Dehydration stress on raft-exhibiting model membranes

5.1 Introduction

The structural integrity and function of biological membranes are strictly dependent on the presence of surrounding water molecules. For this reason, dehydration usually results in irreversible damage (1). Nevertheless, many organisms, from bacteria to fungi, plants, and animals show the ability to survive complete dehydration, in a suspended state called anhydrobiosis, which means "life without water". The majority of desiccation-tolerant organisms synthesize large amounts of disaccharides, such as sucrose or trehalose, during dehydration,(2-4) and the sugar production is thought to be a stress response essential to the survival of the organism.(5) This very same strategy has been applied to develop new technologies for long-storage and stabilization of mammalian cells-from red blood cells (6) to platelets (7) and stem cells, (8) which is the major goal in cryobiology. In vitro FTIR studies have shown that these carbohydrates preserve the structural and functional properties of both biological membranes and soluble proteins (9-10). In particular, dehydration of membranes in the absence of protective molecules has been shown to lead to massive and irreversible aggregation and/or separation of membrane components (11). Upon drying, proteins can aggregate, be excluded from the membrane, or be redistributed on both membrane sides while other components, such as non-bilayer lipids, form completely separate phases. The presence of disaccharides during dehydration has been demonstrated to be sufficient to prevent these fatal changes in the membrane structure (12). Several mechanisms have been proposed to explain the protective effect of sugars under conditions of complete dehydration. According to the water replacement hypothesis, upon dehydration, sugars can replace water molecules by interacting with the polar headgroups of the phospholipids, thus stabilizing their native structure (1,2,13). An alternative could be the water concentration hypothesis, which proposes that sugars concentrate the residual water close to the biostructures, thus maintaining their original structure and solvation properties (14,15). Other authors, instead, attribute the protection effect to a purely mechanical phenomenon (vitrification), which involves the formation of a glassy state as the main factor for the preservation of the membrane integrity (16,17). The three processes are most likely not mutually exclusive (18,19). Comparative studies on conservation of frozen or dried liposomes, by using several stabilizing compounds (e.g., disaccharides, dimethyl sulfoxide, dextran, and others), showed that the specificity for protection against dehydration is high. Only disaccharides, like trehalose, protect from membrane damage during desiccation, most likely by preventing both fusion and leakage events, which originate from lipid phase transitions during dehydration and/or after rehydration (20,21).

Given the highly heterogeneous composition of biological membranes, which could lead to formation of raft microdomains (22) it is of great interest to study the effects of lyoprotectants on domain-forming bilayers subjected to drying conditions. Lipids of specific chemistry, mainly sphingolipids and cholesterol, have been proposed to cluster, thereby forming specialized platforms, which are involved in several biological functions, including lipid trafficking, protein sorting, endo- and exocytosis and cell-cell signaling (22,23). The effects of dehydration on such domains are not fully understood yet. Nevertheless, it has been proposed that lipid phase transitions and lateral phase separation of blood platelet membrane components, both due to chilling or drying, could be responsible for driving the aggregation of ordered domains to form macroscopic domains, as evidenced by FTIR and fluorescence

spectroscopy (24). The aggregation leads to inappropriate signaling and thus to physiological activation, which makes the chilled or dried stored platelets clinically useless (24). Conversely, if platelets are freeze-dried in the presence of trehalose, the physiological damage is avoided (25). The effect of cryoprotectants on the lipid phase behavior of heterogeneous membranes has been recently addressed by analyzing the stability of liposomes composed of dilauroylphosphatidylcholine and distearoylphosphatidylcholine, upon dehydration, by FTIR spectroscopy (26). It was shown that trehalose maintains the phase separation for such lipid mixtures during drying, preserving the features observed in the hydrated state.

In this chapter, we apply atomic force microscopy (AFM) and fluorescence imaging to describe the effects of water removal, with and without lyoprotectants, on supported lipid bilayers (SLB) composed of sphingomyelin (SM), cholesterol, and dioleoylphosphatidylcholine (DOPC) in molar ratios that give rise to L_d/L_o phase coexistence. A striking difference was observed between the effect of disaccharides (trehalose, sucrose) and other glass-forming compounds upon membrane drying. Finally, we show that AFM provides a very useful tool to analyze the topological details of domain morphology and bilayer structure of complex planar bilayers after dehydration/rehydration treatment.

5.2 Experimental procedures

5.2.1 Chemicals

For a complete list of the chemical used for the experiments described in this chapter, see also section 4.2.1. Trehalose dihydrate from Calbiochem (Darmstadt, Germany) was used after recrystallization from water (27). Glucose and chloroform were from Fluka (Buchs, Switzerland), sucrose from Merck (Darmstadt, Germany), dimethyl sulfoxide (DMSO) from Aldrich (Seelze, Germany), Dextran T70 from Amersham Pharmacia Biotech (Piscataway, NJ). The hydrophobic ink for sample confinement during AFM measurements is of common use in immunostaining, cell culture, histology and microbiology preparations and was purchased from Kisker (Steinfurt, Germany).

5.2.2 Preparation of supported lipid bilayers (SLB), AFM imaging and Confocal Fluorescence Microscopy

See sections 4.2.2, 4.2.3 and 4.2.5 of this thesis.

5.2.3 Dehydration and rehydration

After the quality of a freshly prepared supported bilayer was checked by imaging at least a total of 7500 μm^2 from different areas, the sample was washed several times with water to remove buffer salts which, during the dehydration process, could have formed crystals, thereby leading to undesired effects on the membrane. According to our measurements (data not shown), the SLB was stable for several hours in buffer 3. After washing with water, the

sample was stable at least for 3-4 h. After addition of the glass-forming stabilizing compound (0.4 mg in 0.5 mL of water, to ensure a uniform coverage of the entire SLB), the sample was then dried for 1 h in a desiccator under a filtered nitrogen flux, thereby removing the bulk water and, eventually, for at least 12 h under vacuum. Before the measurements, the samples were rehydrated and washed with buffer 3.

5.3 Results

5.3.1 Domain-exhibiting supported lipid bilayers

We investigated the effect of several stabilizing compounds on the topological structure of domain-forming planar supported bilayers after dehydration/rehydration. The chosen lipid composition of SM/cholesterol/DOPC 1:0.7:1 (molar ratio) corresponded to a point in the lipid phase diagram of coexistence of a liquid-disordered (L_d) phase and a liquid-ordered (L_o), raft-like phase (28,29). Figure 5.1 shows a typical topographical image of a SLB of such a composition. The examined samples were always reproducible and spatially homogeneous, with the exception of very few defects, which did not compromise the overall structure.

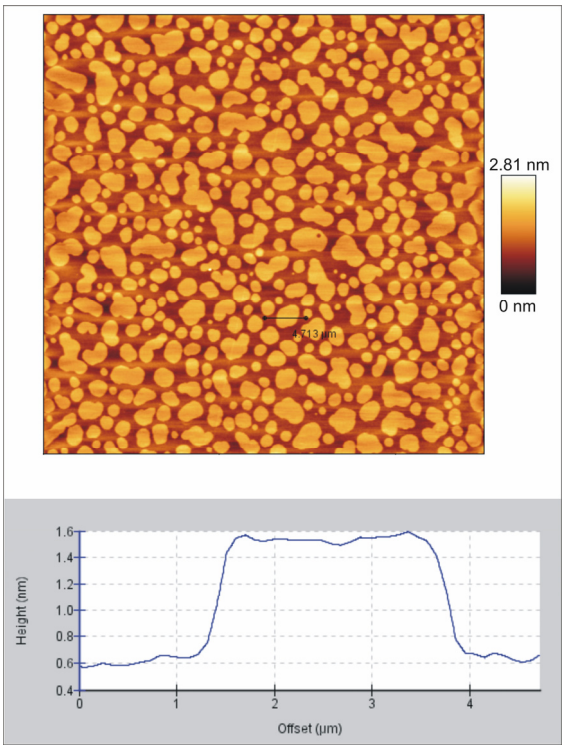

Figure 5.1 *AFM topographical image of a SLB composed of SM/cholesterol/DOPC (1:0.7:1 molar ratio) at room temperature. Bright and dark regions represent SM-rich and DOPC-rich domains, respectively. Note the full membrane coverage, without macroscopic defects, for the entire examined area (50 µm × 50 µm). The lower panel shows a cross section through one of the bright domains.*

Two different phases were clearly identified: one phase with well-defined, round microdomains, ~1 nm higher than the other lipid phase around (see Figure 5.1, lower panel). According to the phase diagram of the lipid mixture we used (29) and to the existing AFM data (30-32), the elevated domains corresponded to the L_o SM- and cholesterol-enriched domains, whereas the lower matrix was attributed to the L_d DOPC-enriched phase. To

confirm the phase assignment, we imaged the same sample by confocal fluorescence microscopy. In lipid bilayers of the above composition, the fluorescent marker DiD-C_{18} favors the DOPC-enriched phase over the SM-enriched one, as for the similar fluorescent probe DiI-C_{18} (35). Figure 5.2 shows, for the same part of the sample, a confocal image together with the AFM deflection signal image, which better evidences the contours of the microdomains (left panel).

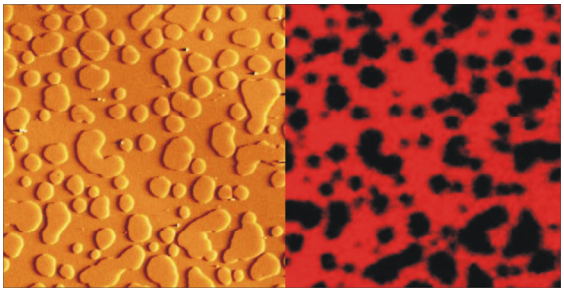

Figure 5.2 *AFM deflection signal (left) and fluorescence image (right) obtained from the same area (25 μm × 25 μm) of a SLB composed of SM/cholesterol/DOPC 1:0.7:1 (molar ratio). Note that higher domains in the AFM image perfectly overlap with the dark domains in the fluorescence image.*

By comparing the AFM and fluorescence images, it is evident that the higher domains shown in Figure 5.1 perfectly corresponded to the areas, from which the fluorescent marker DiD-C_{18} was excluded, thus confirming their assignment to the L_o phase. These images also demonstrated that the samples consisted of single supported bilayers. If this were not so, the fluorescence from DiD-C_{18} in the underlying bilayers would have been apparent in the dark areas of the upper bilayer, leading to a dramatic decrease or absence of the contrast between bright and dark areas.

To characterize the samples from a quantitative point of view, we analyzed several bilayers from independent samples by plotting the histograms of the height information. Figure 5.3 shows, on two different scales, the frequency of the height data for all of the collected images.

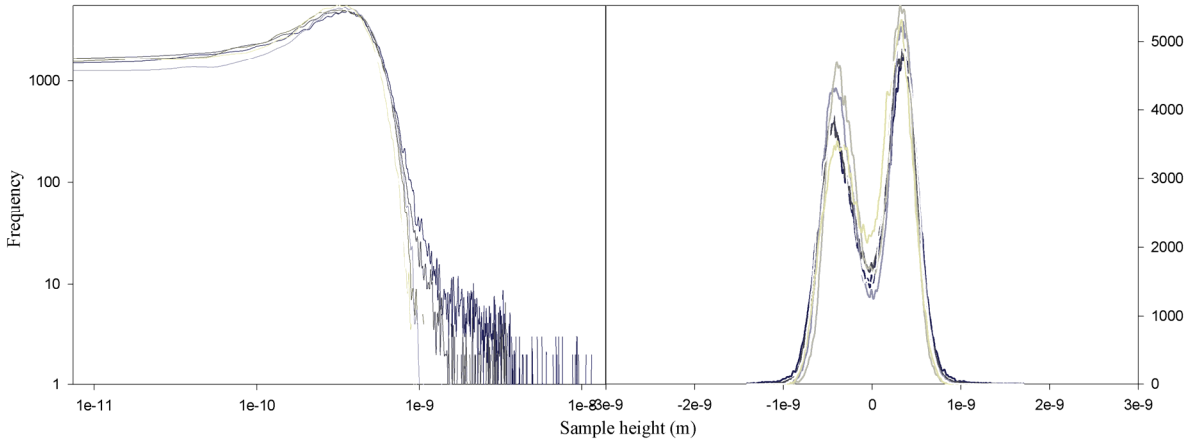

Figure 5.3 *Height histograms for all of the examined SLB composed of SM/cholesterol/DOPC 1:0.7:1 (molar ratio). Each curve refers to a 50 μm × 50 μm image. The left panel is in log-log scale and shows the maximum height observed for the samples. The heights of the two fluid phases are displayed with a linear scale in the histogram on the right panel. Two peaks, corresponding to two different topographical levels, were present in all of the examined samples.*

Note that the height data provided by the AFM are not absolute values when the bilayer covers the surface and the substrate underneath cannot be seen as a reference. It was therefore an arbitrary choice, for the histograms shown, to center the average height of the bilayers around 0 nm. From the left panel of Figure 5.3, we confirmed the absence of large aggregates or macroscopic imperfections in the bilayer, since the measured height is generally less than 10 nm. The right panel contains information about the height difference between the two lipid phases. The two peaks, which corresponded to the two discrete topographical levels of the SLB, were present at approximately the same height value in all of the examined samples and could be well fitted to a two-component Gaussian model. From the fitting, we computed a mean height difference between the phases of 0.71 ± 0.04 nm. The ratio between the area of the higher phase curve and the total area of the two peaks was on average 0.53 ± 0.02, representing a rough estimate of the ratio between the surface occupied by the L_o phase and the total surface of the sample. The microdomains showed a round, regular shape and can be clearly identified, although minor fusion events of very small domains were observed in the first hour. The number of round-shaped domains ranged between 275 and 450 within an area of 2500 μm^2, implying an average dimension of 3.0-4.8 μm^2.

5.3.2 Dehydration and rehydration of domain-exhibiting SLB without lyoprotectants

When dehydrated without any stabilizing substance and then rehydrated, all of the examined samples were highly inhomogeneous and showed extensive areas with major defects and structural damages. In Figure 5.4, two representative situations are shown, in which we could barely observe the phase coexistence and the entire morphology of the bilayer is very different from that prior to dehydration. As evident from the cross sections, the mica surface was uncovered in several areas of the samples (see Figure 5.4). Moreover, bulky and high structures, probably lipid aggregates, were often present on the surface.

This qualitative description was confirmed by the analysis of the height histograms, reported in 5.5. All of the curves, corresponding to independent samples, differed significantly from each other. In particular, the measured height reported in log-log scale (Figure 5.5, left panel) confirmed the presence of frequent irregularities and large, high aggregates in the SLB, with the maximum height being around hundreds of nanometers. For values of height around 0 nm, as represented on the right panel, the curves could not be fitted to a two-component Gaussian model. A few samples showed a separation between the peaks that could be attributed to the distance between the mica support and the bilayer (~5 nm). Others contained no recognizable structures or height difference pattern. The microdomains were no longer readily recognized as regular round-shaped features, as they seemed to enlarge and fuse, thereby forming larger and more irregular domains.

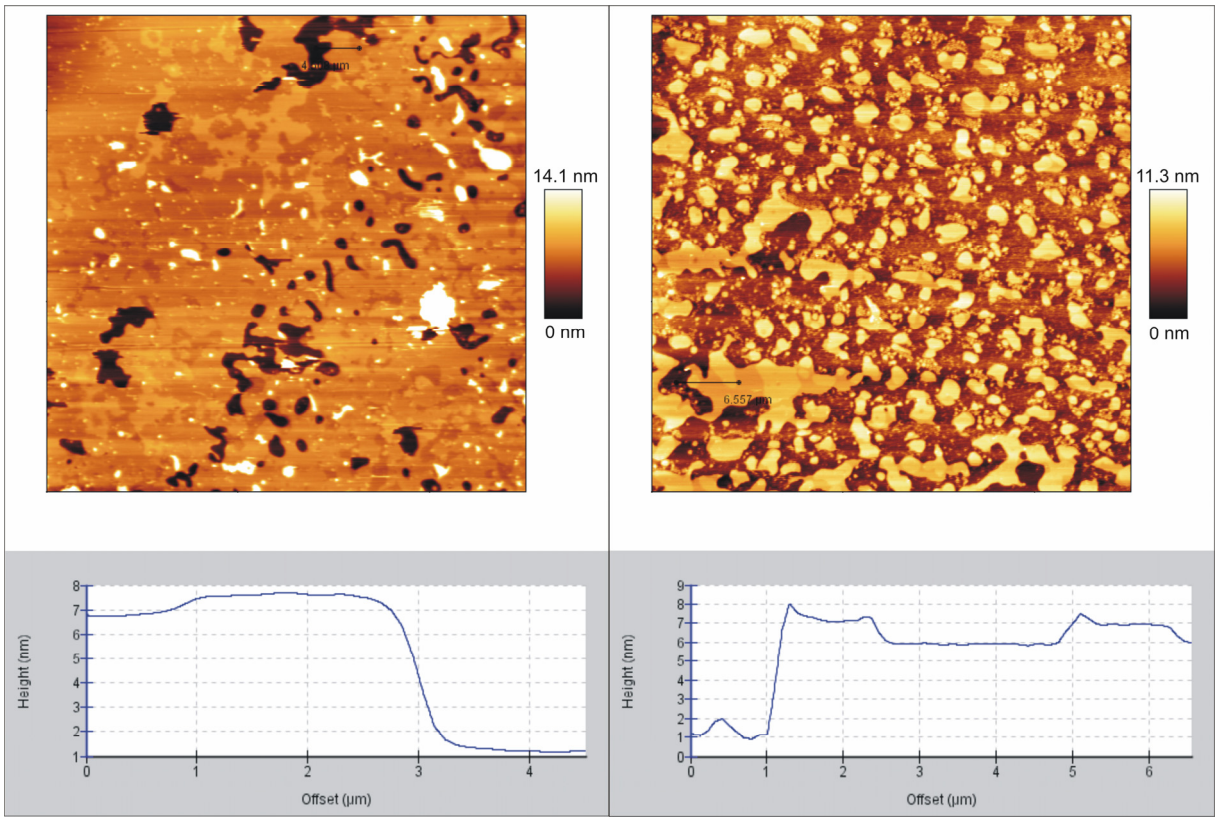

Figure 5.4 *Upper panels: typical 50 µm × 50 µm AFM images of SLP after dehydration and rehydration in the absence of lyoprotectants. The left one presents all the features together: large aggregates (the brightest areas), uncovered mica (the darkest areas), and irregular phase separation were present throughout the entire sample. The right panel shows an area where the mica support was almost completely uncovered leaving just patches of bilayer. Also in this case, phase separation was still observed. Lower panels: the cross sections of the previous images, with three different topographical levels: the mica support (~1-2 nm high), the DOPC-rich phase (~6-7 nm high) and SM-rich phase (~7-8 nm high).*

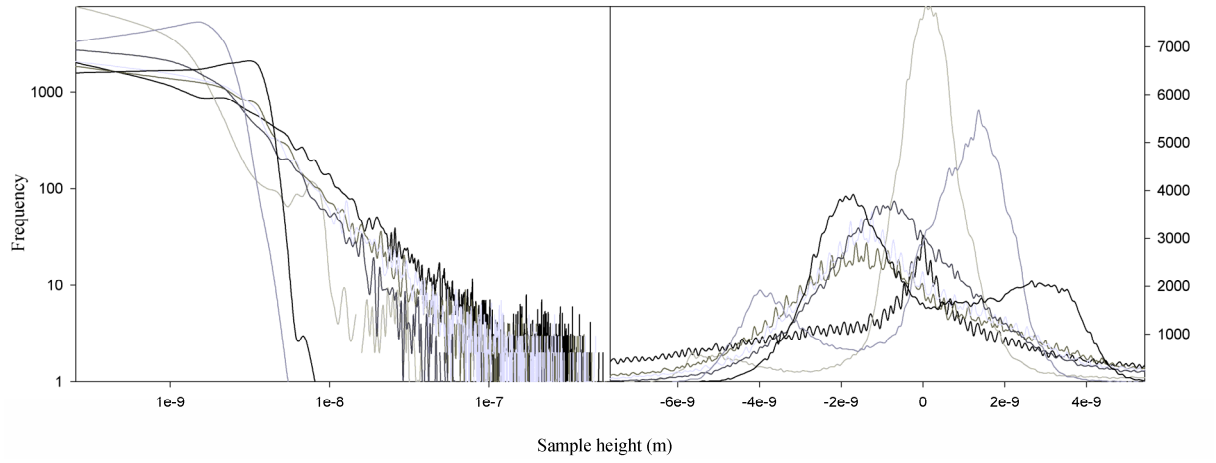

Figure 5.5 *Height histograms for all of the examined SLB composed of SM/cholesterol/DOPC 1:0.7:1 (molar ratio) after dehydration and rehydration in the absence of lyoprotectants. Each curve refers to a 50 µm x 50 µm image. The left panel gives an immediate picture of the inhomogeneity of the samples, as the shape of the curves is*

significantly different. Most of the samples contained topographical features, which are hundreds of nanometers high. Similarly, the hystograms for the area around the height of 0 nm (right panel) show major differences from the freshly prepared bilayers: some of them contained two peaks that could be ascribed to the mica and bilayer levels, whereas others showed no recognizable structure.

5.3.2 Effect of DMSO, glucose and dextran on dehydration and rehydration of domain-forming SLB

To check for the effects of nondisaccharide-based stabilizing substances, SLB composed of SM/cholesterol/DOPC 1:0.7:1 (molar ratio) were dehydrated in the presence of glucose, DMSO, or dextran and subsequently rehydrated. As shown in Figure 5.6, extensive damage on the bilayer structure and major changes on the domain morphology were present. As for the bilayer in the absence of protective compounds, lipid aggregates and large holes in the bilayer with uncovered mica were apparent, but not as frequently as for the untreated samples. It was possible to find, indeed, areas of the samples which were free of large imperfections. Domains could be observed, but they were much larger and of irregular shape compared to the freshly prepared bilayers, most likely as a result of fusion. The number of higher domains, indeed, was lower than that obtained in freshly prepared SLB samples. The corresponding height histograms are plotted in Figure 5.7, but the statistical analysis was difficult, as the curves could not be fitted to a unique model. Sometimes a single Gaussian was observed, usually related to the presence of high features in the image. In other cases, two peaks could be distinguished, representing either the separation between mica and bilayer or the lipid phase separation height step. Even in the latter case, the fitting results were not comparable to those obtained for freshly prepared samples (data not shown). The protective compounds tested here, thus, exhibited poor stabilizing effects on SLB, yielding similar results to those obtained without any added lyoprotectant.

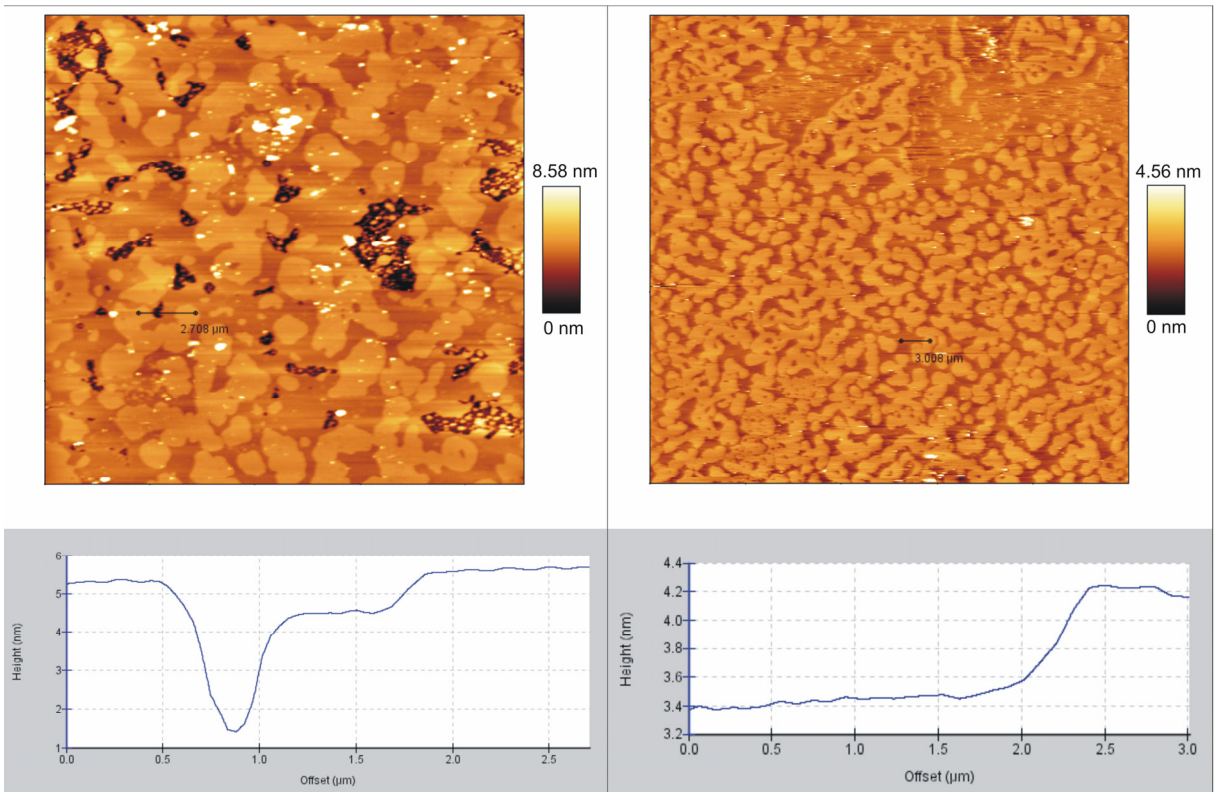

Figure 5.6 *Upper panels: typical AFM images of rehydrated SLB after dehydration and rehydration in the presence of DMSO. The samples treated with glucose or dextran all showed similar damage and defects, i.e., uncovered support and/or lipid aggregates. The left upper panel shows a larger area (50 µm × 50 µm) where no macroscopic imperfection is present. In the right upper panel (22.5 µm × 22.5 µm), the brightest spots correspond to lipid aggregates or dirt, the darkest zones are uncovered mica, and still phase separation is clearly recognizable. Lower panels: cross section for the previous described images.*

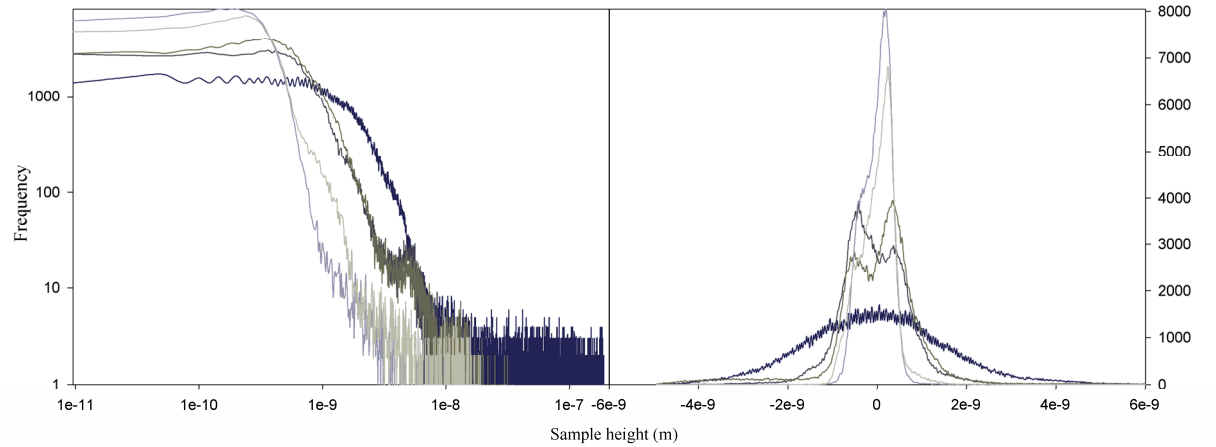

Figure 5.7 *Height histograms for all of the examined SLB composed of SM/cholesterol/DOPC 1:0.7:1 (molar ratio) after dehydration and rehydration in the presence of DMSO. Each curve refers to a 50 µm × 50 µm image and the overall appearance of the graphs is representative also for glucose and dextran samples. The left panel shows that high aggregates or imperfections of the SLB are present. The right panel shows the height distribution around the 0 nm value.*

5.3.3 Effect of trehalose and sucrose on dehydration and rehydration of domain-forming SLB

Finally, we tested the effect of disaccharides on the bilayer structure and domain morphology after dehydration and rehydration. Figure 5.8 shows typical AFM images of rehydrated SLB, after desiccation in the presence of trehalose or sucrose.

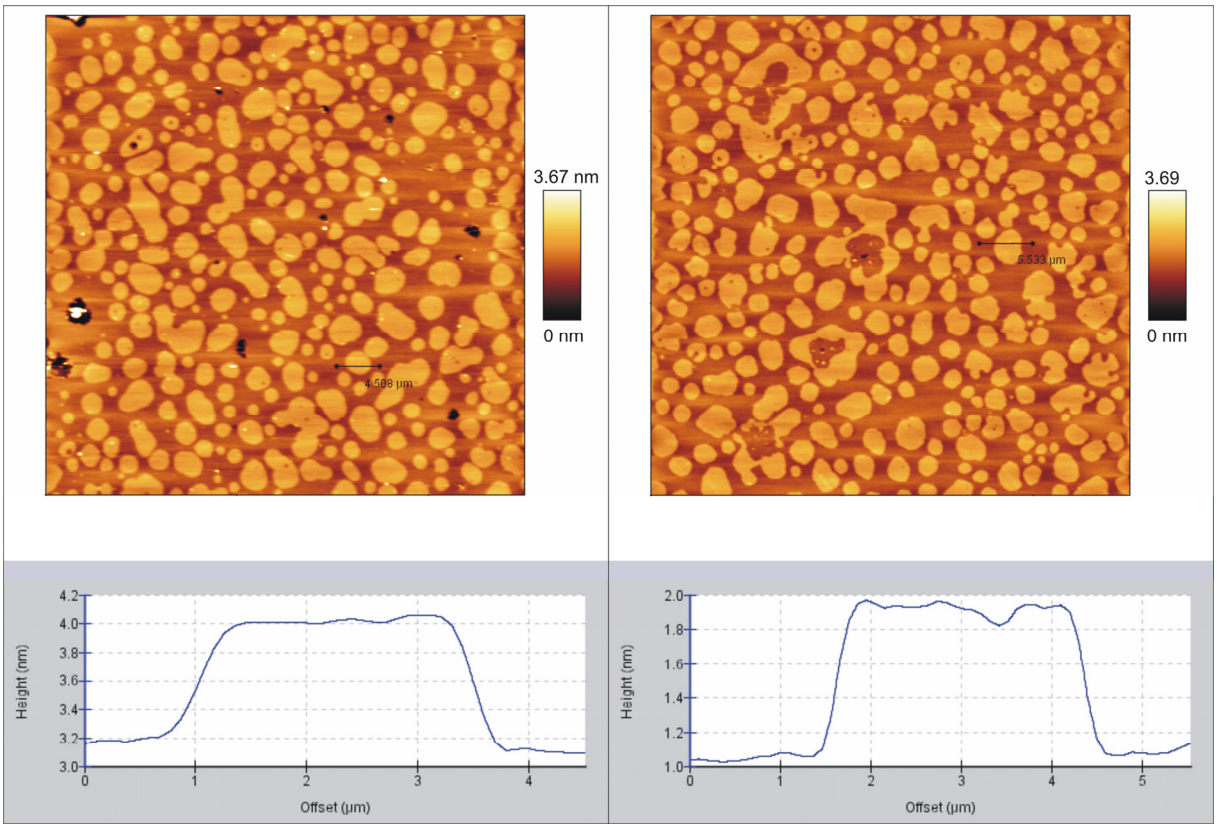

Figure 5.8 *The upper panels show typical 50 µm × 50 µm AFM images of SLB composed of SM/cholesterol/DOPC 1:0.7:1 (molar ratio) after dehydration in the presence of trehalose (left) and sucrose (right) and subsequent rehydration. The images are clearly comparable to those obtained for freshly prepared SLB. Lower panels: cross sections for the previous images.*

The samples were spatially homogeneous and reproducible, as in the freshly prepared samples. The small number of defects was also comparable to that found in fresh SLB. In contrast with the samples treated with nondisaccharides DMSO, glucose and dextran, rehydrated bilayers treated with trehalose and sucrose could be quantitatively characterized by the same statistical analysis for freshly prepared samples. The height histograms of the corresponding samples, shown in Figure 5.9, could always be fitted to a two-component Gaussian model.

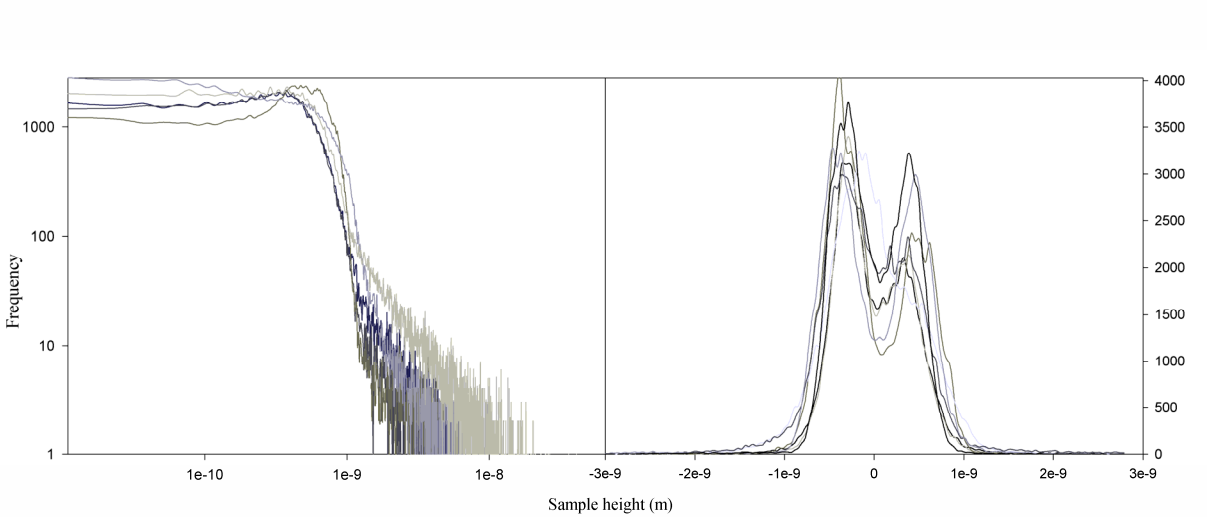

Figure 5.9. *Height histograms for all of the examined SLB composed of SM/cholesterol/DOPC 1:0.7:1 (molar ratio) after dehydration and rehydration in the presence of trehalose. Each curve refers to a 50 μm × 50 μm image. The overall appearance of the graphs is representative also for all of the sucrose samples. The left panel shows that high aggregates or defects were seldom found. The right panel shows the homogeneity of these samples: each histogram could be well fitted to a two-component Gaussian model, as for the freshly prepared SLB.*

In particular, the mean height difference between the phases was 0.71 ± 0.09 nm for trehalose and 0.74 ± 0.13 nm for sucrose. Regarding the percentage of surface covered by L_o domains, we obtained an average result of 0.44 ± 0.03 for trehalose and 0.43 ± 0.05 for sucrose. The microdomains could be clearly distinguished from each other, although the shapes were not always as regular as for the fresh sample. Their number ranges between 320 and 900, implying an average surface area of 1.0-3.5 μm^2 for trehalose samples, and between 260 and 360 for sucrose sample, with an average microdomain area of 3-4 μm^2.

5.4 Discussion

In the work described in this chapter, we used atomic force microscopy to study the effects of dehydration stress on domain-exhibiting supported bilayers for the first time. The observations lead to a quantitative difference, in terms of stabilization efficiency, between disaccharides and other nondisaccharide-based cryo/lyo protectants. In particular, our study showed very good stabilization of both the bilayer structure and the domain morphology by using sucrose or trehalose, whereas poor results were obtained with DMSO, glucose, or dextran. The use of these last three compounds resulted in a moderate protection of the bilayer, probably due to the presence of a transparent glassy film, which only partially avoided the formation of bulky aggregates or large areas of uncovered mica. These findings are in agreement with previous studies (20), which analyzed the efficiency of several stabilizing substances in preserving the integrity of liposomes during freeze-thawing or freeze-drying treatment. Compared to the freezing treatment, protection against drying seemed to be a more complex phenomenon, which could be successfully achieved only by using disaccharides. These substances were, indeed, the only ones among those examined in

these studies providing protection to egg phosphatidylcholine liposomes during drying. On the other hand, in the case of dipalmitoylphosphatidylcholine liposomes, other glass-forming substances, like dextran, were able to protect lipids against desiccation, even though to a lesser extent than trehalose (21). This implies that, for saturated lipids, vitrification could be more effective than the molecular interaction between sugar and the lipid headgroups, thereby playing an important role in liposome stabilization. As a consequence, although protection against drying and freezing may be regulated by the same basic mechanism, important differences between these two damaging conditions have been observed. Further investigations are needed for a more detailed understanding of the molecular interactions between lipids and lyoprotectants. In contrast to previous reports, in this work, we attempted to mimic more closely cellular membranes and, hence, analyzed membranes that contain saturated lipids (SM) mixed with cholesterol and unsaturated lipids (DOPC) and exhibit domain formation (L_d and L_o coexisting phases). Our data show that, in membranes of such composition, vitrification is not very efficient in protection against drying (cf. Figures 5.6 and 5.8). In fact, a more effective stabilization of such heterogeneous membranes was obtained only with disaccharides, thereby involving mechanisms at both macroscopic (vitrification) and microscopic (sugar-lipid headgroup interaction) levels.

Previous studies by FTIR spectroscopy on dilaureoyl- and distearoylphosphatidylcholine liposomes, which exhibit coexistence of gel-phase and L_d phase, revealed the efficiency of trehalose in preventing dehydration damage on more complex model membranes (26). When liposomes were dried without trehalose, full mixing of the lipid components occurred. In the presence of trehalose, instead, the lipid phase separation was maintained during drying. A similar mechanism could be involved in the stabilization of microdomains in native membranes during drying with trehalose.

Such a phenomenon has been investigated for blood platelet membranes. During chilling, platelet membrane lipids undergo a phase transition from liquid crystalline to gel phase, around 10-20 °C (33). The immediate consequences are leakage of the cell content and extensive lateral phase separation of membrane phospholipids. These events led to damages that make cold stored platelets clinically useless (24). Furthermore, Gousset et al. (34) suggested that chilling and phase separation are related to the lateral organization of preexisting, small L_o microdomains in platelet membranes. It is worth noting that the presence of rafts prior to chilling is plausible but could not be proven. By fluorescence imaging, they observed extensive aggregation of membrane components into large domains upon a decrease of the temperature. The same large membrane patches were observed when platelets were activated by thrombin, as this compound induces extensive lateral phase separation and, eventually, aggregation of microdomains. It was then proposed that chilling, as well as drying treatments, brings about aggregation of small rafts into macroscopical domains and, therefore, inappropriate platelet activation, which should be avoided for a successful storage of these cells (24). This goal has been achieved by drying platelets in the presence of trehalose, before storage (25). It is relevant to point out that, in the cited work, the ratio between the mass of the sugar and that of the lipids is roughly comparable to what we used for our experiments (~50-100). The mechanism is not fully understood yet, but it can be assumed that trehalose stabilizes the L_o microdomains, thus preventing their fusion or aggregation. Our measurements support this assumption, giving a visual proof of the enlargement of L_o domains when the membrane is dried in the absence of disaccharides. Although the support might, in general, influence the lipid organization in the bilayer, the goal of this work was to investigate the relative effect of substances on the same bilayer under the same experimental conditions. This implies that the large differences observed among different lyoprotectants are independent of the underlying support.

We show that the protection against desiccation by non-disaccharide-based compounds is rather poor, either concerning the overall structure of the bilayer or concerning the

morphology of the L_o, raftlike domains. By contrast, the presence of disaccharides inhibits nonspecific fusion of the domains, thereby stabilizing their size and boundaries. We did not observe any reproducible specific difference between the effect of trehalose and that of sucrose, but we are currently investigating this aspect in more detail.

Finally, our findings confirm that the protective action of disaccharides could be a two-fold. First, they could preserve the structural/macroscopic integrity of the membrane as a whole through the formation of a glassy solid which prevents the formation of holes or big aggregates (thereby inhibiting leakage and fusion in vivo). As our results show, this specific effect could be exerted by stabilizing substances other than disaccharides but not with the same efficiency. Furthermore, disaccharides can also maintain the phase separation and the integrity of microdomains, thereby preventing their aggregation and the consequent damages in living cells.

5.5 Conclusions

In the work described in this chapter, we established a method to study phase separation in supported lipid bilayers using a combination of AFM and laser scanning fluorescence microscopy. Furthermore, we have applied AFM as a new method for visualizing the dehydration damage on model membranes. In particular, AFM allows for a direct visualization of the effects of water removal on liquid-ordered microdomains, either in the presence or in the absence of lyoprotectants. We showed how effective disaccharides are from a macroscopic point of view, by preserving the overall integrity of the supported bilayers, and also from a microscopic point of view, by preventing fusion and enlargement of microdomains, which is connected to biological damage in living cells.

5.6 References

1. Crowe, J. H.; Crowe, L. M.; Chapman, D. *Science* **1984**, *223*, 701-703.
2. Crowe, J. H.; Hoekstra, F. A.; Crowe, L. M. *Annu. Rev. Phys.* **1992**, *54*, 579-599.
3. Bianchi, G.; Gamba, A.; Murelli, C.; Salamini, F.; Bartels, D. *Plant J.* **1991**, *3*, 355-359.
4. Hoekstra, F. A.; Crowe, L. M.; Crowe, J. H. *Plant Cell Environ.* **1989**, *12*, 83-91.
5. Womersley, C.; Uster, P. S.; Rudolph, A. S.; Crowe, J. H. *Cryobiology* **1986**, *23*, 245-255.
6. Satpathy, G. R.; Torok, Z.; Bali, R.; Dwyre, D. M.; Little, E.; Walker, N. J.; Tablin, F.; Crowe, J. H.; Tsvetkova, N. M. *Cryobiology* **2004**, *49*, 123-136.
7. Wolkers, W. F.; Walker, N. J.; Tablin, F.; Crowe, J. H. *Cryobiology* **2001**, *42*, 79-87.
8. Oliver, A. E.; Jamil, K.; Crowe, J. H.; Tablin, F. *Cell Preserv. Technol.* **2004**, *2*, 35-49.
9. Carpenter, J. F.; Crowe, J. H. *Biochemistry* **1989**, *28*, 3916-3922.
10. Crowe, J. H.; Crowe, L. M.; Carpenter, J. F. *Biochem. J.* **1987**, *242 (1)*, 1-10.
11. Crowe, J. H.; Crowe, L. M. *Cryobiology* **1982**, *19 (3)*, 317-328.
12. Crowe, J. H.; Crowe, L. M.; Jackson, S. A. *Arch. Biochem. Biophys.* **1983**, *220 (2)*, 477-484.
13. Carpenter, J. F.; Prestrelsky, S. J.; Anchordoguy, T. J.; Arakawa, T. In *Formulation and Delivery of Proteins and Peptides*; Cleland, J. L., Langer, R., Eds.; American Chemical Society: Washington, DC, 1994; p 134-147.
14. Cottone, G.; Ciccotti, G.; Cordone, L. *J. Chem. Phys.* **2002**, *117 (21)*, 9862-9866.
15. Belton, P. S.; Gil, A. M. *Biopolymers* **1994**, *34*, 957-961.
16. Koster, K. L.; Webb, M. S.; Bryant, G. *Biochim. Biophys. Acta* **1994**, *1193*, 143-150.
17. Bryant, G.; Wolfe, J. *Cryo-Lett.* **1992**, *13*, 23-26.
18. Crowe, J. H.; Oliver, A. E.; Tablin, F. *Integr. Comput. Biol.* **2002**, *42*, 497-503.
19. Clegg, J. S. *Comput. Biochem. Physiol.* **2001**, *128B*, 613-624.
20. Crowe, J. H.; Carpenter, J. F.; Crowe, L. M. *Cryobiology* **1990**, *27 (3)*, 219-231. 21. Crowe, J. H.; Leslie, S. B.; Crowe, L. M. *Cryobiology* **1994**, *31*, 355-366.
22. Simons, K.; Ikonen, E. *Nature (London)* **1997**, *387 (6633)*, 569-572.
23. Mayor, S.; Rao, M. *Traffic* **2004**, *5*, 231-240.
24. Tablin, F.; Wolkers, W. F.; Walker, N. J. *Cryobiology* **2001**, *43 (2)*, 114-123.
25. Wolkers, W. F.; Walker, N. J.; Tablin, F.; J. H. Crowe *Cryobiology* **2001**, *42 (2)*, 79-87.
26. Ricker, J. V.; Tsvetkova, N. M.; Wolkers, W. F.; Leidy, C.; Tablin, F.; Longo, M.; Crowe J. H. *Biophys. J.* **2003**, *84*, 3045-3051.
27. Giuffrida, S.; Cottone, G.; Cordone, L. *J. Phys. Chem. B* **2004**, *108*, 15415-15421.
28. De Almeida, R. F. M.; Fedorov, A.; Prieto, M. *Biophys. J.* **2003**, *85*, 2406-2416.
29. Kahya, N.; Scherfeld, D.; Bacia, K.; Poolman, B.; Schwille, P. *J. Biol. Chem.* **2003**, *278*, 28109-28115.
30. Berquand, A.; Mingeot-Leclercq, M. P.; Dufrene, Y. F. *Biochim. Biophys. Acta* **2004**, *1664 (2)*, 198-205.
31. Milhiet P. E.; Domec, C.; Giocondi, M.; Van Mau N.; Heitz, F.; Le Grimellec, C. *Biophys. J.* **2001**, *81*, 547-555.
32. Rinia H. A.; Snel M. M. E.; van der Eerden J. P. J. M.; de Kruijff, B. *FEBS Lett.* **2001**, *501*, 92-96. 33. Leidy, C.; Gousset, K.; Ricker, J.; Wolkers, W. F.; Tsvetkova, N. M.; Tablin, F.; Crowe, J. H. *Cell Biochem. Biophys.* **2004**, *40 (2)*, 123-148
34. Gousset, K.; Wolkers, W. F.; Tsvetkova, N. M.; Oliver, A. E.; Field, C. L.; Walker, N. J.; Crowe, J. H.; Tablin, F. *J. Cell. Phys.* **2002**, *190 (1)*, 117-128.
35. Kahya, N. Unpublished results.

Chapter 6 – Ceramide and reorganization of cell membranes

6.1 Introduction

Rafts are most often defined as lateral assemblies enriched in sphingolipids and cholesterol, and they are possibly stabilized both by hydrogen bonds among the polar heads and by hydrophobic interactions among the long saturated aliphatic chains of the sphingolipids. According to the early model proposed by Simons and Ikonen (1-5), the defects in the sphingolipid packing are successfully filled by cholesterol, which also interacts with their hydrophobic moieties. The resulting tight interactions lead to the separation of cholesterol- and sphingolipid- enriched microdomains from the rest of the lipids in the membrane (6). The most common sphingolipid found in eukaryotic membranes is sphingomyelin (SM), which is composed of a hydrophilic phosphorylcholine headgroup and a hydrophobic ceramide backbone. Ceramide (Cer) is a sphingolipid itself, with a sphingosine base linked via its amino group to a fatty acid chain, and it is considered an important signaling molecule in biological processes like senescence, apoptosis, immune response, bacterial and viral pathogenesis, and cell-cycle arrest (7, 8, 9). This molecule can be produced in cells either via *de novo* synthesis or through hydrolysis of SM phosphocholine group, mediated by sphingomyelinase (SMase) (10). In response to specific stimuli, ceramide concentration in physiological contexts can reach 10-20% of the total lipid content (8 and references therein, 11).

Interestingly, the biophysical properties of ceramide strongly influence both the structural organization and the dynamical properties of the cell membrane. First, ceramides are able to form large networks of hydrogen bonds, as their polar head can act both as an acceptor and donor. Moreover, they are among the most hydrophobic lipids in nature and their phase behavior, which exhibits a melting event at around 90°C, is rather peculiar if compared to the other lipids commonly found in biological membranes. These two properties together explain the tendency of ceramides to segregate from other lipids, thereby generating highly ordered ceramide-enriched microdomains (7, 9, 12). Furthermore, given the small size of its polar headgroup, ceramide is classified as a lipid with negative curvature. It can thus significantly affect the overall membrane curvature and stability, for example by promoting the lamellar-hexagonal phase transition, pore formation, membrane fusion and vesicle budding (13-15). Another intriguing property of ceramides concerns their interaction with cholesterol and SM, and the possible consequences on raft assembly. Within this context, a clear relationship has been established between ceramide generation and the decreased level of cholesterol in the plasma membrane (16). Ito et al. (17) reported that the amount of cholesterol in detergent-resistant membrane fractions of rat astrocytes decreases as a consequence of treatment with SMase. It was then proposed that the displacement of cholesterol from the plasma membrane is the result of ceramide-induced displacement of cholesterol from rafts (18). The concept of cholesterol displacement was supported by differential scanning calorimetry and fluorescence spectroscopy studies on lipid vesicles containing co-existing raft and liquid-disordered domains (18-20). It was shown that both natural and synthetic ceramides displace raft-associated cholesterol. The reason could be the competition of ceramide and sterols for inclusion in L_o domains. As an alternative scenario, the presence of distinct ceramide-enriched domains that cannot accommodate sterol molecules might force the latter to dissolve into the disordered phase (18). So far, it is not clear yet whether, in the presence of ceramides, L_o domains exhibit a homogenous lipid composition or whether different domains of chemically distinct composition segregate.

In this chapter, we describe the use of a combined approach of AFM, fluorescence imaging and FCS (21,22) to shed light on the effects of ceramides on the bilayer structure and dynamic organization in domain-exhibiting model membranes with lipid compositions which are relevant to the raft problem.

Our results show that physiological concentrations of ceramide strongly influence the lateral organization of the membrane. More specifically, ceramide-enriched areas are formed in correspondence with raft-like domains, which thus experience major structural rearrangements. Furthermore, dynamic data support the hypothesis by which raft reorganization is accompanied by the release of cholesterol into the disordered phase. Similar results are finally obtained by adding SMase to supported bilayers composed of SM/DOPC/cholesterol 1:1:0.7 (molar ratio).

6.2 Experimental Procedures

6.2.1 Chemicals

For a complete list of the chemicals used for the experiments described in this chapter, see also section 4.2.1. Sphingomyelinase (SMase) from *Staphylococcus aureus* sp was purchased from Molecular Probes (Eugene, OR).

6.2.2 Supported Lipid Bilayers (SLB)

Planar bilayers were prepared as already described in section 4.2.2. (23). Briefly, lipids and fluorescent dyes were mixed in organic solutions in different proportions. The lipid composition was DOPC:Cholesterol:(SM+Cer) 1:0.7:1 (molar ratio), whereas the concentration of the dyes was either 0.1% or 0.005% molar, depending on the technique used. The total molar fraction of sphingolipids was kept constant (37%), but the SM/Cer stoichiometry was varied. After solvent evaporation, the lipid film thus obtained was rehydrated using buffer A at 10 mg/mL lipid concentration and resuspended through vigorous vortexing. After sonicating the suspension at 60 °C, a small aliquot was diluted in buffer B and deposited on a ~20 μm thick, freshly cleaved piece of mica, glued to a glass coverslip. The sample was then left at room temperature for 30 minutes and at 70 °C for 10-15 additional minutes. After that, the SLB was rinsed at least 10 times with buffer C and then allowed to cool down to room temperature, before being transferred to the microscope. Samples containing more than 13 mol% ceramide were unstable after ~3 h. For this reason, all the measurements were performed ~90 min. after the cooling phase.

6.2.3 AFM, Confocal Fluorescence Microscopy and FCS.

AFM, fluorescence imaging and FCS were all performed at room temperature (~23°C) on the same experimental apparatus. It consisted of a NanoWizard AFM (JPK Instruments, Berlin, Germany) mounted on a LSM 510 Meta (Zeiss, Jena, Germany). The fiber output was coupled to a home-built FCS detection unit, consisting of an emission filter and an achromatic doublet (Linos Photonics, Goettingen, Germany) to image the internal pinhole onto the optical fiber connected to an avalanche photodiode (APD) (PerkinElmer, Boston, MA). Correlation curves were obtained with a hardware correlator (Correlator.com, Bridgewater, NJ). Unless

otherwise specified, a typical measurement consisted of the following steps: i) check sample integrity and homogeneity through fluorescence imaging of a large area (~200x200 μm); ii) choose a suitable area and positioning the cantilever tip; iii) acquire both the AFM topographic image and the fluorescence image and, finally, iv) choose a spot on the sample and perform FCS.

For AFM imaging, uncoated silicon cantilevers (MikroMasch, Spain) with typical spring constant of 0.03 N/m (manufacturer specified) were used. During measurements the SLB was always covered with 0.5 mL of buffer 3. Contact mode topographic images were collected in the constant-deflection mode, the scan rate being set between 0.9 and 1.5 Hz, and the force was maintained at the lowest possible value, by continuously adjusting the set point during the measurement. Images were collected at 512x512 or 256x256 pixel resolution and were line-fitted as required with 1^{st} or 2^{nd} order polynomial.

For confocal fluorescence microscopy, the excitation light of a HeNe laser at 543 nm was reflected by a dichroic mirror (HFT KP 700/543) and focused onto the sample by a Zeiss C-Apochromat 40x, NA=1.2 UV-VIS-IR water immersion objective. Fluorescence signal was then recollected by the same objective and, after passing through a 580/40 bandpass filter, measured by a photomultiplier (PMT). The confocal geometry was ensured by a 78 μm pinhole in front of the PMT.

FCS measurements were performed using the same optical path described for the fluorescence imaging, the signal from the sample being collected in this case by the APD in the FCS unit. The optimal laser power, which produced a good signal-to-noise ratio without any bleaching or saturation effect, resulted to be ~10 μW. The laser focus was initially positioned a few hundreds of nm below the z-position which gave the maximum signal intensity and, subsequently, the fluorescence temporal signal was recorded at different z positions, moving the objective upwards step by step. The z-scan always covered a range of ~1.5 μm around the membrane, with steps of 0.2 μm. At each step, the signal was collected in 3 runs of 10 seconds each, and the correlation function $G(\tau)$ was calculated, as elsewhere described (24). Data analysis was performed with a software written in Matlab (Mathworks, Natick, MA) obtaining, for each z position, the average number of particles in the focal volume NP(z) and the corresponding diffusion time $\tau_D(z)$. The final τ_D was chosen in correspondence to the minimum of NP(z). All the FCS data reported are the result of at least 6 measurements for each sample and 2 independent sample preparations.

Due to the presence of the mica glued onto the coverslip, the absolute calibration of the apparatus can be challenging, since the focal volume may be distorted and/or enlarged. We used two methods to estimate the radius of the detection area w_0 on the focal plane. First, we measured the three-dimensional diffusion coefficient of Alexa-546 freely diffusing in the buffer. Assuming a Gaussian detection volume, w_0 was found to be between 0.24 and 0.32 μm. Secondly, fitting the values of NP(z) and $\tau_D(z)$ to a simple parabolic model, which takes into account the shape and the dimensions of the focal volume, yielded an alternative estimate of the parameter w_0 (see paragraph 2.4 and Ref. 25). This method resulted in an average value of $w_0 = 0.29 \pm 0.03$ μm, in good agreement with the previous estimate.

6.2.4 Giant Unilamellar Vesicles (GUVs)

GUVs were prepared with the electroformation method (25b). Using this approach, unilamellar vesicles are produced with diameter ranging from 5 to 100 μm. The perfusion chamber (closed-bath perfusion chamber, RC-21, Warner Instruments Co., Hamden, CT) used for vesicle preparation was equipped with two microscope slides, each coated with indium-tin oxide (ITO), which is electrically conductive and exhibits high light transmission in the visible range. DOPC, SM, and cholesterol were dissolved in chloroform at 1:1:0.67 molar

ratio and 15mM total concentration. The solvent was then evaporated directly on the ITO slides, thereby producing a thin lipid film. GUVs were grown in the perfusion chamber at high temperature (65 ◦C) in presence of water, as a result of lipid swelling under an AC field. After GUV formation, the chamber was slowly cooled down to room T. 60 mU of SMase from *Staphylococcus aureus* sp were injected in the perfusion chamber after the cooling phase and preliminary imaging of the GUVs. DiD and a Bodipy free-cholesterol analogue (BODIPY-FChol, synthesized as described in Ref. 25c) were added in the amount of 0.1 mol% for fluorescence imaging.

Confocal fluorescence microscopy was performed using multitrack mode. Light from an Ar-laser at 488nm and a He-Ne laser at 633nm was reflected with a HFT UV/488/543/633 dichroic. A 40x NA 1.2 C-Apochromat water immersion objective was used, and the pinhole size was set to 70 and 90 μm in the green and red channel respectively. Emitted fluorescence was separated with a NFT 570 dichroic and passed through 530/30 nm or 650nm long pass filters to be finally detected with a PMT.

6.3 Results

6.3.1 The structure of the bilayer is strongly influenced by ceramide

Supported lipid bilayers were prepared with different ceramide contents and their topographical features were examined using atomic force microscopy. The samples were stable for at least 3-4 hours. Over longer times, the presence of ceramide affected the overall stability of the bilayer, resulting in the formation of holes, especially at concentrations higher than 12 mol%. Figure 6.1 shows typical images obtained for samples containing 0, 4, 9, 13, 18 mol% of Cer.

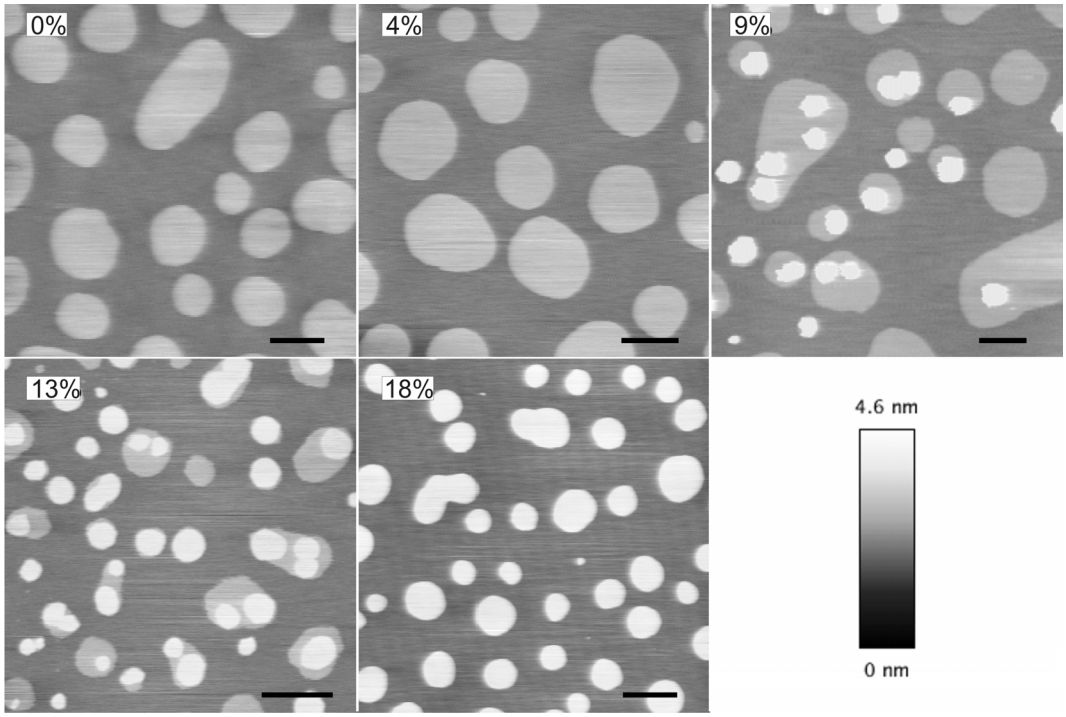

Figure 6.1 *AFM topographical images of SLB at different Cer concentrations, at room temperature. The lipid composition was DOPC:cholesterol:(SM+Cer) 1:0.7:1 molar and SM was gradually substituted for ceramide. In the 0% and 4% samples, two different phases with a height step of ca. 0.8 nm can be readily distinguished. In all of the remaining images, a third topographical level can be identified at ca. 1.2 nm above the surrounding lowest phase. Scale bar = 2 μm.*

Samples containing 0% or 4% of Cer appeared very similar and consistent with previous results obtained for SM/Cholesterol/DOPC 1:0.7:1 SLB, in the absence of Cer (23). For this lipid composition, coexistence of L_d phase and L_o, raft-like phase is expected. The domain structural features and lipid composition have been already characterized in previous studies (21, 23, 26 and references within). The light-colored round domains in the first two images in figure 6.1, which presented very regular shapes and were ~0.8 nm higher than the surrounding matrix, thus corresponded to the SM-rich ordered phase. Conversely, the darker areas in these images corresponded to the DOPC-rich disordered phase. At 9% Cer, a third topographical level could be clearly identified, being almost 0.4 nm higher than the liquid-ordered phase. These new domains had a diameter of ~1 μm and were always localized in the SM-rich domains, either in the interior or at the domain boundaries.

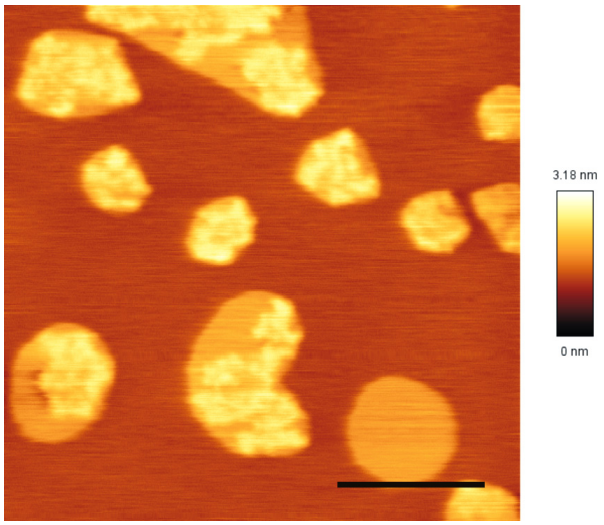

Figure 6.2 *AFM topographical image of a SLB made of DOPC/cholesterol/SM/Cer 1:0.7:0.76:0.24 molar (9% Cer) at room temperature. Three different phases can be readily distinguished at a relative height of 0, 0.6 and 1 nm ca. The first two most likely correspond to the liquid-disordered and liquid-ordered domains respectively. The lightest phase presents irregular features and contours. Scale bar = 2 μm.*

As evident from figure 6.2, higher resolution imaging of the sample revealed a complex structure of these sub-domains. Their shape was not as regular as that of the liquid-ordered domains and their height was not constant. An increase in the ceramide content resulted in an enlargement of the surface occupied by the new high domains, up to 18% Cer, where the lower round domains could not be observed anymore and again only two different topographic levels were distinguished. Samples containing 24 mol% Cer, though highly unstable, showed no further relevant modification of the microdomain internal structure (data not shown).

Finally, figure 6.3 summarizes the topographical features of all the examined samples. In the upper panel, the height differences between the different types of domains and the lowest topographic level are represented.

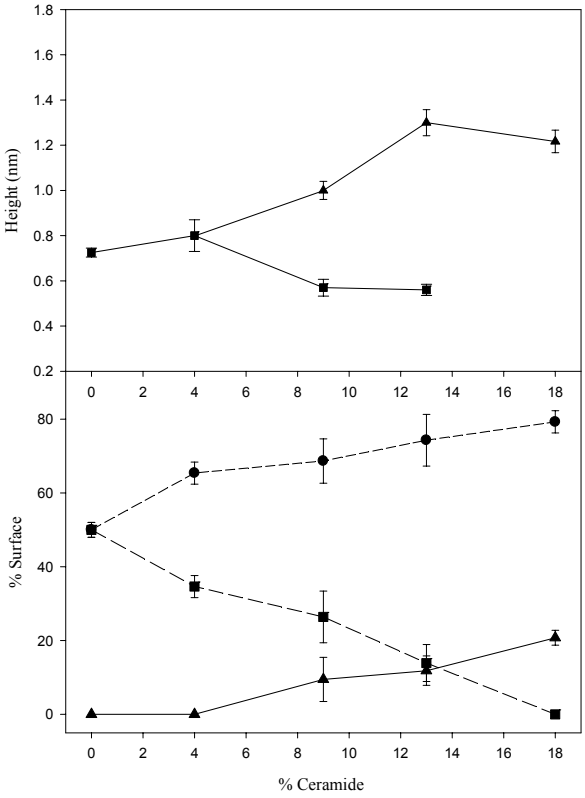

Figure 6.3 *Topographical features of ceramide-containing SLBs. In the upper panel, height differences between the domains at the intermediate height and the surrounding lipid matrix (squares) and between the highest domains and the surrounding lipid matrix (triangles), as a function of ceramide content. In the lower panel, surface fraction occupied by the lowest phase (circles), intermediate phase (squares) or highest phase (triangles), as a function of ceramide content. Error bars represent the standard deviations of the measurements.*

At 0% and 4% only one height step was observed, at ~0.8 nm. At 9% and 13% Cer, as already mentioned, two different steps were observed: the lower one at ~0.6 nm and the higher one at ~1.0 and ~1.2 nm. Finally, at 18% ceramide, again only two phases were present, with constant step of ~1.2 nm. The lower panel represents the surface percentage occupied by each phase, as a function of the ceramide content. The examined samples showed a clear monotonic trend connected to increasing quantities of ceramide: the intermediate-height phase occupied a portion of the surface which steadily decreased, down to complete disappearance. On the other hand, both the lowest and highest phase steadily enlarged, up to 18% Cer, where the former occupied ~80% of the sample surface.

Note that fluorescence imaging did not provide complete information about the lateral organization of the bilayer. This is evident in figure 6.4, which shows, on the left panel, confocal fluorescence images for typical 13% and 4% Cer samples, containing 0.1% RhoPE. Comparison with AFM data, shown on the right panel of figure 6.4, revealed that the dark patches correspond to two distinct lipid phases. This implies that the lipid analog RhoPE partitions almost exclusively into the lowest phase, leaving the intermediate-height domains and the highest ones completely dark. Consequently, fluorescence imaging only allows for a partial characterization of the lateral organization of the membrane. The same results were obtained using Bodipy FL C_5-ceramide, Bodipy FL DHPE and DiD-C_{18} (data not shown).

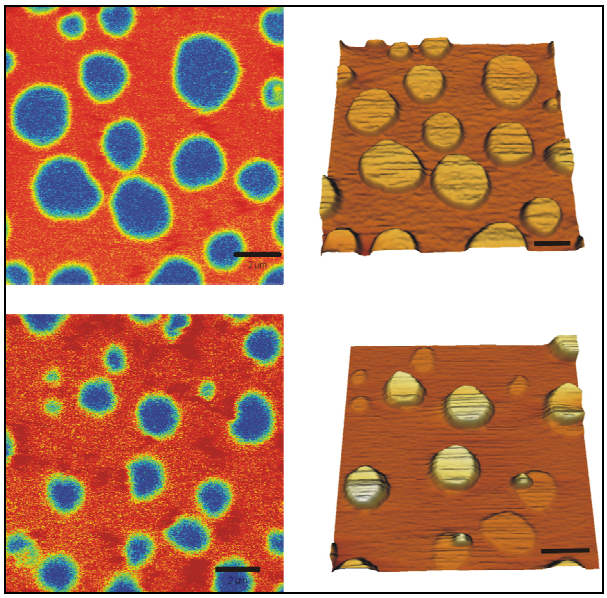

Figure 6.4 *Fluorescence image (left) and AFM topographical data (right) acquired on the same spot of the membrane at room temperature. The upper panel refers to a DOPC/cholesterol/SM/Cer 1:0.7:0.88:0.12 sample (4% Cer), the lower panel to a DOPC/cholesterol/SM/Cer 1:0.7:0.64:0.36 sample (13% Cer). The fluorescent lipid RhoPE was added at 0.1% molar concentration in the lipid mixture.*

6.3.2 Dynamic properties of supported lipid bilayers in presence of ceramide

In order to obtain information about the local dynamics in the different lipid phases, we performed FCS measurements and AFM micromanipulation on ceramide-containing SLBs. More specifically, the AFM tip was used to deform the ordered domains and monitor the process of relaxation back to the original shape. FCS was applied to probe the Brownian diffusion of fluorescent lipids analogs in the ld phase, as a function of the ceramide content. The laser was always focused in a sub-microscopic spot onto the lowest lipid phase of the bilayer, at least 3µm away from the other domains. The accurate x-y positioning was previously determined by both fluorescence and AFM imaging. Figure 6.5 shows typical autocorrelation curves, measured in three different samples.

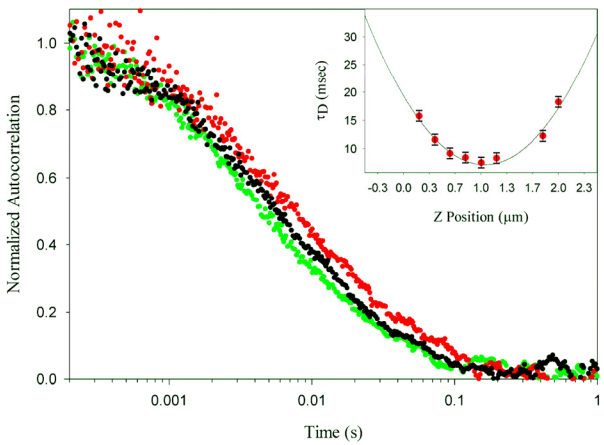

Figure 6.5 *Typical averaged autocorrelation curves, measured in the DOPC-rich phase for three different samples containing 0% (green), 9% (black) and 18% (red) ceramide. The fluorescent lipid RhoPE was included in 0.005% molar concentration. All measurements were performed at room temperature. For each ceramide content, the final diffusion times τ_D were computed from the analysis of ca. 140 curves: 3 autocorrelation curves, at ~8 different z positions in 6 independent measurement spots. Inset: Diffusion times τ_D for different heights z of the detection volume (18% ceramide). Diffusion times were obtained by fitting the autocorrelation curves to a one-component two-dimensional Brownian diffusion model. Solid line: fit to second order polynomial to determine the minimum diffusion time.*

It is worth noting that the presence of bright, slow diffusing non-fused liposomes or aggregates can cause severe distortion of the autocorrelation curves. Scanning the AFM tip on the sample, with appropriate force and speed, can sweep away the undesired fluorescent particles, thus allowing a reproducible fluorescence data acquisition.

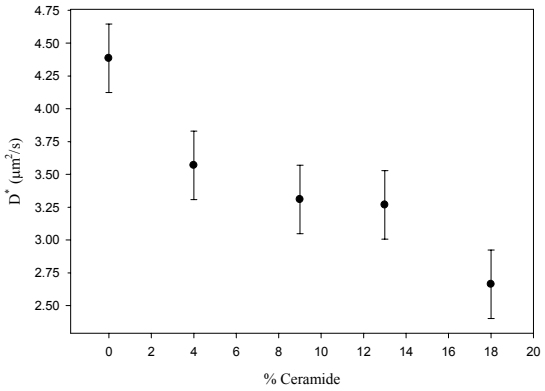

Figure 6.6 *Relative diffusion coefficient D* for the DOPC-rich phase as function of the ceramide content. D* is computed assuming a mean value w_0 = 0.29 μm for all of the samples. To convey a general estimate of the uncertainty associated with these measurements, the error bars represent the average of the standard deviations of all the experimental points.*

The diffusion times τ_D of RhoPE in the DOPC-rich phase were determined by fitting the FCS curves to a one-component two-dimensional Brownian diffusion model. The results are shown in figure 6.6, where the relative diffusion coefficients $D^*=w_0^2/4\tau_D$ are plotted as a function of the ceramide content. An absolute estimate of the diffusion coefficient would require precise measurements of the focal spot radius w_0, but that is not needed in this case, as we are only interested in the relative changes of the diffusion coefficient as a function of Cer content in the membrane. D* is thus computed by using a reasonable estimate of w_0 (see Materials and Methods), which is therefore considered a simple scaling factor.

We observed a well-defined dependence of the lipid diffusion coefficient in the bilayer as a function of the ceramide content. In particular, the presence of the Cer molecule, up to 18%, slows down the diffusion of RhoPE in the L_d phase. The estimated diffusion coefficients for this phase were consistent with those previously measured in analogous samples (26).

The membrane viscosity of L_o domains was probed by using the AFM tip. Figure 6.7 shows the time-course of such a measurement, in which the domains were deformed by scanning the tip at high force and speed.

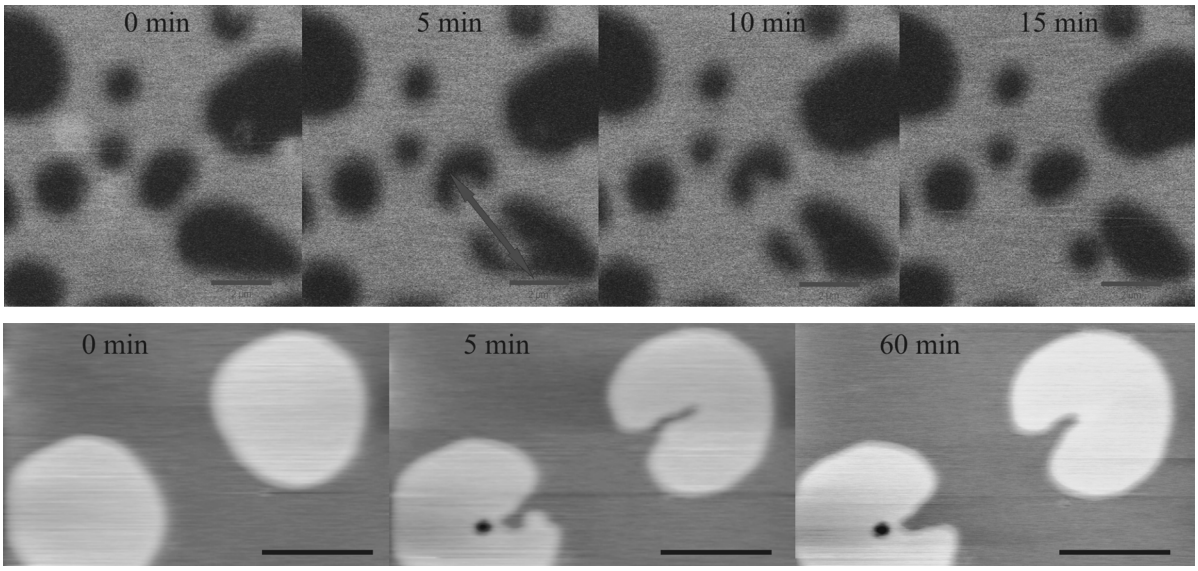

Figure 6.7 *Time-course of a micromanipulation experiment, in which ordered domains are deformed by the AFM tip. The upper series of panels shows the deformation and relaxation of two domains at intermediate height in a DOPC/cholesterol/SM 1:0.7:1 sample (0% Cer), followed using fluorescence imaging. The circular shape of the domains is fully recovered in a few minutes. The lower series of panels shows AFM images of the same procedure on the highest domains, in a DOPC/cholesterol/SM/Cer 1:1:0.52:0.48 sample (16% Cer). In this case, after ~1h after the deformation, the contour of the domains was still irregular. Measurements were performed at room temperature. Scale bars = 2 μm.*

The upper series of panels in figure 6.7 shows the micromanipulation experiment on two domains at intermediate height (~0.8 nm), for a sample without ceramide. In this case, the time-scales involved in the process of deformation and relaxation of the domains were not long enough to be efficiently monitored by AFM imaging. Fluorescence images show how, after the manipulation process (3rd panel, first row), only a few minutes were needed for the irregular-shaped domains to assume a regular and round shape again. A comparable time-scale for the same process was observed in samples with a ceramide content of 4 mol%. The second row shows the same experiment on the highest microscopic lipid domains (~1.1 nm height), for a 18 mol% Cer sample. In this case, the whole process was slower than in the previous case and could, therefore, be effectively monitored by AFM imaging. One hour after the manipulation, the domains still featured the irregular contours which were initially caused by the AFM tip. Compared to the domains of intermediate height, this lipid phase thus exhibited at least 10-fold slower dynamics.

6.3.3 Effects of Sphingomyelinase on L_o/L_d phase separation

In living organisms, ceramide can be produced from sphingomyelin in a reaction catalyzed by the enzyme sphingomyelinase (SMase). The action of this protein was observed here in vitro, on a SLB composed of SM/DOPC/cholesterol 1:1:0.7. A small tube was positioned between the mica and the glass block, which holds the AFM cantilevers, and 60 mU of the enzyme were introduced into the solution after starting the imaging scan.

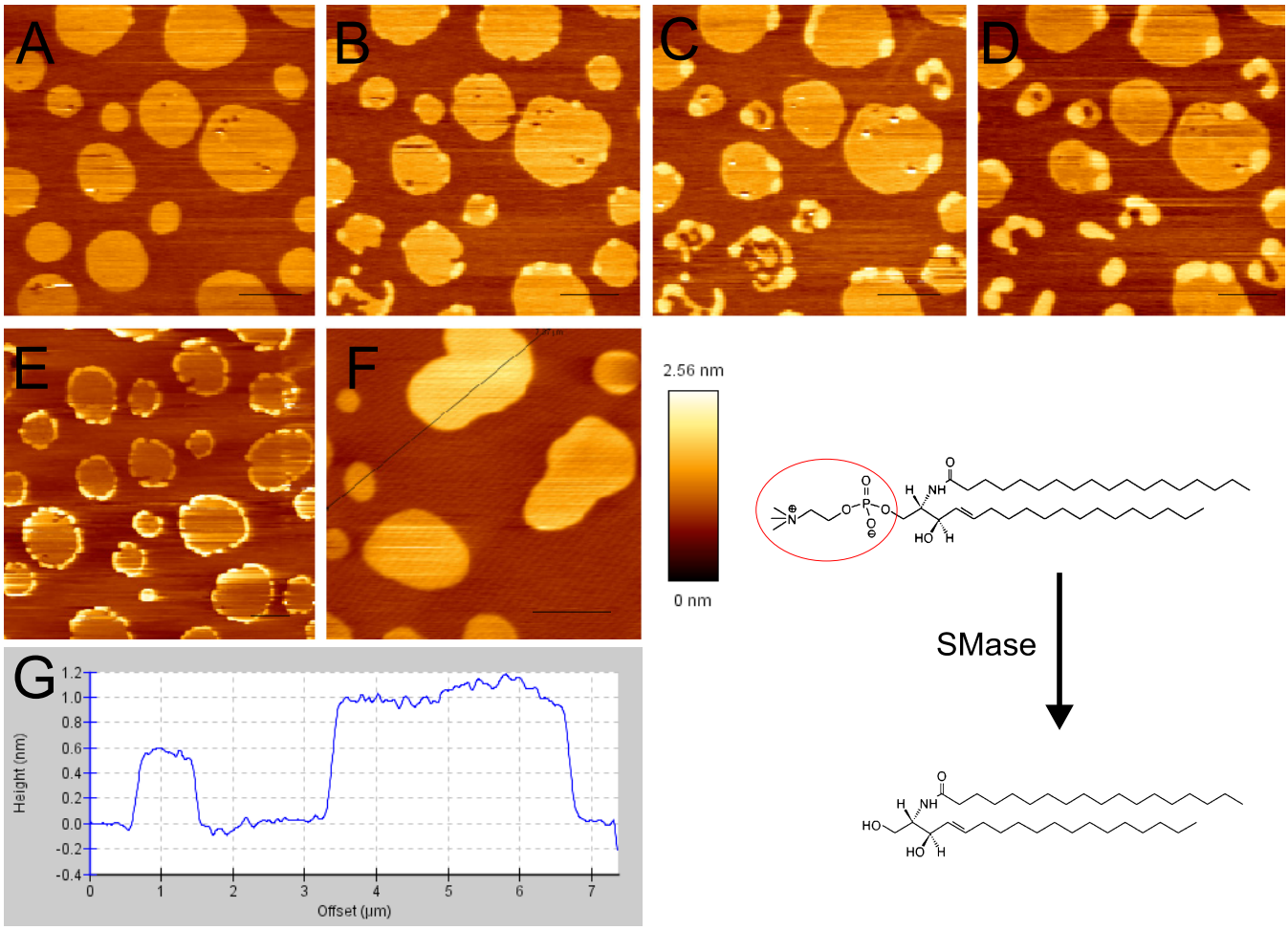

Figure 6.8 *Panels A-B-C-D and E-F show a time-course measurement on two DOPC/cholesterol/SM/:1:0.7:1 samples, after addition of SMase at room temperature. The enzyme was injected at the beginning of the scans represented in panels A, for the first experiment, and E for the second. Imaging time was set to 4 minutes. Panel F and G, in particular, show typical topographical features of the membrane that could be observed after the action of SMase. In the right lower corner, the structures of SM C18:0 and ceramide C18:0 are shown. The red circle indicates the SM phosphocholine group, which is removed by the action of SMase. Scale bars = 2 µm.*

Figure 6.8 shows time-course AFM imaging performed on two analogous samples (sample 1: panels A B C D, sample 2: E F), obtained with an imaging speed of 4 minutes. Due to the action of the SMase, the lipid domains experienced changes in both height and shape. In particular, the enzyme acted on the liquid-ordered domains, starting from their borders and eventually destabilizing them, thereby inducing changes in their shape and formation of smaller domains or even creating holes in the bilayer. The differences between the two observed samples are due to the difficulties in controlling both the local concentration of the enzyme and the reaction speed. In both cases, several minutes after addition of the enzyme, domains with different heights are present in the SLB and their topology was comparable to that observed in the other previously examined samples with higher ceramide content (see figures 6.1 and 6.3).

An analogue experiment was performed using giant unilamellar vesicles (GUVs) with the same lipid composition. Figure 6.9 shows a fluorescence LSM image of such model membranes before the application of SMase. While DiD (red channel) is a good marker for the L_d phase, the BODIPY-FChol partitions more evenly between the two lipid phases.

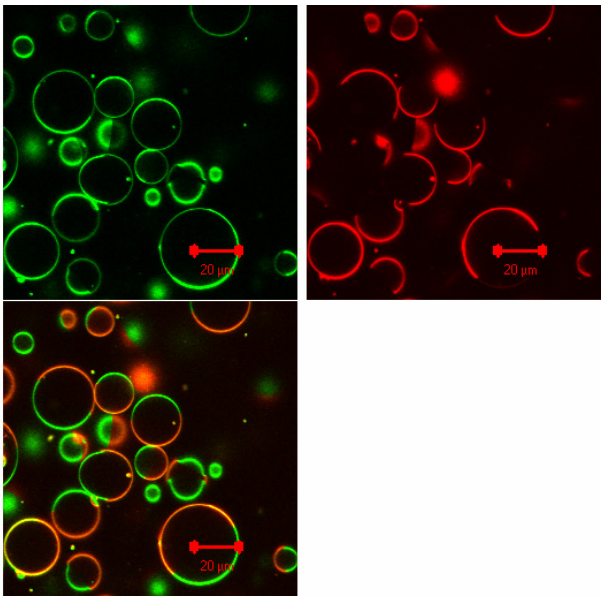

Figure 6.9 *GUVs were prepared using a mixture of DOPC, SM and cholesterol. DiD-C18 (red) and BODIPY-FChol (green) were used to mark the two lipid phases.*

We exogenously added SMase to these GUVs to analyze whether intra-vesicular membranes were formed from one of these lipid phases. Shortly after the addition of the SMase, small vesicles started to bud from the L_o lipid phase and to accumulate in the lumen of the GUVs (Figure 6.10). The intravesicular membrane was predominantly labelled by BODIPY-FChol and contained only small amounts of DiD. The left panel in Figure 6.10 shows a magnification of the membrane of a GUV from where BODIPY-FChol labeled vesicles are about to bud in. Similar results were observed when G_{M1} was included in the GUVs and fluorescently-labeled cholera-toxin was used to mark the L_o lipid phase (data not shown).

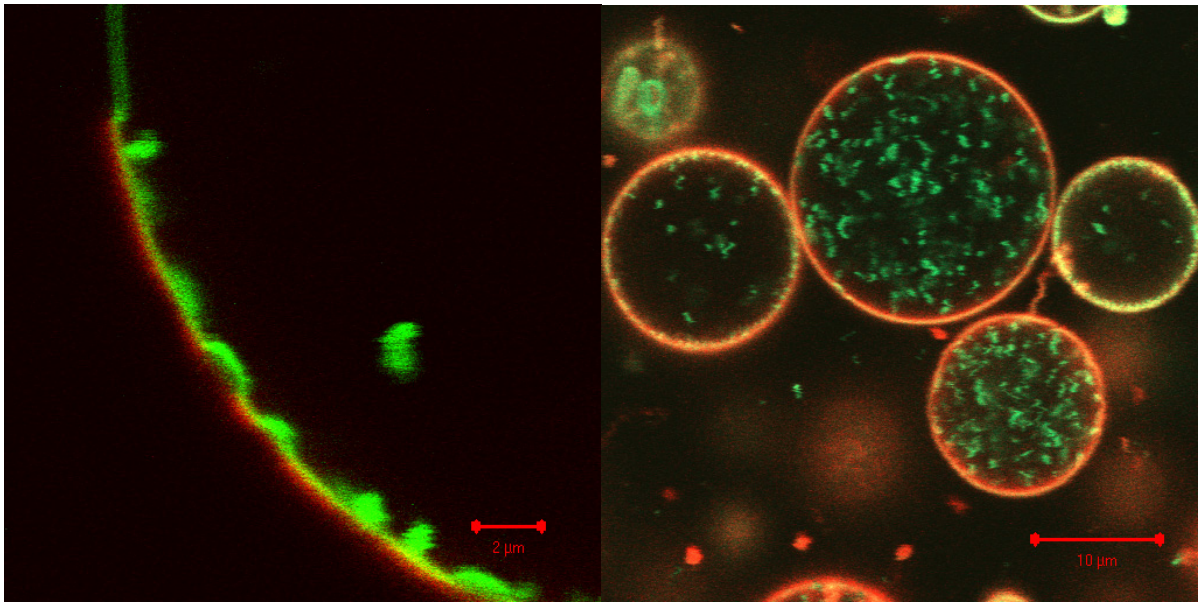

Figure 6.10 *GUVs were incubated with SMase. After few minutes, budding in of the membrane could already be observed (left panel). Eventually, many GUVs were filled with floating fluorescent particles (right panel: green channel, red channel and overlay). The*

intravesicular membrane was predominantly labelled by BODIPY-FChol and contained only small amounts of DiD.

6.4 Discussion

We have investigated both the morphology and the dynamical properties of lipid microdomains in supported bilayers, composed of DOPC, SM, cholesterol and ceramide, by using a combined approach of AFM and FCS. Ternary mixtures of DOPC, SM and cholesterol 1:1:0.7 (molar ratio) are known to exhibit liquid-liquid immiscibility, leading to phase-separated microdomains in model membranes (4). For our measurements, we started from this lipid composition, gradually substituting SM with ceramide. The molar concentration of ceramide in our samples was between 0% and 18%. The resulting domain morphology of samples with more than 4% ceramide was found to be qualitatively consistent with that obtained by the action of SMase, which converts SM into ceramide, on bilayers composed of SM, DOPC and cholesterol 1:1:0.7 molar. Most interestingly, all the significant rearrangements of the bilayer occurred at a Cer concentration between 9 and 18%, which is comparable to the physiological concentrations (11). Our results showed that the addition of ceramide is correlated to the presence of a third lipid phase. AFM images of bilayers with more than 4% ceramide exhibited indeed three different topographical levels. An increase of ceramide concentration results in rather continuous and gradual morphological changes of the domains (see figure 6.1 and 6.3). For this reason, it is quite safe to assume that, in all our measurements, only three well defined lipid phases were present.

For all the lipid mixtures used here, the lowest topographical level can be assigned to a L_d, DOPC-enriched phase, according to the initial lipid composition and the measured diffusion coefficients shown in figure 6.6, which are comparable to that of a liquid crystalline lipid environment. It is worth noting that the diffusion of lipids in such a phase is ~20% slower for a supported bilayer, if compared to free-standing membranes in water (26). Such difference could be ascribed to the effect of the mica support and/or to the presence of salt in our samples.

The lipid phase at intermediate topographical level is ~0.8 nm higher than the surrounding lipid matrix and is organized in microscopic round domains, which appear dark in fluorescence. They can be observed in samples containing 0-13% Cer, and can be assumed to consist of a L_o phase, enriched in cholesterol and SM. This statement is substantiated both by the height difference with the DOPC matrix, consistent with previous AFM data (21, 23), and by the liquid-like properties, which were probed by the micromanipulation experiment (see figure 6.7). Fluorescence imaging shows that these liquid-ordered domains rapidly assumed a regular round shape to minimize the interaction surface between different phases.

Interestingly, distinct properties were observed for the highest topographical level. The height step between these lipid microdomains and the low DOPC-enriched phase is around 1.2 nm, which is comparable to what is observed for liquid-gel phase separation in POPC/DPPC (27) and DOPC/DPPC (28). Furthermore, the surface fraction occupied by the highest phase grows in parallel with ceramide content. Taken together, the data lead to the conclusion that the highest domains observed in our samples most likely correspond to a ceramide-enriched gel phase. This finding is supported by the fact that, after the AFM tip-induced deformation, the relaxation time back to a round shape was on the time-scale of hours, i.e. much longer than the one observed for the liquid-ordered domains.

Although our data do not allow for a precise characterization of the composition of distinct lipid phases, some considerations can be formulated. It is well known that ceramide molecules interact strongly, forming a stable hydrogen-bond network among their polar

heads. As a consequence, poor mixing with other lipids and formation of ceramide-enriched gel-like domains is then expected for our sample compositions (8, 29). Additionally, both ceramide and cholesterol are known to reduce the steric repulsion among the bulky SM headgroups and to interact via hydrogen-bonds with their polar moieties (29). In this case, SM molecules can come closer together, maximizing the interactions between their aliphatic chains. This molecular mechanism explains the stabilizing effect of cholesterol in SM-enriched L_o domains. In previous x-ray diffraction studies on C18:0-SM bilayers, it was found that the thickness of the membrane, which is an indication of the vertical extension of the lipid aliphatic chains and of their packing density, is reduced from 5.2 to 4.7 nm by the presence of cholesterol (30). Conversely, cholesterol makes the lower DOPC-rich phase thicker and thus reduces the height step between this phase and the SM-rich domains (21). Previous AFM measurements show that, in case of liquid-gel phase separation in PC/Cer (27) and PC/SM (31) bilayers, the relative height of the gel domains was between 0.8 and 1 nm. According to the previous considerations, these values must represent an upper limit, if cholesterol is introduced in the lipid mixture. Consequently, we speculate that the height step of ~1.2 nm that we observed for the highest domains is an indication of the existence of a highly ordered and tightly packed gel-like phase, most likely composed of both ceramide and SM molecules. This possibility is supported also by the data in figure 6.3, which show a gradual decrease of the surface occupied by the ordered domains (liquid-ordered and gel). As ceramide increases the stability and the configurational order in the ordered domains, the distance between the lipids and, consequently, the surface occupied by the ordered phase may decrease. On the other side, such decrease of the surface fraction could also be partially due to the lower quantities of SM present in the bilayer. As SM is supposed to be present both in gel and liquid ordered domains, interacting respectively with ceramide and cholesterol, the surface occupied by these domains should indeed scale down with the decreasing quantity of SM included in the lipid mixture. Small or no condensing effect of cholesterol in the DOPC-rich phase can be observed in our samples, in agreement with previous experiments (32). Our hypothesis according to which these ceramide-rich domains are constituted by SM and Cer was eventually validated by recent experiments (32b).

As a direct consequence of the strong interactions with SM, it was also proposed that ceramide molecules could efficiently displace cholesterol from raft domains in model membranes (18). A possible explanation for this phenomenon is that less SM molecules are available for interacting with cholesterol in the ordered domains. On one hand, ceramide gradually replaces SM in the preparation of the bilayer, so that less and less SM is engaged in an interaction with cholesterol. On the other hand, ceramide competes with cholesterol in the interaction with the remaining fraction of SM. The presence of cholesterol in the DOPC-rich phase would have two immediate consequences. First, a decrease of the diffusion coefficient in that phase, probably due to the ordering imposed by the rigid sterol rings on DOPC aliphatic chains (26, 33, 34). Furthermore, a transfer of cholesterol to the L_d phase would cause, as already pointed out, a decrease of the height difference between the liquid-ordered and the liquid-disordered phase. As evident from figure 6.6, the sample containing 18% ceramide showed indeed a reduction of the RhoPE diffusion coefficient by 40% in the DOPC-rich phase, compared to bilayers prepared without ceramide. Similar reduction of diffusion coefficient was measured in DOPC/Cholesterol giant unilamellar vesicles, when cholesterol content was increased from 0% to ~40% molar (26). Figure 6.3 shows that the height difference between the liquid-ordered and the lowest phase is reduced from ~0.8 nm to ~0.6nm, already at 9% ceramide. This data, although not conclusive, strongly support the hypothesis of an increased presence of cholesterol in the DOPC-rich phase, as a consequence of ceramide-induced displacement from rafts.

Finally we studied the effect of the enzyme SMase on a lipid bilayer composed of SM/DOPC/Cholesterol 1:1:0.7. Figure 6.8 E shows that the enzyme localizes on the L_o phase

and that the production of ceramide starts at the border of domains. The inhomogeneous distribution of the enzyme activity can be rationalized by the molecular packing disorder characterizing the interface between two lipid phases. In these areas of the membrane, the insertion of external molecules like proteins or drugs is energetically more favorable (35). Thus, in the case of SMase acting on SM/DOPC/Cholesterol bilayers, the substrate (i.e. the choline moiety) near the boundary of L_o domains might be more favorably exposed to the active site of the enzyme. The membrane structural features observed after enzyme addition are comparable to what is observed when ceramide is directly included in the preparation of the bilayer. In particular, beside the formation of holes induced by ceramide formation, three topographical levels can be distinguished in the sample (figure 6.8 G-H), being quantitatively comparable to those observed at 8% or 12% ceramide. It is worth noting that, if the enzyme action is stopped by strong dilution, structural rearrangements of the bilayer, monitored by fluorescence imaging and FCS in the disordered phase, keep taking place for at least 100-120 minutes (data not shown), in line with previous observations by Holopainen et al. (29).

6.5 Conclusions

In the work described in this chapter, a combination of AFM and FCS has been for the first time used to study model membranes of biological relevance. In particular, we were able to investigate simultaneously the fine structural features and the dynamic properties of supported lipid bilayers, which exhibit L_o, raft-like, domains. We showed that the presence of physiological quantities of ceramide severely affected the lipid spatial organization in domains, as a gel-like ceramide-enriched phase appeared in correspondence with raft-like domains. Furthermore, our data provide evidence of an increased concentration of cholesterol in the L_d phase, which support the hypothesis of cholesterol displacement from rafts induced by ceramide (18). Finally, the presence of ceramide and the local membrane curvature alterations that we observed in the GUVs experiments were shown to be connected with protein sorting in cellular cargo dynamics and exosomes production (36,37). Similar structural alterations of membrane microdomains may have crucial importance in regulating signal transduction or lipid-mediated cell signalling *in vivo (8)*.

6.6 References

1. Singer, S. J., and G. L. Nicolson. 1972. Fluid mosaic model of structure of cell-membranes. Science. 175:720-731.

2. Barenholz, Y., and T. E. Thompson. 1980. Sphingomyelins in bilayers and biological-membranes. Biochim. Biophys. Acta. 604:129-158.

3. Anderson, R. G. W. 1998. The caveolae membrane system. Annu. Rev. Biochem. 67:199-225.

4. Mayor, S., and M. Rao. 2004. Rafts: Scale-dependent, active lipid organization at the cell surface. Traffic. 5:231-240.

5. Simons, K., and E. Ikonen. 1997. Functional rafts in cell membranes. Nature. 387:569-572.

6. Simons, K., and W. L. C. Vaz. 2004. Model systems, lipid rafts, and cell membranes. Annu. Rev. Biophys. Biomol. Struct. 33:269-295.

7. Kolesnick, R. N., F. M. Goni, and A. Alonso. 2000. Compartmentalization of ceramide signaling: Physical foundations and biological effects. J. Cell. Physiol. 184:285-300.

8. Cremesti, A. E., F. M. Goni, and R. Kolesnick. 2002. Role of sphingomyelinase and ceramide in modulating rafts: do biophysical properties determine biologic outcome? FEBS Lett. 531:47-53.

9. Bollinger, C. R., V. Teichgraeber, and E. Gulbins. 2005. Ceramide-enriched membrane domains. Biochim. Biophys. Acta. In press.

10. Kolesnick, R., and Y. A. Hannun. 1999. Ceramide and apoptosis. Trends Biochem. Sci. 24:224-225.

11. Hannun, Y. A. Functions of ceramide in coordinating cellular responses to stress. 1996. Science. 274:1855-1859.

12. Veiga, M. P., J. L. R. Arrondo, F. M. Goni, and A. Alonso. Ceramides in phospholipid membranes: Effects on bilayer stability and transition to nonlamellar phases. Biophys. J. 76: 342-350.

13. Ruiz-Arguello, M. B., F. M. Goni, and A. Alonso. 1998. Vesicle membrane fusion induced by the concerted activities of sphingomyelinase and phospholipase C. J. Biol. Chem. 273:22977-22982.

14. Siskind, L. J., and M. Colombini. 2000. The lipids C-2- and C-16-ceramide form large stable channels - Implications for apoptosis. J. Biol. Chem. 275:38640-38644.

15. Holopainen, J. M., M. I. Angelova, and P. K. J. Kinnunen. 2000. Vectorial budding of vesicles by asymmetrical enzymatic formation of ceramide in giant liposomes. Biophys. J. 78: 830-838.

16. Al-Makdissy, N., M. Younsi, S. Pierre, O. Ziegler, and M. Donner. 2003. Sphingomyelin/cholesterol ratio: an important determinant of glucose transport mediated by GLUT-1 in 3T3-L1 preadipocytes. Cell. Signal. 15:1019-1030.

17. Ito, J., Y. Nagayasu, and S. Yokoyama. 2000. Cholesterol-sphingomyelin interaction in membrane and apolipoprotein-mediated cellular cholesterol efflux J. Lipid Res. 41: 894-904.

18. Megha and E. London. 2004. Ceramide selectively displaces cholesterol from ordered lipid domains (rafts) - Implications for lipid raft structure and function. J. Biol. Chem. 279: 9997-10004.

19. Alanko, S. M. K., K. K. Halling, S. Maunula, J. P. Slotte, and B. Ramstedt. 2005. Displacement of sterols from sterol/sphingomyelin domains in fluid bilayer membranes by competing molecules. Biochim. Biophys. Acta. 1715: 111-121.

20. Bjorkqvist, Y. J. E., T. K. M. Nyholm, J. P. Slotte, and B. Ramstedt. 2005. Domain formation ans stability in complex lipid bilayers as reported by cholestatrienol. Biophys. J. 88: 4054-4063.

21. Saslowsky, D. E., J. Lawrence, X. Y. Ren, D. A. Brown, R. M. Henderson, and J. M. Edwardson. 2002. Placental alkaline phosphatase is efficiently targeted to rafts in supported lipid bilayers. J. Biol. Chem. 277: 26966-26970.

22. Schwille, P., J. Korlach, and W. W. Webb. 1999. Fluorescence correlation spectroscopy with single-molecule sensitivity on cell and model membranes. Cytometry. 36:176-182.

23. Chiantia, S., N. Kahya, and P. Schwille. 2005. Dehydration damage of domain-exhibiting supported bilayers: an AFM study on the protective effects of disaccharides and other stabilizing substances. Langmuir. 21:6317-6323.

24. Magde, D., E. Elson, and W. W. Webb. 1972. Thermodynamic fluctuations in a reacting system. Measurement by fluorescence correlation spectroscopy. Phys. Rev. Lett. 29:705–708.

25. Benda, A., M. Benes, V. Marecek, A. Lhotsky, W. T. Hermens and M. Hof. 2003. How to determine diffusion coefficients in planar phospholipid systems by confocal fluorescence correlation spectroscopy. Langmuir. 19:4120-4126.

25b. Angelova, M.I., and D. S. Dimitrov. 1986. Liposome electroformation. Faraday Discussions 81: 303.

25c. Li, Z., Mintzer, E., Bittman, R., 2006. First synthesis of free cholesterol-BODIPY conjugates. J. Org. Chem. 71, 1718–1721

26. Kahya N., D. Scherfeld, K. Bacia, B. Poolman, and P. Schwille. 2003. Probing lipid mobility of raft-exhibiting model membranes by fluorescence correlation spectroscopy. J. Biol. Chem. 278:28109-28115.

27. Simonsen, A. C., and L. A. Bagatolli. 2004. Structure of spin-coated lipid films and domain formation in supported membranes formed by hydration. Langmuir. 20:9720-9728.

28. Burns, A. R. 2003. Domain structure in model membrane bilayers investigated by simultaneous atomic force microscopy and fluorescence imaging. Langmuir. 19:8358-8363.

29. Holopainen, J. M., M. Subramanian, and P. K. J. Kinnunen. 1998. Sphingomyelinase induces lipid microdomain formation in a fluid phosphatidylcholine/sphingomyelin membrane. Biochemistry. 37:17562-17570.

30. Maulik, P. R., and G. G. Shipley. 1996. Interactions of N-stearoyl sphingomyelin with cholesterol and dipalmitoylphosphatidylcholine in bilayer membranes. Biophys. J. 70:2256-2265.

31. Milhiet, P. E., M. C. Giocondi, O. Baghdadi, F. Ronzon, B. Roux, and C. Le Grimellec. 2002. Spontaneous insertion and partitioning of alkaline phosphatase into model lipid rafts. EMBO Rep. 3:485-490.

32. Filippov, A., G. Oradd, and G. Lindblom. 2003. The effect of cholesterol on the lateral diffusion of phospholipids in oriented bilayers. Biophys. J. 84:3079-3086.

32b. Silva, L. C.; de Almeida, R. F.; Castro, B. M.; Fedorov, A.; Prieto, M. Biophys.J. 2007, 92, 502-516.

33. Smaby, J. M., H. L. Brockman, and R. E. Brown. 1994. Cholesterol's interfacial interactions with sphingomyelins and phosphatidylcholines: hydrocarbon chain structure determines the magnitude of condensation. Biochemistry. 33:9135-9142.

34. Polson, J.M., I. Vattulainen, H. Zhu, and M. J. Zuckermann. 2001. Simulation study of lateral diffusion in lipid-sterol bilayer mixtures. Eur. Phys. J. E. 5:485-497.

35. Mouritsen, O. G., and K. Jorgensen. 1998. A new look at lipid-membrane structure in relation to drug research. Pharm. Res. 15:1507-1519.

36. Trajkovic K., Hsu C., Chiantia S., Rajendran L., Wenzel D., Schwille P., Brügger B., Simons M. 2007. A role for ceramide in exosome formation within multivesicular endosomes, Science, submitted

37. Chiantia S.**,** Ries J., Chwastek G., Carrer D., Li Z., Bittman R., Schwille P. 2007. Role of ceramide in membrane protein organization investigated by simultaneous AFM and FCS, Biochim. et Biophy. Acta., submitted

Chapter 7 – Role of ceramide chain length in lipid phase separation

7.1 Introduction

Raft microdomains are thought to be involved in various biological processes such as protein and lipid sorting for cell-cell communication or intracellular signaling cascades (1-4).

As it was already introduced in chapter 6, the specific composition of microdomains, and the lateral organization of the membrane in general, can be dramatically altered during several biological processes, like apoptosis, immune response, senescence, and viral or bacterial pathogenesis. In all the described situations, it was shown that the concentration of the sphingolipid ceramide (Cer) can rise from very low values up to 10-20% of the total lipid content (5-7). It was also proposed that, as a consequence of Cer generation, rafts would coalesce in large platforms where different receptors and proteins are clustered, thus initiating signal transduction (8). Due to its strong regulation of cell death, growth, and differentiation, Cer has been also identified as a possible therapeutic agent in cancer (9,10).

From a structural point of view, Cer is formed by a sphingosine base linked via its amino group to a fatty acyl chain, containing from 2 to 28 carbon atoms. The long-chain Cer (C16 to C24 N-acyl chain Cer) are most abundant in nature and are classified as "insoluble nonswelling amphiphiles" (11,12). The high melting temperature and peculiar molecular shape contribute to their ability to strongly influence the bilayer, imposing a negative curvature on the membrane, impairing its impermeability and leading to the formation of highly ordered Cer-enriched microdomains (see chapter 6 and Ref. 5,6,13-15). Conversely, the short-chain Cer (i.e., C10 to C2) are classified as "soluble swelling amphiphiles" and are less common in natural membranes (16,17). These lipids have often been used in biological experimentation with living cells as substitute for long-chain Cer (e.g., to induce apoptosis), since they can be easily dissolved in water and show a high rate of spontaneous inter-/intra-bilayer movement (11,12,17,18). Nevertheless, it was occasionally observed that the physiological effects of Cer may depend on the chain length (5,19,20) and indeed, long- and short-chain Cer exhibit very different biophysical properties. Short-chain Cer do not segregate from liquid-crystalline phospholipids, they promote a positive curvature in lipid membranes, and their ability to increase bilayer permeability is very low (16,21-24). Furthermore, differently from long-chain Cer, short-chain Cer cannot form detergent resistant fractions when mixed with SM (25), destabilize the cholesterol/SM L_o domains, and perturb in general the structural order in model and cellular membranes (18,26,27). In the previous chapter of this thesis, we have shown that C18 Cer form separate domains in lipid mixtures that exhibit L_o-L_d "raftlike" phase separation (13). It is therefore interesting to investigate how short-chain Cer behave in raft-exhibiting membranes. Do they segregate into separate domains? How is the local viscosity influenced by the presence of Cer?

In this chapter, we systematically investigated the effects of Cer chain length in a lipid bilayer, which contains L_o domains, as a model for the putative phase separation in biological membranes. To this end, we used a combined approach of atomic force microscopy (AFM) and fluorescence correlation spectroscopy (FCS) (28,29). Our results show that only C18 and C16 Cer are able to segregate from the L_o phase, thus forming gel-like Cer-enriched domains. Conversely, short-chain Cer can mix with lipids in the L_o phase. Furthermore, whereas long-chain Cer do not influence the physical properties of the L_o phase, their short-chain analogues like C12, C6, and C2 are shown to perturb the lipid-lipid interaction in the raft domains and, thereby, remarkably decrease their surface extent and viscosity.

7.2 Materials and methods

7.2.1 Chemicals

1,2-Dioleoyl-*sn*-glycero-3-phosphocholine (dioleoylphosphatidylcholine; DOPC), *N*-stearoyl-D-*erythro*-sphingosylphosphorylcholine (stearoyl sphingomyelin; SM), *N*-stearoyl-D-*erythro*-sphingosine (C18:0 ceramide, C18 Cer), *N*-palmitoyl-D-*erythro*-sphingosine (C16:0 ceramide, C16 Cer), *N*-lauroyl-D-*erythro*-sphingosine (C12:0 ceramide, C12 Cer), *N*-hexanoyl-D-*erythro*-sphingosine (C6:0 ceramide, C6 Cer), *N*-acetoyl-D-*erythro*-sphingosine (C2:0 ceramide, C2 Cer), and cholesterol were purchased from Avanti Polar Lipids (Alabaster, AL) and used without further purification. Cholesteryl 4,4-difluoro-5,7-dimethyl-4-bora-3a,4a-diaza-*s*-indacene-3-dodecanoate (cholesteryl BODIPY FL C_{12}, BODIPY-CholE) was from Invitrogen (Eugene, OR). Optical Adhesive 88, used to glue the mica on coverslips, was purchased from Norland Products Inc. (Cranbury, NJ). Buffers are described in section 4.2.1.

7.2.2 Supported lipid bilayers (SLBs)

See section 4.2.2 of this thesis.

7.2.3 AFM, confocal fluorescence microscopy and FCS

See section 6.2.3 of this thesis. Differently from the work described in chapter 6, the FCS results shown here are those obtained the z-scan method (30-31).

7.3 Results

7.3.1 Membrane structure: only long-chain Cer segregate as own gel phase

Supported lipid bilayers were prepared using a DOPC/SM/Cer/cholesterol 1/0.7/0.3/0.67 molar mixture, containing Cer with different chain lengths. In particular, Figure 7.1 shows typical results obtained for membranes containing C18, C16, C12, C6, and C2 Cer. For comparison, a sample without Cer (DOPC/SM/cholesterol 1/1/0.67) is shown in the first panel.

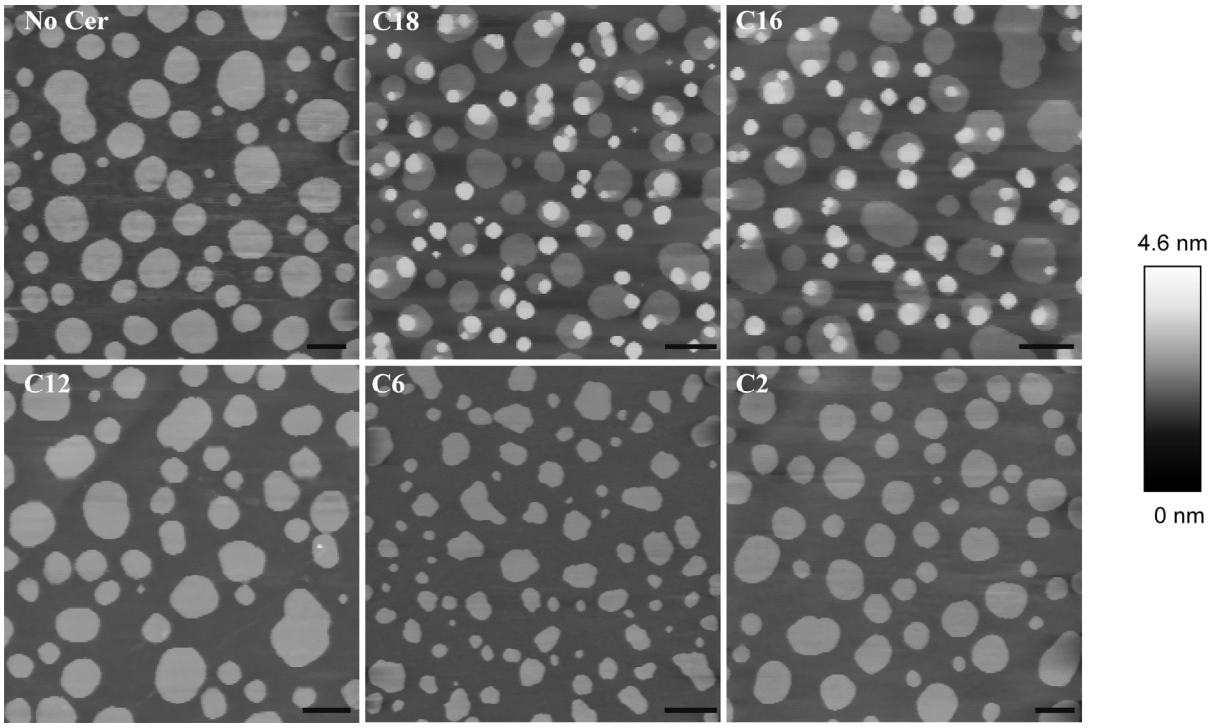

Figure 7.1 *AFM topographical images of SLBs containing Cer with different chain lengths, at room temperature. The lipid composition was DOPC/SM/Cer/cholesterol 1/0.7/0.3/0.67 molar ratios. The "No Cer" panel shows a DOPC/SM/cholesterol 1/1/0.67 sample as a reference. All the other panels refer to the different Cer chain lengths used to prepare the bilayers. In the C18 and C16 SLBs, three different topographical levels can be distinguished. Their relative heights are 0, ~0.6, and ~1.3 nm. In all the remaining images, only two height levels can be identified. Every image is representative of at least two independent sample preparations. Each SLB was first imaged with confocal fluorescence microscopy (~400 x 400 μm), to check its homogeneity, and eventually with AFM (at least three images for a total of ~650 μm^2). Scale bar = 2 μm.*

For a DOPC/SM/cholesterol lipid mixture with the above-mentioned molar ratio, coexistence of two different phases is expected in a broad range of temperatures (28,32-34). The light-colored domains, ~0.8 nm higher than the surrounding membrane, are assigned to a L_o phase enriched in SM and cholesterol. Conversely, the darker areas correspond to a L_d phase enriched in DOPC. If 30% of the SM is substituted by C18 Cer, a more complex lipid lateral organization is expected (13). As shown in Figure 7.1 in the panel labeled "C18", three different height levels were observed. The first two corresponded again to the L_d and L_o phases, in analogy with the "No Cer" sample. Note that, in line with previous results,[13] the height difference between these two phases was ~25% smaller than that measured in the absence of Cer. The third height level, ~0.6 nm higher than the L_o phase, corresponded to a gel-like Cer-enriched phase (13), as already described in section 6.3.2. Figure 7.2 shows the exact height differences between the different types of domains and the lowest topographical level, as a function of Cer chain length.

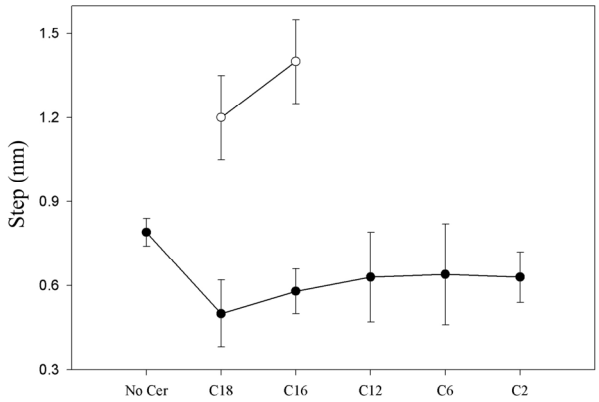

Figure 7.2 *Height differences between different lipid phases as a function of Cer chain length. The open circles show the height difference between the highest lipid phase and the surrounding lipid matrix, while the closed circles show the height difference between the domains of intermediate height and the surrounding lipid matrix. The height values were computed from a statistical analysis of at least ~650 μm^2 of two different SLBs. The error bars represent the standard deviation of the measurements.*

Samples with C16 Cer, as shown in Figure 7.1 in the panel labeled "C16", exhibited a topography that was very similar to that of Cer 18, with comparable height differences between the different phases.

AFM images of samples containing short-chain Cer (C12, C6, and C2) are shown in the lower panels of Figure 7.1. For these samples, again, only two topographic levels were observed. The light-colored domains are 0.5-0.7 nm higher than the lower (darker) phase, as shown in Figure 7.2. Although these data are, in general, consistent with L_d-L_o phase separation, no certain conclusion about the physical characteristics of these domains can be drawn from the AFM structural/topographical information.

7.3.2 Short-chain Cer inhibit the formation of L_o phase

The high reproducibility and homogeneity of SLBs, allowed the quantitative study of the effect of Cer chain length on the surface area occupied by each lipid phase. Figure 7.3 shows the surface percentage occupied by each phase in the different samples. Data from a "No Cer" sample (DOPC/SM/cholesterol 1/1/0.67) are also reported as a reference.

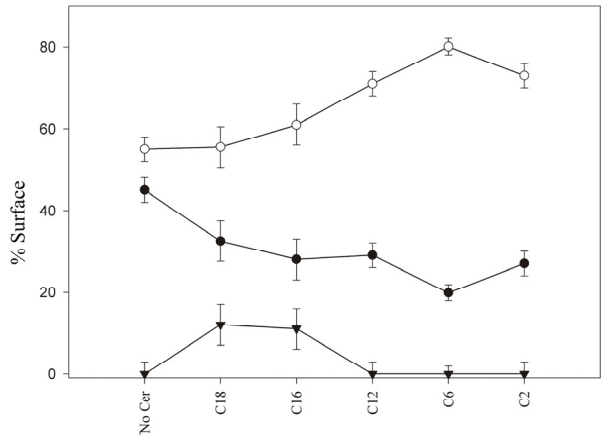

Figure 7.3 *Relative surface fractions of Cer-containing bilayers at room temperature. The surface extents of the L_d phase (open circles), L_o phase (close circles), and gel phase (triangles) are plotted as a function of Cer chain length, at room temperature. The "No Cer" sample refers to a DOPC/SM/cholesterol 1/1/0.67 molar lipid mixture. The surface fraction values were computed from a statistical analysis of at least ~650 μm^2 of two different SLBs. Error bars represent the standard deviation.*

The surface extent of the L_o phase in the examined lipid compositions showed a steady monotonic decrease as a function of decreasing Cer chain length. In particular, when C18 or C16 Cer was added to the lipid mixture, the contraction of the L_o phase could be almost entirely explained by the appearance of the gel phase. For these two samples, in fact, the enlargement of the L_d phase was very limited. However, when short-chain Cer were added to the mixture, no gel phase was observed. In this case, the further decrease of L_o phase extent was accompanied by a significant enlargement of the disordered phase. Interestingly, the above-described trend changes in the presence of C2 Cer.

Finally, the size of L_o domains seems to be affected by the presence of short-chain Cer. In particular, the samples containing C2 Cer showed a reproducible ~25% decrease (from 2.3 to 1.7 μm^2) in average domain size, if compared to samples without Cer. Interestingly, in the case of C6 Cer (see C6 panel, Figure 7.1) this effect was even larger and the average domain size was ~60% smaller than the value measured in samples without Cer.

7.3.3 Membrane dynamics: short-chain Cer exert a 'fluidizing effect' on L_o phase

In order to support and complete the structural information from AFM, FCS measurements were performed on distinct lipid phases of SLBs composed of the above-mentioned lipid mixtures. In this way, we set out to quantitatively investigate the local membrane viscosity by monitoring the Brownian diffusion of the fluorescent lipid BODIPY-CholE inside the bilayer. This commercially available fluorescent sterol was chosen because it has no net electric charge and partitions sufficiently in the ordered phase (36). FCS measurements were performed in the L_o, L_d and, when present, in the gel phase. In each case, a mathematical analysis of the fluctuations of the fluorescence signal from the SLB resulted in characteristic autocorrelation curves. Figure 7.4 shows examples of such curves and, in the inset, the corresponding fluorescence temporal signal is shown.

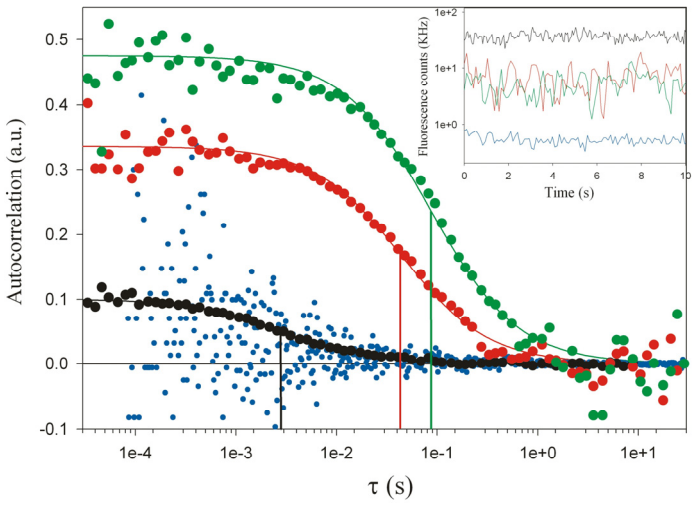

Figure 7.4 *Representative autocorrelation curves measured in different lipid phases of the bilayer, at room temperature. In particular, typical autocorrelation curves are shown for the Ld phase (black), Lo phase in samples without Cer (green), for the Lo phase in samples containing C6 Cer (red), and for the gel phase in a C18 or C16 Cer sample (blue). For each correlation curve, the vertical bars indicate the diffusion time of the BODIPY-CholE in the SLBs. The solid lines represent the fittings of the autocorrelation curves to a one-component, two-dimensional Brownian diffusion model. The inset shows, with the same color code, typical fluorescence intensity tracks from which the autocorrelation curves were calculated.*

In particular, the black and the green data refer respectively to the L_d and the L_o phase in a typical "No Cer" sample. Comparing the decay of the two curves as a function of time, it was evident that the L_o phase was characterized by a 30-fold slower dynamics compared to the L_d phase. Furthermore, comparison of the autocorrelation amplitude, which is inversely proportional to the number of diffusing molecules, revealed that the concentration of BODIPY-CholE in the L_d phase was ~5 times higher than in the L_o phase. The red data in Figure 7.4 show the autocorrelation curve from the diffusion of BODIPY-CholE in the L_o phases of samples containing C6 Cer. The comparison with the data represented in green suggests that the diffusion of lipids was in this case ~3 times faster than that in L_o phase in the absence of short-chain Cer. The lower correlation amplitude indicated an increased number of diffusing fluorophores. The blue data points represent the autocorrelation curve calculated from the fluorescence signal in the gel phase in a C18 or C16 sample. This phase was most likely enriched in Cer and SM and was characterized by a very high viscosity and packing density (13,35). The very low autocorrelation amplitude, almost indistinguishable from the experimental noise, and the very low fluorescence signal reflected the negligible amount of BODIPY-CholE in this phase. By using a fluorescent probe that associates strongly with these Cer-enriched domains, i.e., fluorescent cholera toxin B subunit, strong bleaching was observed (see chapter 8).

Finally, a systematic analysis (31) of several autocorrelation curves obtained at different *z*-positions provided the diffusion times (τ_D), the diffusion coefficient (D^*), and the number of fluorescent particles (NP) in the focal volume. These parameters were collected for all the samples, in both the L_d and the L_o phases, as a function of Cer chain length. Figure 7.5 shows the relative diffusion coefficients ($D^* = w_0^2/4\tau$) in both the L_d (closed circles) and the L_o phase (open circles) for all the examined samples.

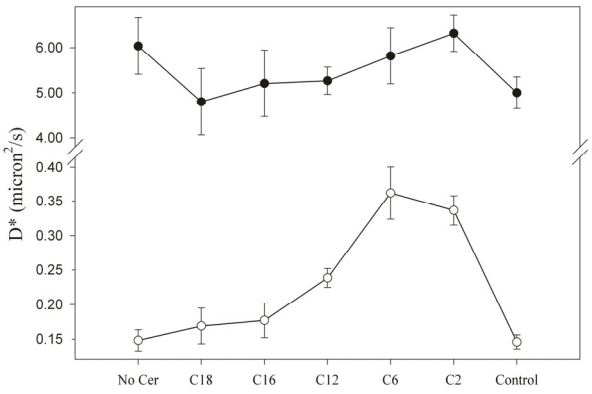

Figure 7.5 *Relative diffusion coefficients D* for the L_d (closed circles) and L_o phase (open circles) as a function of Cer chain-length, measured at room temperature. D* was calculated using the z-scan method and the error bars represent the standard deviations deriving from the fitting procedure. The "No Cer" and "Control" samples refer to a DOPC/SM/cholesterol 1/1/0.67 and a DOPC/SM/cholesterol 1/0.7/0.67 molar ratio mixture, respectively. Each diffusion coefficient was computed as the average of the values measured in at least three different positions of two independent SLB preparations.*

An absolute estimate of the diffusion coefficient would require a precise measurement of the focal spot radius (w_0), but that is not needed in this case. The relative changes of the diffusion coefficient are, in fact, enough to determine the effect of Cer on the physical properties of the bilayer. D^* is thus computed by using a reasonable estimate of w_0 (see Materials and Methods), which can be therefore considered as a simple scaling factor. As evident from Figure 7.5, the addition of either long- or short-chain Cer did not influence

significantly the dynamic properties of the membrane in the disordered phase. The changes of D^*, as a function of Cer chain length, were small compared to their standard deviation. On the other side, much larger variations were observed in the L_o phase. The diffusion of BODIPY-CholE in the L_o phase in both "C18" and "C16" samples is comparable to that observed in "No Cer" samples. Conversely, the SLBs containing short-chain Cer exhibited much faster dynamics, especially for the C6 sample. As observed for the relative surface occupied by the different lipid phases, the above-described trend of the diffusion coefficient in the L_o phase varied slightly in the presence of C2 Cer. The last point in Figure 7.6 shows the FCS results obtained in a control sample composed of DOPC/SM/cholesterol 1/0.7/0.67 molar ratio. Differently from the "No Cer" sample, this lipid composition simulates the case in which any of the examined membranes lost its entire Cer content because of strong Cer partition into water. This might be a possibility in the case of short-chain Cer, like C2 Cer, which are more water-soluble than their long-chain counterparts (11). The control sample thus provides a way to verify that the changes in the bilayer properties are not due to the fact that the short-chain Cer were removed from the bilayer and partitioned into water, thereby changing the ratio among the remaining membrane components. If the control sample exhibited dynamical or structural properties similar to the C6 or C2 Cer sample, this could indicate that the Cer partitioned strongly in the water phase. As shown in Figure 7.5, this was not the case.

Finally, Figure 7.6 shows the partition coefficient $K(L_o/L_d)$ of BODIPY-CholE between the L_o and the L_d phase. The local concentration of the fluorescent probe was determined directly from the FCS measurements, as the number of particles in the focal volume is inversely proportional to the amplitude of the autocorrelation curve. Furthermore, the size of the focal volume and, thus, the final concentration of the diffusing BODIPY-CholE was easily derived by the same *z*-scan method used to measure the diffusion coefficients D^* (31). The amount of fluorescent probe molecules in the L_o phase was approximately the same for the "No Cer", "C18" and "C16" samples. Interestingly, much more BODIPY-CholE molecules partitioned in the raft-like phase in the presence of short-chain Cer. In particular, our data showed at least a 2-fold increase in the value of $K(L_o/L_d)$ of the "C6" sample, if compared to a bilayer without Cer.

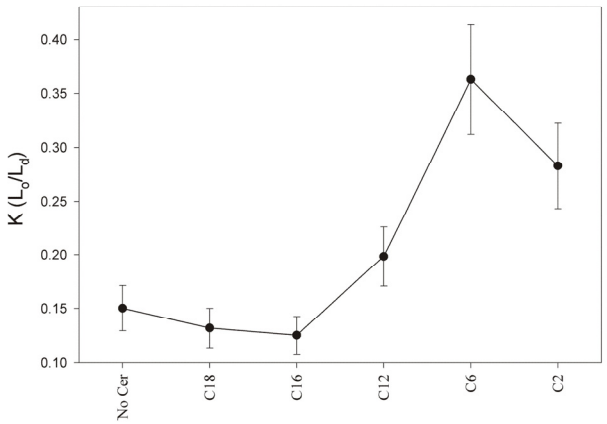

Figure 7.6 *Partition coefficient of BODIPY-CholE between the L_o and the L_d phase at room temperature. The ratio between the number of BODIPY-CholE molecules in the L_o and in the L_d phase, measured by the maximum amplitude of the autocorrelation amplitude, as a function of Cer chain-length. Error bars represent the standard deviations of the measurements. Each partition coefficient was computed as the average of the values measured in at least three different positions of two independent SLB preparations.*

7.4 Discussion

7.4.1 Long-chain Cer – C18 and C16

The domain morphologies in DOPC/SM/cholesterol 1/1/0.67 supported bilayers which contain ~10 mol % long-chain C18 and C16 Cer are practically indistinguishable. AFM imaging clearly shows the presence of three distinct lipid phases. Their height differences are consistent with the L_d/L_o/Cer-enriched phase separation that was described in the previous chapter for analogous membranes containing different amounts of C18 Cer. A similar phase separation was also reported for mixtures of C16 SM, C16 Cer, cholesterol, and palmitoyl-oleoyl-phosphatidylcholine.[35] The phase assignment for the samples examined in this work was also confirmed by the FCS data. In both "C16" and "C18" samples, the lowest phase has a diffusion coefficient of ~5 $\mu m^2/s$, comparable to that of a liquid-crystalline lipid environment (34,36,37). The intermediate phase is characterized by diffusion coefficients of $\sim 10^{-1}$ $\mu m^2/s$, similar to that measured in the L_o phase in supported membranes composed of SM, DOPC, and cholesterol (36). Finally, no apparent diffusion and a very low partition coefficient of fluorescent dye were measured for the highest lipid phase. Regarding the diffusion coefficient in the L_d phase, it is worth noting that its value is ~20% lower than that for the "No Cer" sample. This small difference is consistent with the possibility of a partial cholesterol displacement from ordered domains (13,38). Regarding the L_o phase, it is interesting to note that its dynamic properties are not influenced by the presence of long-chain Cer in the lipid bilayer. Furthermore, the packing density of the lipid chain does not change significantly, as the partition of the bulky BODIPY-CholE molecule between the L_d and the L_o phase is fully comparable in all the "No Cer", "C18", and "C16" samples. This implies that C18 and C16 Cer are able to recruit SM molecules forming a Cer-enriched phase (35) and leaving the remaining SM/cholesterol enriched phase unaltered. Panels A and B in Figure 7.7 show a simplistic view of the phase separation at room temperature so far described for "No Cer" and "C18"/"C16" samples, respectively.

Figure 7.7 Panel A shows then a SM/DOPC/cholesterol bilayer exhibiting a SM/cholesterol-enriched L_o phase and a DOPC-enriched L_d phase. Figure 7.7B shows that the same bilayer in the case of a long-chain Cer has partially substituted the SM. In this case, the L_d phase can be thought to contain more cholesterol, which was displaced away from ordered domains by Cer (13,38) Additionally, it is safe to assume that the amount of long-chain Cer in the L_d phase is very low (39). The L_o phase maintains its original lipid components, being constituted still by SM and cholesterol. Finally, the model bilayer contains a highly ordered gel phase, enriched mainly in SM and long-chain Cer (Cer-enriched phase).

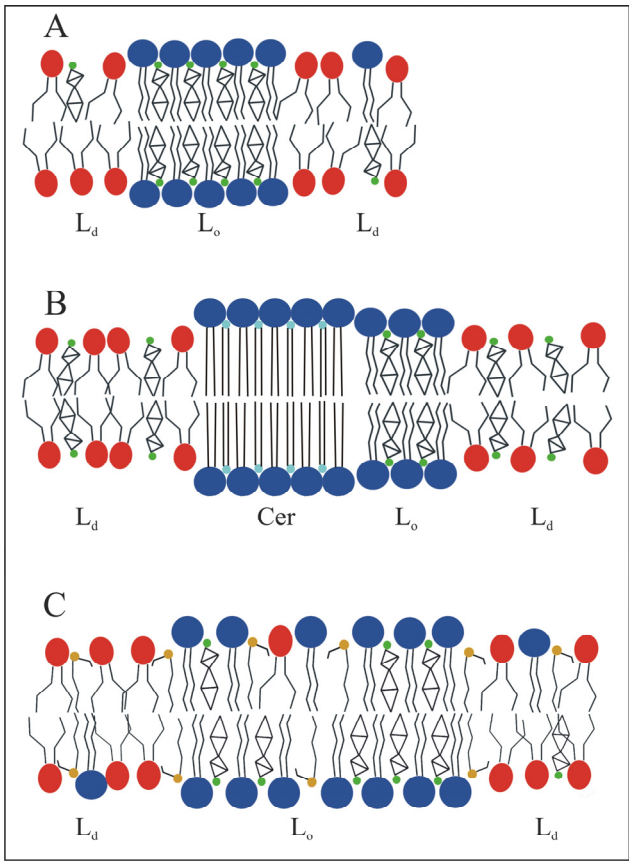

Figure 7.7 *Schematic model for phase separation at room temperature in presence of long- and short-chain Cer. The lipid molecule represented are: DOPC (red), SM (dark blue), cholesterol (green), long-chain Cer (light blue), short-chain Cer (brown). Panel A represents the phase separation observed in 'No Cer' samples. Panel B refers to samples containing long-chain Cer, i.e. C18 or C16 Cer. Panel C refers to samples containing short-chain Cer, i.e. C12, C6 or C2 Cer.*

7.4.2 Short-chain Cer – C12, C6 and C2

A rather different situation is observed in the presence of a short-chain Cer like C12, C6, or C2. In this case, in fact, AFM imaging reveals only the presence of two phases, characterized by microscopic domains ~0.6 nm thicker than the rest of the membrane. FCS measurements confirm that the two phases are in the L_o and L_d state, respectively. The lower phase is characterized by diffusion coefficients between ~5 and 6 $\mu m^2/s$ for all the short-chain Cer samples we have examined, and no significant differences between these and the "No Cer" SLBs were observed. Conversely, the L_o phase is strongly influenced by the presence of short-chain Cer, the magnitude of the effect depending on the Cer chain length. The diffusion coefficient of BODIPY-CholE remarkably increases as a function of chain length, especially in the case of C6 Cer. Furthermore, the amount of fluorescent probe in L_o domains for this kind of samples is significantly larger than that in "No Cer" samples. Taken together, these observations suggest a perturbation of the lipid-lipid interaction in the raftlike L_o domains. Short-chain Cer do not segregate in a separate phase and mix at least with the lipids in the L_o phase, thereby altering the molecular packing behavior. The high structural order in this phase derives from the optimal interaction between cholesterol and SM. The two lipids have a complementary structure: the small polar head of cholesterol fits between the large headgroups of SM, and its flat hydrophobic part can be accommodated between the long saturated chains without disrupting their van der Waals interactions (4). Conversely, the hydrophobic moiety of short-chain Cer has different geometrical properties that do not match well with the high degree of structural order in the SM/cholesterol L_o phase. As a consequence, the addition of short-chain Cer to the L_o phase might perturb the interactions among SM molecules, thereby significantly decreasing the translational order of the bilayer.

As was pointed out by Nybond et al. (27), in the case of C2 Cer, the very short acetyl-chain is most probably located entirely at the water/lipid interface. In C4 or C6 Cer, the acetyl chain might wobble between the aqueous phase and the hydrophobic core, thus perturbing the lipid packing in its vicinity. Finally, if the acetyl chain has more than eight carbon atoms, it should be increasingly embedded in the bilayer. The ineffective lipid packing would produce a local abrupt fall in methylene density, which would most probably be compensated by an increased mobility of the surrounding acyl chains. According to these notions then, it is reasonable that the lipid packing in the L_o phase is altered most in the "C6" samples, even more than in the presence of C2 or C12 Cer. The experimental observation that C2 has a smaller effect compared to C6 (e.g., in terms of perturbation of the ordered phase) was also observed in other studies (18), and it was proposed to be due to the lower partition of C2 in the bilayer phase.

It is worth noting that, differently from previous studies that indicated C8 Cer as still belonging to the group of long-chain Cer (26), our experiments indicate that C12 Cer behaves indeed as a short-chain Cer for the lipid mixture we analyzed. We did not observe, in fact, gel/L_o/L_d phase coexistence in the presence of C12 Cer and the lipid packing in the L_o phase was decreased, even if to a small extent.

The reduced domain size observed in "C6" and "C2" samples suggests a reduction in the line tension between the L_d and L_o phase. This observation might be related again to the peculiar geometrical properties of short-chain Cer, which could be thus accommodated at the interface of L_o domains in an energetically favored configuration. Finally, the increase of the surface area fraction covered by the L_d phase and the concomitant decrease measured for the L_o phase suggest that small amounts of SM, cholesterol and/or short-chain Cer might be dissolved in the L_d phase. Panel C in Figure 7.7 summarizes these last considerations, showing a simple model for the phase separation observed at room temperature for a SM/DOPC/cholesterol membrane in the presence of a short-chain Cer.

7.5 Conclusions and biological relevance

In this chapter, we described the application of AFM and FCS to study the lateral organization of raft-exhibiting bilayers, in presence of long- and short-chain Cer. Using this approach, it is possible to obtain precise structural information about the bilayer and to directly visualize the topological aspects of domain formation, which, combined with the local dynamic properties obtained from the FCS, allow for a better understanding of the lipid phase behavior.

Our results show that, at physiological concentrations, only C16 and C18 Cer form Cer-enriched domains, which consist of a highly ordered gel phase characterized by very slow dynamics. Remarkably, the L_o "raftlike" phase is hardly affected by the presence of these long-chain Cer. Conversely, C12, C6, and C2 Cer do not segregate into separate domains but are solubilized, at least, in the L_o phase. For these samples, the stability, the lipid packing, and the surface extension of the raftlike phase at room temperature are strongly reduced. The L_o properties of raft domains have a role in membrane protein signaling (40). Therefore, changes in their physical characteristics, like those reported in our work, could alter signal transduction and other cellular processes. Gidwani et al. reported, for example, that short-chain Cer inhibit phospholipase D activity and IgE-FcεRI signaling in RBL mast cells by disrupting the lipid order and destabilizing L_o domains (18).

In conclusion, long- and short-chain Cer show entirely different effects on the physical properties of lipid bilayers that exhibit liquid-liquid phase separation. Consequently, it seems

unlikely that the analogous physiological effects of short- and long-chain Cer are brought about by their behavior in the context of membrane organization and lipid-lipid interactions. Rather, it is possible that the Cer-dependent response triggered in *in vivo* experiments by short-chain Cer is related to more complex biochemical processes that do not depend on the chain length of Cer, like binding between the polar head of Cer and a target protein (16), interference in phospholipids synthesis and protein kinase B survival pathway (41), or long-chain Cer synthesis stimulation by exogenous short-chain analogues (42).

7.6 References

(1) Simons, K.; Ikonen, E. *Nature* **1997**, *387*, 569-572.
(2) Anderson, R. G. *Annu.Rev.Biochem.* **1998**, *67*, 199-225.
(3) Mayor, S.; Rao, M. *Traffic.* **2004**, *5*, 231-240.
(4) Simons, K.; Vaz, W. L. *Annu.Rev.Biophys.Biomol.Struct.* **2004**, *33*, 269-295.
(5) Kolesnick, R. N.; Goni, F. M.; Alonso, A. *J.Cell Physiol* **2000**, *184*, 285-300.
(6) Bollinger, C. R.; Teichgraber, V.; Gulbins, E. *Biochim.Biophys.Acta* **2005**, *1746*, 284-294.
(7) Hannun, Y. A. *Science* **1996**, *274*, 1855-1859.
(8) Gulbins, E.; Dreschers, S.; Wilker, B.; Grassme, H. *J.Mol.Med.* **2004**, *82*, 357-363.
(9) Radin, N. S. *Eur.J.Biochem.* **2001**, *268*, 193-204.
(10) Kester, M.; Kolesnick, R. *Pharmacol.Res.* **2003**, *47*, 365-371.
(11) Sot, J.; Goni, F. M.; Alonso, A. *Biochim.Biophys.Acta* **2005**, *1711*, 12-19.
(12) Small, D. M. *Fed.Proc.* **1970**, *29*, 1320-1326.
(13) Chiantia, S.; Kahya, N.; Ries, J.; Schwille, P. *Biophys.J.* **2006**, *90*, 4500-4508.
(14) Veiga, M. P.; Arrondo, J. L.; Goni, F. M.; Alonso, A. *Biophys.J.* **1999**, *76*, 342-350.
(15) Holopainen, J. M.; Angelova, M. I.; Kinnunen, P. K. *Biophys.J.* **2000**, *78*, 830-838.
(16) Goni, F. M.; Alonso, A. *Biochim.Biophys.Acta* **2006**, *1758*, 1902-1921.
(17) Venkataraman, K.; Futerman, A. H. *Trends Cell Biol.* **2000**, *10*, 408-412.
(18) Gidwani, A.; Brown, H. A.; Holowka, D.; Baird, B. *J.Cell Sci.* **2003**, *116*, 3177-3187.
(19) Di Paola, M.; Cocco, T.; Lorusso, M. *Biochemistry* **2000**, *39*, 6660-6668.
(20) Ghidoni, R.; Sala, G.; Giuliani, A. *Biochim.Biophys.Acta* **1999**, *1439*, 17-39.
(21) Goni, F. M.; Contreras, F. X.; Montes, L. R.; Sot, J.; Alonso, A. *Biochem.Soc.Symp.* **2005**, 177-188.
(22) Montes, L. R.; Ruiz-Arguello, M. B.; Goni, F. M.; Alonso, A. *J.Biol.Chem.* **2002**, *277*, 11788-11794.
(23) Sot, J.; Aranda, F. J.; Collado, M. I.; Goni, F. M.; Alonso, A. *Biophys.J.* **2005**, *88*, 3368-3380.
(24) Huang, H. W.; Goldberg, E. M.; Zidovetzki, R. *Eur.Biophys.J.* **1998**, *27*, 361-366.
(25) Sot, J.; Bagatolli, L. A.; Goni, F. M.; Alonso, A. *Biophys.J.* **2006**, *90*, 903-914.
(26) Carrer, D. C.; Schreier, S.; Patrito, M.; Maggio, B. *Biophys.J.* **2006**, *90*, 2394-2403.
(27) Nybond, S.; Bjorkqvist, Y. J.; Ramstedt, B.; Slotte, J. P. *Biochim.Biophys.Acta* **2005**, *1718*, 61-66.
(28) Saslowsky, D. E.; Lawrence, J.; Ren, X.; Brown, D. A.; Henderson, R. M.; Edwardson, J. M. *J.Biol.Chem.* **2002**, *277*, 26966-26970.
(29) Schwille, P.; Korlach, J.; Webb, W. W. *Cytometry* **1999**, *36*, 176-182.
(30) Petrov, E.; Schwille P. *Standardization in fluorometry: state of the art and future challenges* **2007**, U. Resch-Genger editor, Springer, Berlin Heidelberg New York. In press.
(31) Benda, A.; Benes, M.; Marecek, V.; Lhotsky, A.; Hermens, W.T.; Hof M. *Langmuir* **2003**, 19, 4120-4126.
(32) Chiantia, S.; Kahya, N.; Schwille, P. *Langmuir* **2005**, *21*, 6317-6323.
(33) Crane, J. M.; Tamm, L. K. *Biophys.J.* **2004**, *86*, 2965-2979.
(34) Kahya, N.; Scherfeld, D.; Bacia, K.; Poolman, B.; Schwille, P. *J.Biol.Chem.* **2003**, *278*, 28109-28115.
(35) Silva, L. C.; de Almeida, R. F.; Castro, B. M.; Fedorov, A.; Prieto, M. *Biophys.J.* **2007**, *92*, 502-516.
(36) Chiantia, S.; Ries, J.; Kahya, N.; Schwille, P. *Chemphyschem.* **2006**, *7*, 2409-2418.
(37) Bacia, K.; Scherfeld, D.; Kahya, N.; Schwille, P. *Biophys.J.* **2004**, *87*, 1034-1043.
(38) Megha; London, E. *J.Biol.Chem.* **2004**, *279*, 9997-10004.

(39) Wang, T. Y.; Silvius, J. R. *Biophys.J.* **2003**, *84*, 367-378.
(40) Brown, D. A.; London, E. *J.Biol.Chem.* **2000**, *275*, 17221-17224.
(41) van Blitterswijk, W. J.; van der Luit, A. H.; Veldman, R. J.; Verheij, M.; Borst, J. *Biochem.J.* **2003**, *369*, 199-211.
(42) Ogretmen, B.; Pettus, B. J.; Rossi, M. J.; Wood, R.; Usta, J.; Szulc, Z.; Bielawska, A.; Obeid, L. M.; Hannun, Y. A. *J.Biol.Chem.* **2002**, *277*, 12960-12969.

Chapter 8 – Membrane protein organization and ceramide-rich domains

The experiments described in this chapter have been performed in collaboration with Jonas Ries.

8.1 Introduction

In the last decade, several studies identified a novel membrane domain based on the sphingolipid ceramide, which plays an important role in a multitude of cellular processes ranging from differentiation to immune response and apoptosis (1-7). It is important to stress that, at least in the context of simple model membrane systems, it is possible to distinguish "lipid rafts", which are L_o domains enriched in SM and cholesterol, from "ceramide-rich domains", highly ordered gel domains that exclude cholesterol (see chapters 6 and 7 of this thesis and Ref. 8-17).

The interplay between rafts and ceramide domains is thought to be involved in the internalization of viruses and parasites and in the induction of apoptosis (18). Ceramide-rich platforms may act in these situations as sorting locations for membrane receptors, inhibitors and other membrane components involved in signaling (19). For example, ceramide-rich domains seem to recruit the receptors mediating the internalization of *N. gonorrhoeae* (20). Similar receptor clustering and trapping in ceramide-rich domains is also suggested by experiments performed with Fcγ receptor II (21), CD95 and CD40 (22,23). Nevertheless, since the ceramide phase is characterized by tight packing of lipids and high structural order, it seems counter-intuitive that certain membrane proteins would partition strongly into these rigid domains (15). Until now, no biophysical study concerning the affinity of membrane proteins or sphingolipids (other than SM and ceramide) for the ceramide-rich domains has been reported.

In order to address this question, we used a combined approach of atomic force microscopy (AFM), fluorescence imaging, and scanning fluorescence correlations spectroscopy (scanning FCS) to study the partitioning of membrane components into different lipid phases. Specifically, we produced supported bilayers showing a coexistence of L_d phase, L_o raft-like phase and ceramide-rich gel phase. We investigated the lateral organization of L_d-associated membrane components — i.e. fluorescent lipid analogues and the synaptic membrane protein Synaptobrevin 2 — and two typical raft-associated membrane components — i.e. the glycosylphosphatidylinositol anchored protein placental alkaline phosphatase (GPI-PLAP), and cholera toxin (CT*x*-B) bound to G_{M1} —. In order to obtain quantitative data about the partitioning of fluorescent molecules into the different lipid phases, we used a novel technique based on scanning FCS. Use of scanning FCS instead of classic FCS makes it possible to obtain reliable data even in the case of very slow diffusion and strong bleaching of the membrane components which are present in the highly viscous regions of the membrane, such as the ceramide-rich domains. Furthermore, this technique allows us to neglect changes in brightness of the fluorophores in different lipid environments that arise because of selective excitation, quenching or environmental sensitivity.

Our results show that membrane components with a low capacity to partition into the raft-like L_o phase tend to be completely excluded from the tightly packed ceramide domains. On the contrary, GPI-PLAP and CT*x*-B, which usually show a remarkably high degree of

partitioning into the L_o phase[1], seem to be concentrated in the ceramide-rich phase. Nevertheless, the affinity for the L_o phase is not by itself sufficient for the inclusion in ceramide domains, as exemplified by the case of the novel fluorescent free cholesterol analogue BODIPY-FChol. Furthermore, while the addition of ceramide does not appreciably change the dynamic properties of the membrane components in the L_d and L_o phases, very slow ($<<0.1\ \mu m^2/s$) diffusion is observed for the proteins enriched in the ceramide phase. These findings strongly support the hypothesis that ceramide domains may act in vivo as protein/lipid platforms that recruit or exclude specific membrane components (e.g. from small transient rafts), clustering them stably together and effectively slowing their in-plane diffusion.

8.2 Materials and methods

8.2.1 Chemicals

See section 4.2.1 for lipids and buffers. BODIPY free cholesterol analogue 23-(4,4-difluoro-1,3,5,7-tetramethyl-4-bora-3a,4a-diaza-*s*-indacen-8-yl)-24-norchol-5-en-3β-ol (BODIPY-FChol) was synthesized as described in (25). Dioctadecyl-3,3,3′,3′-tetramethylindodicarbocyanine perchlorate (DiD-C18, DiD), cholesteryl 4,4-difluoro-5, 7-dimethyl-4-bora-3a, 4a-diaza-*s*-indacene-3-dodecanoate (cholesteryl ester BODIPY FL C_{12},, BODIPY-CholE) and Alexa Fluor 488 cholera toxin subunit B (CT*x*-B) were from Invitrogen (Eugene, OR). Optical Adhesive 88, used to glue the mica on coverslips, was purchased from Norland Products (Cranbury, NJ). Alkaline phosphatase from human placental tissue (PLAP), 3-((3-cholamidopropyl) dimethylammonio)-1-propanesulfonic acid (CHAPS) and sodium cholate were purchased from Sigma. Before use, PLAP was purified and labelled with NHS-rhodamine (Pierce, Rockford, IL) using a protocol modified from (26) and (27). In particular, high-resolution Superdex200 10/300GL (GE-Healthcare) columns were used instead of Sephacryl S200 and, after labelling, a Nap-5 (GE-Healthcare) and an additional Superdex columns were used to exclude free dye and protein dimers.

Recombinant protein Synaptobrevin 2 (residues 1–117C) was expressed, purified and labeled with Cy5 maleimide (Amersham Biosciences) as described in (28) and (29).

.

8.2.2 Supported lipid bilayers (SLBs)

Planar bilayers were prepared based on the procedure described in section 4.2.2 (30).

8.2.3 Protein-containing SLBs

In the case of membranes containing rhodamine-labeled PLAP, the liposomes were used to produce proteoliposomes before deposition onto mica, using a modification of the procedure described by Kahya et al. (26) In particular, the protein and 100 nm extruded liposomes (without ceramide) were mixed in buffer A to final concentrations of 40 μg/mL and 2.5

[1] Compared to other lipid analogues and membrane proteins like SNAREs and Bacteriorhodopsin [24]

mg/mL, respectively, in the presence of 1.8% CHAPS. The liposomes´ extrusion was performed twice: i) before adding CHAPS and ii) before adding the protein. The initial protein:lipid ratio was ~1:2500. After 24 h of dialysis against buffer A using a 50 kDa SpectraPro membrane (Spectrum, Breda, Netherlands), a small aliquot was diluted 10 times in buffer B, briefly sonicated with ceramide-containing liposomes in the desired proportions at 50° C, and deposited onto mica as described above for the normal, protein-free, liposomes. The final protein:lipid ratio was then ~1:8000. The activity of the reconstituted protein was checked by enzymatic digestion of Sigma Fast *p*-nitrophenyl phosphate (Sigma) in the solution above the SLB.

SLBs containing Synaptobrevin 2 were prepared from proteoliposomes as described by Bacia et al. (28) In particular, the protein and 100 nm extruded liposomes (without ceramide) were mixed in buffer A with ~1:2500 molar ratio, in the presence of 1.2% sodium cholate. The liposomes´ extrusion was performed twice: i) before adding sodium cholate and ii) before adding the protein. After 24 h of dialysis against buffer A using a 50 kDa SpectraPro membrane (Spectrum, Breda, Netherlands), a small aliquot was diluted 10 times in buffer B, briefly sonicated with ceramide-containing liposomes in the desired proportions at 50° C, and deposited onto mica as described above for the normal, protein-free liposomes. The final protein:lipid ratio was ~1:8500. The activity of the protein incorporated in the SLB was checked by specific binding to a fluorescent soluble syntaxing fragment (AA 183-262) (28).

In the case of samples stained with Alexa488 CT*x*-B, the SLBs contained 0.03% G_{M1}. The toxin (10 mg/mL) was added and washed away after 2 min incubation.

8.2.4 Optical setup

See section 4.2.3.

8.2.5 Scanning FCS

Data were acquired by scanning repeatedly the focal volume in a linear fashion in the membrane. Line scans of ca. 5-µm length were chosen such that all three phases were scanned through. Intensity traces of parts of the scans corresponding to only one phase were correlated scan by scan. To account for photo bleaching, correlation curves $G_i(\tau)$ were multiplied by the ratio between the average intensity of the corresponding scan I_i and the initial intensity I_0: $\widetilde{G}_i(\tau) = G_i(\tau) \cdot I / I_0$. Since the concentrations c_i are inversely proportional to amplitudes of the correlation curves (i.e. $G_i(0) \sim 1/c_i$) and directly proportional to the intensities ($I_i \sim c_i$,), $\widetilde{G}_i(\tau)$ is in this way scaled back to the initial correlation curve $G_0(\tau)$. The average of the rescaled correlation curves was fitted with a flow-diffusion model. Since the residence time of the scanned detection volume is much shorter than the diffusion time, the diffusional part of the correlation curves was very small. Therefore diffusion coefficients could be fixed to approximate value. By using the known velocity of the detection volume, the fit provided directly the size of the detection volume w_0 and, more importantly, the fluorophore concentration c.

Knowing the concentration of the fluorophores in the different phases (c_{Lo}, c_{Ld}, and c_{Cer}), we defined a "normalized partition" P_X for the phase X as:

$$P_X = \frac{c_X}{c_{Lo} + c_{Ld} + c_{Cer}} \quad (8.1)$$

In the case of samples without ceramide, P_X is simply:

$$P_X = \frac{c_X}{c_{Lo} + c_{Ld}} \quad (8.2)$$

8.2.6 Atomic Force Microscopy

See section 4.2.5.

8.3 Results and discussion

8.3.1 L_d phase-associated Protein Synaptobrevin is Excluded from Ceramide Domains

Synaptobrevin 2 belongs to the SNARE protein family, which is involved in the membrane fusion processes within the secretory pathway of eukaryotic cells. The lateral organization of SNARE proteins in the plasma membrane and their association to raft domains in vivo are still matter of debate (31,32,33). The determination of the affinity of a membrane component for raft domains often relies on detergent-resistance assays at low temperature. These procedures are in general prone to artifacts (34) and, in the case of Synaptobrevin for example, the outcome can be even influenced by the choice of the specific detergent (35). On the other hand, studies with model membranes clearly show that both Syntaxin 1 and Synaptobrevin 2 are preferentially associated with the L_d phase in lipid bilayers composed of DOPC, SM, and cholesterol (28,36). For this reason, we chose the same recombinant Synaptobrevin 2 used in Ref.(28) as a paradigm for a L_d-associated membrane component. In order to study its lateral organization in the presence of ceramide domains, we reconstituted Synaptobrevin 2 in supported bilayers showing a L_d/L_o/ceramide-rich phase coexistence.

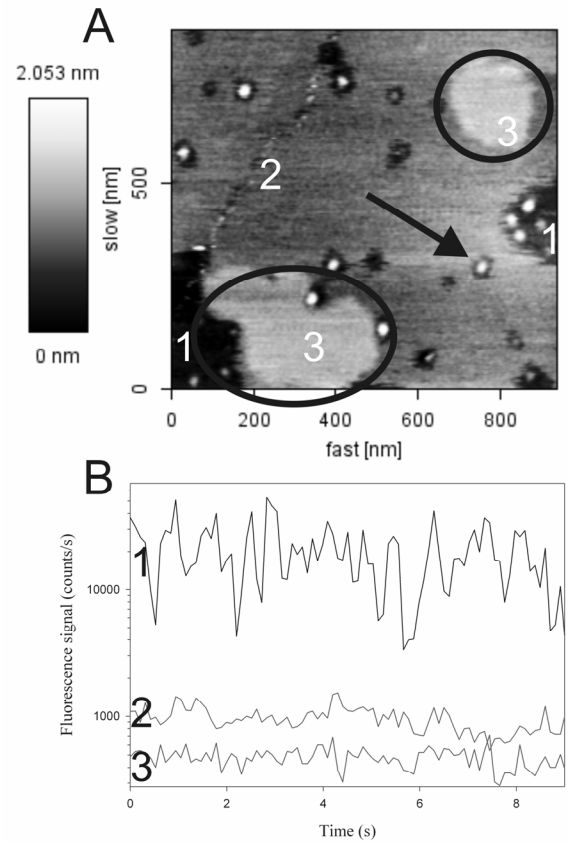

Figure 8.1 *Synaptobrevin 2 is excluded from ceramide-rich domains. A) AFM topographical image of a SM/DOPC/ceramide/cholesterol supported bilayer containing Synaptobrevin 2 at 25°C. The three topographical level in the figure represent the Ld (black, number 1), Lo (dark gray, number 2), and ceramide-enriched phase (light grey, number 3) respectively. The protein can be visualized as bright white protrusions, a few nm higher than the lipid membrane, probably corresponding to small clusters of up to ~10 Synaptobrevin 2 monomers. The circles show the ceramide-rich domains. The arrow indicates a Synaptobrevin 2 cluster in the Lo phase, surrounded by a thinner portion of membrane. B) Representative APD measurements of the fluorescence signal of the protein as a function of time in the Ld (1), Lo (2) and ceramide-rich (3) phases.*

We used membranes containing DOPC, SM, C18:0 ceramide, and cholesterol in a 1:0.7:0.3:0.67 molar ratio. Figure 8.1A shows an AFM topographical image of such a membrane, in which the three lipid phases can be distinguished based on the increasing thickness. The activity of the protein was verified as described in the Materials and Methods section. As was previously shown (13,37), in such supported bilayers the L_o phase is ~0.8 nm higher than the L_d phase, and the ceramide-rich phase is ~1.3 nm higher than the L_d phase. Fig. 8.1A shows the L_d phase as the darkest portions of the membrane, the L_o phase as a dark grey area and the ceramide-rich domains as light grey domains (evidenced by circles). Synaptobrevin reconstituted in the bilayer appears as small round spots, 1.2-2.0 nm higher than the rest of the membrane, which are not observed in pure lipid bilayers prepared under the same conditions (13). The average radius of these spots, measured at half height to minimize the error introduced by the geometry of the scanning tip (38), is 15-20 nm. In line with previous observations regarding Syntaxin 1 reconstituted in lipid bilayers (39), this result suggests that the round spots visualized by AFM are small immobile Synaptobrevin clusters, containing in this case approximatively ~10 monomers each. Fig. 8.1A shows that these clusters are observed mostly in the L_d phase, while they are completely excluded from the ceramide-rich domains. As it was pointed out in a recent work from our group (30), AFM might not be the method of choice for protein partition studies because small diffusing membrane components (e.g., Synaptobrevin monomers) might be undetected. AFM is used here to: i) correctly identify ceramide-rich and L_o domains and ii) monitor the presence of large aggregates of membrane proteins, especially in the ceramide-rich phase. Although the presence of immobile Synaptobrevin in the highly viscous ceramide domains should be easily detected by AFM, a complementary technique is necessary to confirm the absence of protein in these domains.

Because of the low protein concentration, LSM imaging does not convey a clear contrast between the different lipid phases (data not shown). Fluorescence imaging performed using highly sensitive APDs shows that the signal originating from Synaptobrevin 2 in both the L_d

and the L_o phase is significantly higher than that from the protein in the ceramide domains, the latter being comparable to background noise of ca. 300-400 photons per second (see Fig. 8.1B). The extremely low protein signal in the ceramide-rich phase precludes the possibility of performing further quantitative measurement (i.e. scanning FCS) of the protein partition behavior. Nevertheless, it is possible to conclude that the concentration of Synaptobrevin 2 in the ceramide-rich domains is well below the sensitivity of our setup (~1 molecule/μm^2). This result is consistent with studies that show that the ceramide-rich phase is characterized by a high degree of structural order (17,40), and the tight packing of the saturated lipid molecules might lead to the exclusion of bulky membrane components.

AFM imaging shows that the Synaptobrevin 2 clusters included in large L_o domains are very often surrounded by small lipid islets exhibiting a membrane height comparable to the L_d phase (see, for example, the arrow in Fig. 8.1A). If such islets are small compared to the optical resolution, they cannot be distinguished from the large L_o domains by means of fluorescence imaging. In this case, the fluorescent signal measured positioning the laser focus in the L_o phase could also include photons originating from proteins which are in fact surrounded by lipids most likely in the L_d phase. This local perturbation of the L_o phase, probably connected to the presence of the bulky membrane protein, might bias the estimation of the partition coefficient between L_d and L_o phase obtained from fluorescence microscopy without auxiliary high-resolution AFM data.

8.3.2 Enrichment of raft-associated membrane components in ceramide domains

I) GPI-PLAP is Enriched in Ceramide Domains

Many membrane proteins are tethered to the exoplasmic leaflet of plasma membranes via a post-translational lipid modification known as the glycosylphophatidylinositol (GPI) anchor (41,42). GPI-anchored proteins perform their function by association with raft domains in vivo (43,44,45,46). Therefore, we chose to study the organization of GPI-PLAP in the presence of L_d, L_o and ceramide domains, as a paradigm for raft-associated proteins.

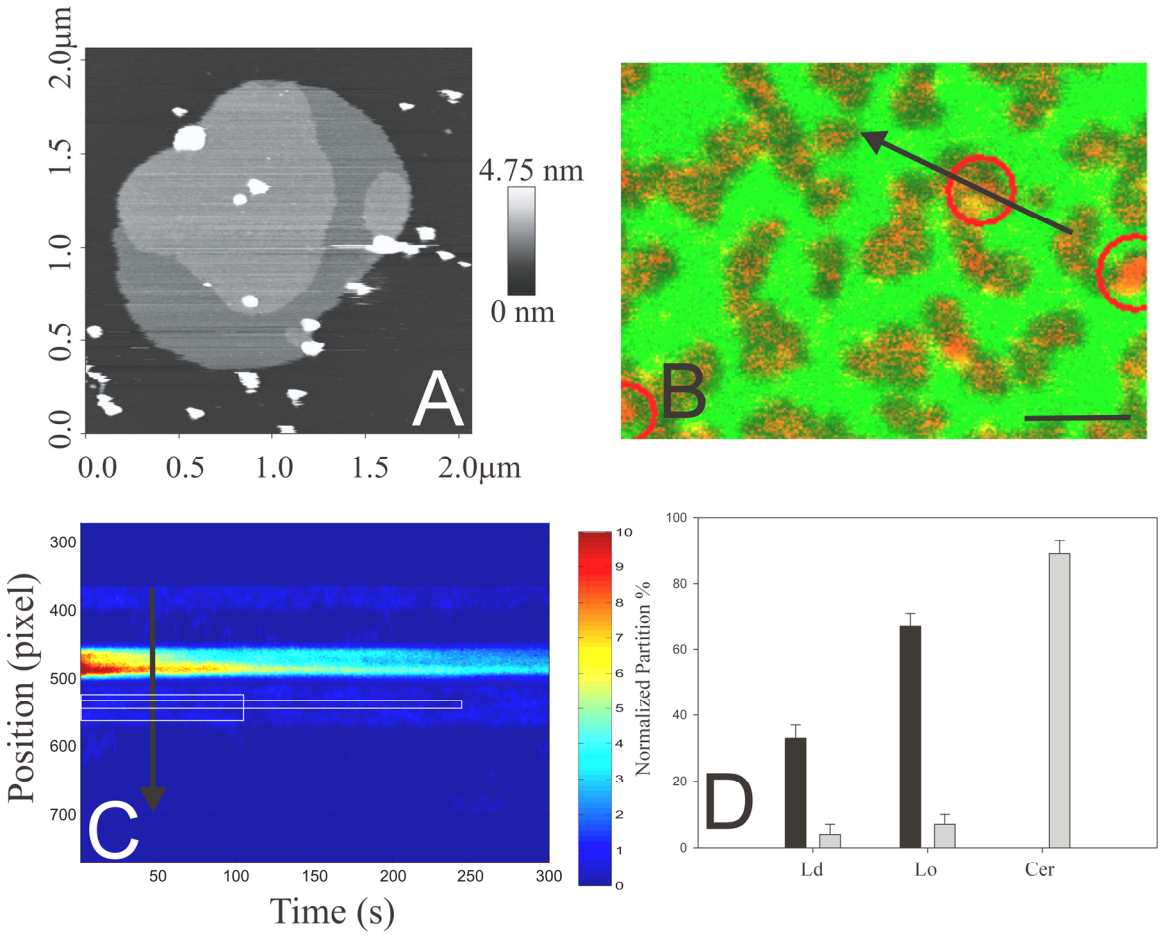

Figure 8.2 *GPI-PLAP is enriched in ceramide domains. A) AFM topographical image of a SM/DOPC/ceramide/cholesterol supported bilayer containing GPI-PLAP at 25°C. The three topographical levels in the figure are represented in black (Ld phase), dark gray (Lo phase), and light grey (ceramide-enriched phase). The protein can be visualized as white protrusions, a few nm higher than the lipid membrane, probably corresponding to slowly diffusing protein cluster/aggregates. B) LSM fluorescence imaging of the same sample. The green channel refers to the BODIPY-CholE in the Ld phase, and the red channel refers to the fluorescent GPI-PLAP. Red circles indicate ceramide-rich domains identified via parallel AFM imaging. The arrow represents the scanning path used for scanning FCS (see text). Scale bar = 2 micron. C) Complete visualization of all the scanning FCS lines collected in 300 seconds. Each line is represented vertically, as indicated by the black arrow. The lines are collected in the same part of the sample indicated by the arrow in panel B. The color code refers to the number of measured fluorescence photons. The white rectangles are examples of selected line portions used to calculate autocorrelation curves. D) Normalized partitioning of GPI-PLAP into different lipid phases (see text). In black, the partition measured in samples without ceramide (Ld Lo phase coexistence); in grey, the partition of the protein in sample containing ceramide (Ld / Lo /ceramide-rich phase coexistence).*

We reconstituted GPI-PLAP in supported bilayers with L_d/L_o/ceramide-enriched phase coexistence, as reported above for the Synaptobrevin 2 experiments. The activity of the protein was verified as described in the Materials and Methods section. AFM imaging shows the three lipid phases and the protein molecules (Fig. 8.2A). The lowest (L_d) phase is

represented in black, the middle-height (L_o) phase in dark grey and the high ceramide domains in light gray. As for the case of Synaptobrevin 2, the sharp high topographical features observed probably represent a small fraction of the reconstituted protein, in form of clusters and aggregates, which can be easily detected by AFM due to their low mobility (30). The half height radii of these particles are larger than those observed in the case of Synaptobrevin 2. They range from 15 nm to 160 nm, the largest values being observed in the ceramide-rich domains. The presence of large aggregates in the ceramide phase is unlikely to be an artifact, since it is reproducibly observed in the case of GPI-PLAP but not when Synaptobrevin 2 is reconstituted in the same lipid mixture (see Fig. 8.1A). As mentioned above, AFM is employed here only to distinguish the different lipid domains and to monitor the presence of protein aggregates. In order to investigate quantitatively the partitioning of GPI-PLAP in ceramide domains, we applied fluorescence microscopy and scanning FCS simultaneously on the same sample. Fig.8.2B shows LSM imaging of the bilayer using BODIPY-CholE enriched in the L_d phase (green channel) and Rhodamine-labeled GPI-PLAP (red channel). The L_o domains appear dark in the green channel. The red circles indicate ceramide-rich domains, localized via AFM imaging. The fluorescence intensity in the red channel indicates, in a qualitative way, that the GPI-PLAP is not excluded from the ceramide-rich domains. In order to quantitatively determine the partition coefficient of the GPI-PLAP in the different lipid phases, we measured its local concentration using scanning FCS. The arrow in Fig. 8.2B indicates a typical linear path in the plane of the membrane through which the focal volume was scanned in a continuous way, collecting the signal from the protein in the different phases. Between 10^3 and 10^4 lines were collected in ca. 200 s and arranged along the y-axis as shown in Fig. 8.2C. Therefore the y-axis denotes the position within each line scan, while the x-axis denotes the different acquired lines and is proportional to the time. The arrow indicates the direction in which each line scan from Fig. 8.2B is stored and represented. The different phases are clearly visible along the y-axis as stripes with different fluorescence intensities. Interestingly, the high signal from the protein in the ceramide-rich domain (located approximatively in the center of the line scan) decreases with time because of strong localized bleaching. As confirmed by classic FCS (data not shown), the diffusion coefficient of the protein in the ceramide-rich domains is below our instrumental limit ($<<0.01\ \mu m^2/s$), while the diffusion in both L_d and L_o phase is similar to what measured in the absence of ceramide domains (30,26).

At this point, it is possible to select portions of the scan path (e.g., the white rectangles in Fig. 8.2C for the L_d phase) and calculate the autocorrelation curve, therein for each line scan. The amplitudes of the individual autocorrelation curves were corrected for bleaching as explained in the Materials and Methods section. From the amplitude of the average autocorrelation curve we obtained the concentration of GPI-PLAP in the different membrane domains. Fig. 8.2D shows the normalized partition P of the protein in each lipid phase (see equations 1 and 2). In the case of simple L_d/L_o phase separation, P_{Lo} of GPI-PLAP is ~70%. This value is higher than what we previously measured for the same kind of protein in an analogous experiment (i.e., 40±5%)(30). We argue that the difference might be attributable to: i) the more accurate purification procedure we performed for the GPI-PLAP used in this work (see Materials and Methods) and/or ii) the statistical variation in saturation and length of the acyl/alkyl chains in the GPI moiety between different protein batches.

In bilayers showing L_d/L_o/ceramide-rich phase separation, P_{Cer} of GPI-PLAP was almost ~90%. Considering that the AFM data indicate a certain degree of protein aggregation in the ceramide-rich phase, this value may be underestimated because large GPI-PLAP clusters might appear as single (bright) particles in the scanning FCS measurements, thus lowering the apparent protein concentration.

Finally, it is worth noting that simple comparison of fluorescent intensities coming from the different lipid phases would lead to an almost 10-fold underestimation of the GPI-PLAP

enrichment in the ceramide domains (data not shown). In general, the partition coefficients derived from fluorescent intensities are significantly different from those derived from FCS-measured concentrations in all of the samples we have examined. This effect comes from the fact that the brightness of the same fluorophore in different lipid phases can change because of several factors, such as selective photo-excitation or environment-sensitive quenching (47). While these changes in fluorescence quantum yield can bias partition coefficients as measured using fluorescence imaging, they do not, however, affect those measured employing FCS or scanning FCS, which directly probe the concentrations of fluorophores.

In conclusion, these results showed that GPI-PLAP is strongly enriched in the ceramide domains where its diffusion is dramatically decreased.

II) Cholera Toxin is Enriched in Ceramide Domains

The B- subunit of cholera toxin *(CTx-B)* binds to the ganglioside G_{M1} and therefore is used as a typical marker for raft domains in cell and model membranes (48,49). In order to study the affinity for ceramide-rich domains of this protein that binds to raft lipids, we used the same methodology described above for GPI-PLAP. Fig. 8.3A shows the fluorescence image of a supported bilayer containing SM, DOPC, cholesterol, and G_{M1} ($1:1:0.67:0.27\cdot10^{-3}$ molar ratio). This lipid composition displays a simple L_d/L_o phase coexistence and DiD (red channel) was included to visualize the L_d phase (30). Under these conditions, the green fluorescent *CTx-B* binds uniformly to the L_o phase, as shown in Fig. 8.3A. The arrows in Fig. 8.3A indicate examples of occasional lipid aggregates or non-fused vesicles which appear bright in both the red and the green channels.

When SM is partially substituted with C18:0 ceramide, as described above for the Synaptobrevin 2 or GPI-PLAP experiments, the *CTx-B* is still enriched in the portions of the membrane that exclude DiD, but its spatial distribution is no longer homogeneous in such domains (Fig. 8.3B). As shown by parallel AFM imaging of the same supported membrane (Fig. 8.3C), *CTx-B* seems to be concentrated in the ceramide-rich domains, that are ca. 1.2 nm higher than the L_d phase enriched in DiD. Using scanning FCS, as described above for the GPI-PLAP experiments, we calculated the normalized partition P of *CTx-B* for the different lipid domains, both in the absence of ceramide (L_d/L_o phase coexistence) and in the presence of ceramide (L_d/L_o/ceramide-rich phase coexistence). As shown in Fig. 8.3D, more than 80% of the *CTx-B* molecules partition to the ceramide-enriched domains.

Again, the strong localized bleaching of the protein in the ceramide domains, observed both in classic (data not shown) and scanning FCS, suggests strongly hindered local dynamics. Hence we conclude that, similarly to what was observed for GPI-PLAP, the G_{M1}-bound *CTx-B* is highly concentrated and diffuses very slowly ($<<0.01\ \mu m^2/s$) in ceramide-rich domains.

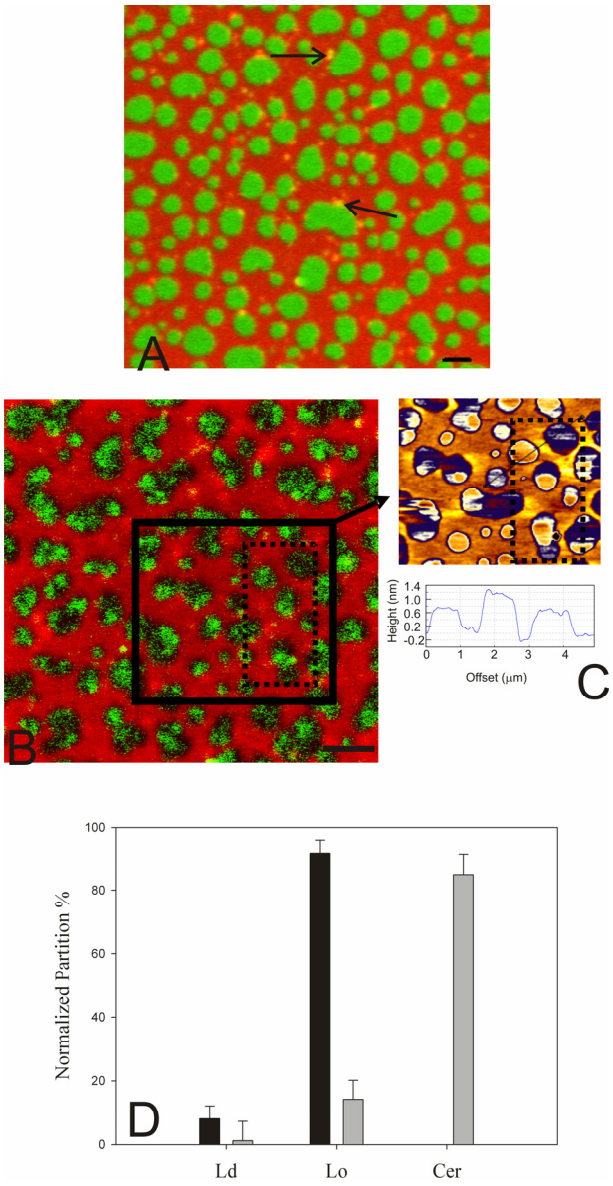

Figure 8.3 *CTx-B is enriched in ceramide domains. A) LSM fluorescence image of a SM/DOPC/cholesterol supported bilayer at 25°C. The red channel refers to the DiD in the Ld phase, and the green channel refers to the CTx-B enriched in the Lo phase. The arrows indicate small lipid aggregates or non-fused vesicles which appear bright in both the red and the green channels. Scale bar = 2 μm. B) LSM fluorescence image of a SM/ DOPC/ ceramide/ cholesterol supported bilayer containing the same fluorescent probes as in panel A. The solid black rectangle indicates the zone of the bilayer imaged by AFM at the same time. The dotted rectangle helps the comparison with panel C. Scale bar = 2 μm. C) AFM topographical image of the same bilayer shown in the black rectangle in panel B and the relative cross section. D) Normalized partitioning P of CTx-B into the different lipid phases. The values are calculated as the local concentration normalized with the sum of the concentrations in each phase. In black, the partition measured in samples without ceramide (Ld/Lo phase coexistence); in grey, the partition of the protein in sample containing ceramide (Ld/Lo/ceramide-rich phase coexistence).*

The fact that both these membrane components are enriched in the ceramide phase is a surprising result. Firstly, while the lipid chains of the G_{M1} to which *CTx-B* is bound are long and saturated, the GPI-anchor of PLAP possesses both C18:0/C18:1 or C18:0/C16:0 lipid chains in different proportions (50). One could expect that the presence of unsaturated acyl chain might disrupt the ordered lipid packing in the ceramide-rich gel phase. Secondly, even though the partitioning of G_{M1} into the ceramide domains could be favored by increased chain-chain interactions or hydrogen-bond formation between the sphingosine backbones of G_{M1} and Cer or SM (51), the bulky hydrophilic moieties of both *CTx-B* and GPI-PLAP might perturb the hydrogen-bond network (5) around the polar head groups of the lipids constituting the ceramide-rich domains.

Nevertheless, the partitioning of GPI-PLAP and the G_{M1}-*CTx-B* complex into the ceramide-rich domains seems to be energetically favorable, at least at the low protein concentration we used. At these protein:lipid ratios, neither the conformational nor the translational order of the ceramide-rich phase are strongly perturbed, as measured by AFM and FCS, respectively. The observation that some raft-associated molecules are enriched in ceramide domains can be rationalized if the molecular mechanism behind the selective inclusion/exclusion in ceramide-rich domains arises from physical characteristics common to both L_o and ceramide-rich phase.

For example, changes in hydrophobicity and bilayer thickness, both increasing when going from L_d to L_o to ceramide-rich phase, might be involved in the specific partitioning behavior on some membrane components (52).

Interestingly, upon ceramide generation, clustering of GPI-CD40 and strong co-localization with *CTx-B* was observed in in vivo studies (22). The same observations were made in the case of the GPI-anchored CD48 receptor (53). According to these findings and to our results in model membranes, the production of ceramide in already existing sphingolipid-rich L_o domains might result in the formation of ceramide-rich signaling microdomains. These domains may in turn trigger the clustering of receptors that were already in raft-like domains, and modify their diffusion behavior. Trapping of these receptors in ceramide domains and subsequently reducing their diffusion could favor sustained signaling from the membrane.

8.3.3 Fluorescent Lipid Analogues with Different Affinities for the L_o Phase are Excluded from Ceramide Domains

For the membrane components we have examined thus far, the partitioning between the L_d and L_o phases seems to be important in determining the affinity for the ceramide-rich phase. In order to determine whether partitioning of a membrane component in the ceramide domains is solely dependent on its affinity for the L_o phase, we analyzed several fluorescent lipids with different partition behavior between the L_o and L_d phases. The P_{Lo} of the fluorescent analogues we used ranged from ~0.4% (DiD(30)) to ~45% (the fluorescent sterol BODIPY-FChol) for membranes showing simple L_d/L_o phase coexistence. We incorporated the fluorescent lipids in supported bilayers containing DOPC, SM, C18:0-Cer and cholesterol in a 1:0.7:0.3:0.67 molar ratio. Fig. 8.4A shows, in the red channel, the signal from DiD and, in the green channel, that from the BODIPY-FChol. Interestingly, the fluorescent sterol is almost homogenously distributed in the entire membrane, with the exception of the ceramide-rich domains. Both the L_o and ceramide-rich phases appear dark in the red channel.

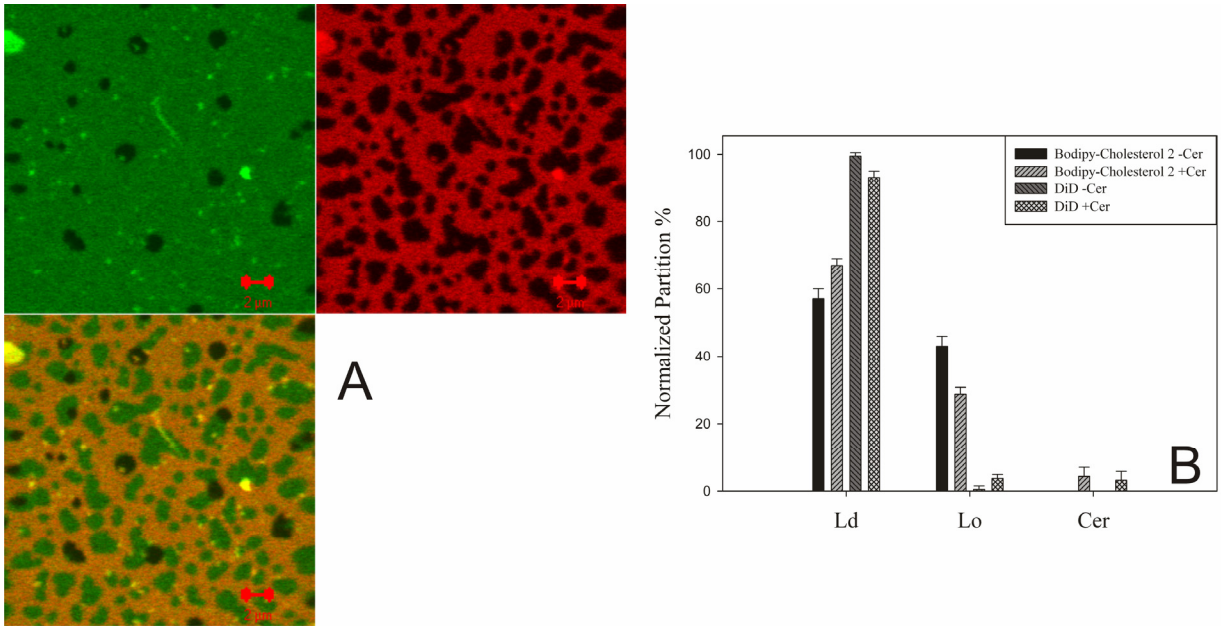

Figure 8.4 *Fluorescent lipid analogues are excluded from ceramide domains. A) LSM fluorescence image of a SM/ceramide/DOPC/cholesterol supported bilayer at 25°C. The*

green channel refers to BODIPY-FChol and the red channel refers to DiD. The dark zones in both channels are ceramide-rich domains. Scale bar = 2 micron. B) Normalized partitioning of BODIPY-FChol and DiD into different lipid phases. For each fluorescent dye, the normalized partitioning is indicated both in case of L_d/L_o phase coexistence (-Cer) and L_d/L_o/ceramide-rich phase coexistence (+Cer).

More quantitatively, Fig. 8.4B shows the affinity of the two fluorescent lipids for the three examined lipid phases obtained with scanning FCS. Interestingly, both DiD and BODIPY-FChol show a very low affinity for the ceramide-rich domains, although their partitioning in the L_o phase is dramatically different and almost half of the BODIPY-FChol partitions in the L_o phase in samples without ceramide. A low extent of partitioning into ceramide-domains was also observed for BODIPY-CholE (14), BODIPY-C5-Cer, and BOPIDY-DPPE. For all three dyes, we also observed a significant extent of partitioning into the L_o phase, with a P_{Lo} as high as ~25% for BODIPY-C5-Cer (30). Similarly, Silva et al. observed the exclusion of many fluorescent dyes from C16:0 ceramide-rich domains, with the only exception being *trans*-parinaric acid (17).

The high P_{Lo} of BODIPY-FChol in membranes displaying L_o/L_d phase coexistence, although still less than 50%, suggests that this fluorescent lipid is a reliable probe for non-labeled, natural cholesterol in optical microscopy, compared to other available fluorescent sterol analogues (see also (54)). In spite of its favorable interactions with SM (i.e., a relatively high P_{Lo}), this fluorescent sterol is nevertheless excluded from ceramide-rich domains, probably because of the competition with ceramide molecules (55). It is worth noting that, to the best of our knowledge, this is also the first direct optical visualization of the ceramide-induced cholesterol displacement hypothesis (55,55b).

These results suggest that the affinity for L_o domains might be necessary for inclusion in ceramide-rich domains, but does not appear to be in general sufficient, as exemplified by BODIPY-FChol.

8.4 Conclusions and biological relevance

We have investigated the influence of ceramide in the lateral organization of several membrane components in supported bilayers showing L_d/L_o/ceramide-rich phase separation. Our results show for the first time in a model, well-controlled system, that some membrane proteins are preferentially distributed into ceramide-rich domains. More specifically, the raft-associated proteins GPI-PLAP and *CTx-B* are enriched in the highly ordered ceramide-rich domains, while several fluorescent lipid analogues and the L_d-associated protein Synaptobrevin 2 are excluded from them. Furthermore, the inclusion of a membrane component in ceramide-rich domains is directly connected to a dramatic reduction of its in-plane diffusion. On the other hand, the diffusion of non raft-associated components or of the raft-associated ones in both L_d and L_o phases are not strongly influenced by the presence of ceramide-rich domains, in agreement with previous measurements (14).

In an in vivo context, such a reorganization of membrane receptors might be used by the cell to alter the signaling process. For example, ceramide platforms could i) exclude inhibitors with lower raft affinity (e.g. CD45 inhibiting GPI-CD40 (22)), ii) bring in closer contact receptors and signaling molecules both raft associated (e.g., FCγRII and Lyn kinase (21)), or iii) stabilize the interactions between a receptor and its ligand by decreasing their diffusion coefficients (56). Our data support these scenarios, as the membrane components we examined displayed a strong ceramide-induced alteration of their local concentration (see i)

and ii)) and their diffusion behavior (see iii)), in connection to their affinity toward the raft-like phase.

The finding that ceramide production protects cells from HIV infection (57) might also be interpreted according to our results. Upon sphingomyelinase action, the raft associated receptor CD4 is clustered and its diffusion is slowed (58). Interestingly, in agreement with our findings in the simple model we used, the mobility of the nonraft-associated co-receptor CCR5 is not affected by ceramide production (58). It is thus possible that CD4 is sequestered in ceramide-enriched domains, where its mobility is drastically reduced and the partitioning of the non raft-associated CCR5 is extremely low (59). Since HIV fusion requires receptor mobility and contact between CD4 and CCR5, immobilizing CD4 in ceramide-rich domains most likely inhibits viral fusion at the step of co-receptor engagement (59,60,61). A deeper understanding of such a mechanism obviously requires further studies involving the reconstitution of more complex membrane proteins (for example, with the purified CD4 receptor).

In conclusion, we used a combined approach of AFM, LSM, and scanning FCS to probe the partition behavior of different membrane components in the presence of raft-like and gel phase, ceramide-rich domains. Our results show that only some raft-associated components were enriched and immobilized in ceramide domains. The L_d-associated protein Synaptobrevin 2 and many lipid analogues with different affinity toward the L_o phase were almost completely excluded from ceramide-rich domains. Similar rearrangements of membrane proteins may be of crucial importance in regulating signal transduction in biological contexts in which ceramide is produced in the cell membrane.

These results also show that the combined approach of AFM and scanning FCS on supported lipid bilayers of increasing complexity is a promising tool for understanding the molecular mechanisms behind ceramide-induced reorganization of membrane components in living cells.

8.5 References

(1) K. Simons,E. Ikonen, Functional rafts in cell membranes, Nature. 387 (1997) 569-572.

(2) K. Simons,W. L. Vaz, Model systems, lipid rafts, and cell membranes, Annu. Rev. Biophys. Biomol. Struct. 33 (2004) 269-295.

(3) R. G. Anderson, The caveolae membrane system, Annu. Rev. Biochem. 67 (1998) 199-225.

(4) S. Mayor,M. Rao, Rafts: scale-dependent, active lipid organization at the cell surface, Traffic. 5 (2004) 231-240.

(5) R. N. Kolesnick, F. M. Goni,A. Alonso, Compartmentalization of ceramide signaling: physical foundations and biological effects, J. Cell Physiol. 184 (2000) 285-300.

(6) C. R. Bollinger, V. Teichgraber,E. Gulbins, Ceramide-enriched membrane domains, Biochim. Biophys. Acta. 1746 (2005) 284-294.

(7) Y. A. Hannun, Functions of ceramide in coordinating cellular responses to stress, Science. 274 (1996) 1855-1859.

(8) A. E. Cremesti, F. M. Goni,R. Kolesnick, Role of sphingomyelinase and ceramide in modulating rafts: do biophysical properties determine biologic outcome?, FEBS Lett. 531 (2002) 47-53.

(9) J. C. Fanzo, M. P. Lynch, H. Phee, M. Hyer, A. Cremesti, H. Grassme, J. S. Norris, K. M. Coggeshall, B. R. Rueda, A. B. Pernis, R. Kolesnick,E. Gulbins, CD95 rapidly clusters in cells of diverse origins, Cancer Biol. Ther. 2 (2003) 392-395.

(10) T. A. Nurminen, J. M. Holopainen, H. Zhao,P. K. Kinnunen, Observation of topical catalysis by sphingomyelinase coupled to microspheres, J. Am. Chem. Soc. 124 (2002) 12129-12134.

(11) D. C. Carrer,B. Maggio, Phase behavior and molecular interactions in mixtures of ceramide with dipalmitoylphosphatidylcholine, Journal of Lipid Research. 40 (1999) 1978-1989.

(12) L. Silva, R. F. de Almeida, A. Fedorov, A. P. Matos,M. Prieto, Ceramide-platform formation and -induced biophysical changes in a fluid phospholipid membrane, Mol. Membr. Biol. 23 (2006) 137-148.

(13) S. Chiantia, N. Kahya, J. Ries,P. Schwille, Effects of ceramide on liquid-ordered domains investigated by simultaneous AFM and FCS, Biophys. J. 90 (2006) 4500-4508.

(14) S. Chiantia, N. Kahya,P. Schwille, Raft domain reorganization driven by short- and long-chain ceramide: a combined AFM and FCS study, Langmuir. 23 (2007) 7659-7665.

(15) L. C. Silva, R. F. M. de Almeida, B. M. Castro, A. Fedorov,M. Prieto, Ceramide-domain formation and collapse in lipid rafts: Membrane reorganization by an apoptotic lipid, Biophysical Journal. 92 (2007) 502-516.

(16) Megha, O. Bakht,E. London, Cholesterol precursors stabilize ordinary and ceramide-rich ordered lipid domains (lipid rafts) to different degrees. Implications for the Bloch hypothesis and sterol biosynthesis disorders, J. Biol. Chem. 281 (2006) 21903-21913.

(17) L. C. Silva, R. F. de Almeida, B. M. Castro, A. Fedorov,M. Prieto, Ceramide-domain formation and collapse in lipid rafts: membrane reorganization by an apoptotic lipid, Biophys. J. 92 (2007) 502-516.

(18) E. Gulbins,H. Grassme, Ceramide and cell death receptor clustering, Biochim. Biophys. Acta. 1585 (2002) 139-145.

(19) E. Gulbins, S. Dreschers, B. Wilker,H. Grassme, Ceramide, membrane rafts and infections, J. Mol. Med. 82 (2004) 357-363.

(20) J. Riethmuller, A. Riehle, H. Grassme,E. Gulbins, Membrane rafts in host-pathogen interactions, Biochimica et Biophysica Acta-Biomembranes. 1758 (2006) 2139-2147.

(21) A. B. Abdel Shakor, K. Kwiatkowska,A. Sobota, Cell surface ceramide generation precedes and controls FcgammaRII clustering and phosphorylation in rafts, J. Biol. Chem. 279 (2004) 36778-36787.

(22) H. Grassme, V. Jendrossek, J. Bock, A. Riehle,E. Gulbins, Ceramide-rich membrane rafts mediate CD40 clustering, J. Immunol. 168 (2002) 298-307.

(23) H. Grassme, A. Jekle, A. Riehle, H. Schwarz, J. Berger, K. Sandhoff, R. Kolesnick,E. Gulbins, CD95 signaling via ceramide-rich membrane rafts, Journal of Biological Chemistry. 276 (2001) 20589-20596.

(24) N. Kahya, Targeting membrane proteins to liquid-ordered phases: molecular self-organization explored by fluorescence correlation spectroscopy, Chem. Phys. Lipids. 141 (2006) 158-168.

(25) Z. G. Li, E. Mintzer,R. Bittman, First synthesis of free cholesterol - BODIPY conjugates, Journal of Organic Chemistry. 71 (2006) 1718-1721.

(26) N. Kahya, D. A. Brown,P. Schwille, Raft partitioning and dynamic behavior of human placental alkaline phosphatase in giant unilamellar vesicles, Biochemistry. 44 (2005) 7479-7489.

(27) R. Schroeder, E. London,D. Brown, Interactions between saturated acyl chains confer detergent resistance on lipids and glycosylphosphatidylinositol (GPI)-anchored proteins: GPI-anchored proteins in liposomes and cells show similar behavior, Proc. Natl. Acad. Sci. U. S. A. 91 (1994) 12130-12134.

(28) K. Bacia, C. G. Schuette, N. Kahya, R. Jahn,P. Schwille, SNAREs prefer liquid-disordered over "raft" (liquid-ordered) domains when reconstituted into giant unilamellar vesicles, J. Biol. Chem. 279 (2004) 37951-37955.

(29) C. G. Schuette, K. Hatsuzawa, M. Margittai, A. Stein, D. Riedel, P. Kuster, M. Konig, C. Seidel,R. Jahn, Determinants of liposome fusion mediated by synaptic SNARE proteins, Proceedings of the National Academy of Sciences of the United States of America. 101 (2004) 2858-2863.

(30) S. Chiantia, J. Ries, N. Kahya,P. Schwille, Combined AFM and two-focus SFCS study of Raft-exhibiting model membranes, Chemphyschem. 7 (2006) 2409-2418.

(31) P. S. Tsai, K. J. De Vries, M. Boer-Brouwer, N. Garcia-Gil, R. A. Van Gestel, B. Colenbrander, B. M. Gadella,T. Van Haeften, Syntaxin and VAMP association with lipid rafts depends on cholesterol depletion in capacitating sperm cells, Molecular Membrane Biology. 24 (2007) 313-324.

(32) T. Lang, SNARE proteins and membrane rafts, J. Physiol. 2007)

(33) C. Salaun, G. W. Gould,L. H. Chamberlain, Lipid raft association of SNARE proteins regulates exocytosis in PC12 cells, Journal of Biological Chemistry. 280 (2005) 19449-19453.

(34) D. Lingwood,K. Simons, Detergent resistance as a tool in membrane research, Nat. Protoc. 2 (2007) 2159-2165.

(35) I. Kalus, A. Hodel, A. Koch, R. Kleene, J. M. Edwardson,M. Schrader, Interaction of syncollin with GP-2, the major membrane protein of pancreatic zymogen granules, and association with lipid microdomains, Biochemical Journal. 362 (2002) 433-442.

(36) D. E. Saslowsky, J. C. Lawrence, R. M. Henderson,J. M. Edwardson, Syntaxin is efficiently excluded from sphingomyelin-enriched domains in supported lipid bilayers containing cholesterol, J. Membr. Biol. 194 (2003) 153-164.

(37) I. Johnston,L. J. Johnston, Ceramide promotes restructuring of model raft membranes, Langmuir. 22 (2006) 11284-11289.

(38) C. S. Neish, I. L. Martin, R. M. Henderson,J. M. Edwardson, Direct visualization of ligand-protein interactions using atomic force microscopy, Br. J. Pharmacol. 135 (2002) 1943-1950.

(39) D. E. Saslowsky, J. C. Lawrence, R. M. Henderson,J. M. Edwardson, Syntaxin is efficiently excluded from sphingomyelin-enriched domains in supported lipid bilayers containing cholesterol, J. Membr. Biol. 194 (2003) 153-164.

(40) B. M. Castro, R. F. M. de Almeida,Silva L.C., Formation of Ceramide/Sphingomyelin gel domains in the presence of an unsaturated phospholipid: A quantitative multiprobe approach, Biophys. J. 93 (2007) 1639-1650.

(41) S. Udenfriend,K. Kodukula, How glycosylphosphatidylinositol-anchored membrane proteins are made, Annu. Rev. Biochem. 64 (1995) 563-591.

(42) S. Chatterjee,S. Mayor, The GPI-anchor and protein sorting, Cell Mol. Life Sci. 58 (2001) 1969-1987.

(43) K. Simons,G. van Meer, Lipid sorting in epithelial cells, Biochemistry. 27 (1988) 6197-6202.

(44) T. Harder, P. Scheiffele, P. Verkade,K. Simons, Lipid domain structure of the plasma membrane revealed by patching of membrane components, J. Cell Biol. 141 (1998) 929-942.

(45) D. A. Brown,J. K. Rose, Sorting of GPI-anchored proteins to glycolipid-enriched membrane subdomains during transport to the apical cell surface, Cell. 68 (1992) 533-544.

(46) V. Horejsi, M. Cebecauer, J. Cerny, T. Brdicka, P. Angelisova,K. Drbal, Signal transduction in leucocytes via GPI-anchored proteins: an experimental artefact or an aspect of immunoreceptor function?, Immunology Letters. 63 (1998) 63-73.

(47) T. Baumgart, G. Hunt, E. R. Farkas, W. W. Webb,G. W. Feigenson, Fluorescence probe partitioning between L(o)/L(d) phases in lipid membranes, Biochim. Biophys. Acta. 2007)

(48) K. Bacia, P. Schwille,T. Kurzchalia, Sterol structure determines the separation of phases and the curvature of the liquid-ordered phase in model membranes, Proc. Natl. Acad. Sci. U. S. A. 102 (2005) 3272-3277.

(49) A. K. Kenworthy, N. Petranova,M. Edidin, High-resolution FRET microscopy of cholera toxin B-subunit and GPI-anchored proteins in cell plasma membranes, Molecular Biology of the Cell. 11 (2000) 1645-1655.

(50) C. A. Redman, J. E. Thomasoates, S. Ogata, Y. Ikehara,M. A. J. Ferguson, Structure of the Glycosylphosphatidylinositol Membrane Anchor of Human Placental Alkaline-Phosphatase, Biochemical Journal. 302 (1994) 861-865.

(51) D. C. Carrer,B. Maggio, Transduction to self-assembly of molecular geometry and local interactions in mixtures of ceramides and ganglioside GM1, Biochimica et Biophysica Acta-Biomembranes. 1514 (2001) 87-99.

(52) J. Bock,E. Gulbins, The transmembranous domain of CD40 determines CD40 partitioning into lipid rafts, Febs Letters. 534 (2003) 169-174.

(53) C. Detre, E. Kiss, Z. Varga, K. Ludanyi, K. Paszty, A. Enyedi, D. Kovesdi, G. Panyi, E. Rajnavolgyi,J. Matko, Death or survival: membrane ceramide controls the fate and activation of antigen-specific T-cells depending on signal strength and duration, Cell Signal. 18 (2006) 294-306.

(54) J. E. Shaw, R. F. Epand, R. M. Epand, Z. G. Li, R. Bittman,C. M. Yip, Correlated fluorescence-atomic force microscopy of membrane domains: Structure of fluorescence probes determines lipid localization, Biophysical Journal. 90 (2006) 2170-2178.

(55) Megha,E. London, Ceramide selectively displaces cholesterol from ordered lipid domains (rafts): implications for lipid raft structure and function, J. Biol. Chem. 279 (2004) 9997-10004.

(55b) A. Zitzer, R. Bittman, C. A. Verbicky, R. K. Erukulla, S. Bhakdi, S. Weis, A. Valeva, M. Palmer, Coupling of cholesterol and cone-shaped lipids in bilayers augments membrane permeabilization by the cholesterol-specific toxins Streprolysin and Vibrio cholearae cytolysin., J. Biol. Chem. 276 (2001) 14628-14633.

(56) H. Grassme, A. Jekle, A. Riehle, H. Schwarz, J. Berger, K. Sandhoff, R. Kolesnick,E. Gulbins, CD95 signaling via ceramide-rich membrane rafts, J. Biol. Chem. 276 (2001) 20589-20596.

(57) C. M. Finnegan, S. S. Rawat, A. Puri, J. M. Wang, F. W. Ruscetti,R. Blumenthal, Ceramide, a target for antiretroviral therapy, Proc. Natl. Acad. Sci. U. S. A. 101 (2004) 15452-15457.

(58) C. M. Finnegan, S. S. Rawat, E. H. Cho, D. L. Guiffre, S. Lockett, A. H. Merrill,R. Blumenthal, Sphingomyelinase restricts the lateral diffusion of CD4 and inhibits human immunodeficiency virus fusion, Journal of Virology. 81 (2007) 5294-5304.

(59) D. H. Nguyen,D. D. Taub, Targeting lipids to prevent HIV infection, Mol. Interv. 4 (2004) 318-320.

(60) T. E. Fox, C. M. Finnegan, R. Blumenthal,M. Kester, The clinical potential of sphingolipid-based therapeutics, Cellular and Molecular Life Sciences. 63 (2006) 1017-1023.

(61) S. A. Gallo, C. M. Finnegan, M. Viard, Y. Raviv, A. Dimitrov, S. S. Rawat, A. Puri, S. Durell,R. Blumenthal, The HIV Env-mediated fusion reaction, Biochimica et Biophysica Acta-Biomembranes. 1614 (2003) 36-50.

Conclusions

The work described in this thesis can be summarized in two main points: i) the development of a novel combined approach of atomic force microscopy (AFM), laser scanning imaging (LSM), and fluorescence correlation spectroscopy (FCS) and ii) the study of the effects of ceramide in the lateral organization of model plasma membranes.

AFM is a powerful technique which allows a highly detailed topographical characterization of the sample surface in physiological conditions. While AFM imaging offers an extremely high spatial resolution, up to the nanometer scale, the limited image acquisition speed (~minutes) can pose a severe drawback in adequately studying fast dynamic processes. On the other hand, fluorescence based imaging techniques are much faster ($\sim 10^{-3}$-10^{0} s), but certainly lack the high spatial resolution that AFM offers. FCS in particular can also provide information about dynamic processes, like diffusion of fluorescent membrane components. For these reasons, implementing a combination of the above mentioned techniques on the same sample (e.g. cell membrane models) proves extremely beneficial in the complete dynamic and structural characterization of molecular interactions.

In this thesis, we described one of the first simultaneous applications of AFM and FCS on biologically relevant systems. More specifically, model membranes showing complex phase separation were investigated with a combined approach of AFM, confocal fluorescence imaging, force measurements and FCS, based on commercially available instruments. AFM conveys information about the structural and mechanical properties of the different lipid phases. Different membrane domains can be distinguished based on height difference, elastic properties and line tension as measured by the AFM tip. Simultaneous optical measurements offer the correlation of these data in real time with the partition behavior and diffusion of fluorescent lipids and proteins. We established a clear link between the local membrane viscosity, probed by FCS, and the lipid-lipid interactions involved in line tension, probed by AFM force measurements. An example of a significant drawback circumvented by the AFM-FCS approach involves the use of AFM micromanipulation to eliminate unwanted interactions between lipid particles — similar to intra-cellular vesicles found *in vivo* experiments — and the membrane, which usually result in distorted FCS autocorrelation curves. Finally, the combined application of AFM and FCS on membrane-anchored proteins reconstituted in lipid bilayers has been instrumental in clarifying inconsistencies that arose in work that focused solely on either AFM or fluorescence techniques. We have shown that, in the case of proteins diffusing in the plane of the membrane, AFM can unambiguously detect only a small immobile fraction. Furthermore, since AFM detection of proteins might be facilitated by high local membrane viscosity (e.g. in ordered lipid phases), the measurement of protein partition between disordered and ordered membrane domains might be biased toward the latter. In this case, the use of FCS as a complementary technique allows a more thorough investigation and deeper understanding of the system of interest.

The second part of this thesis dealt with the study of complex lipid mixtures which are used to model the putative lipid/proteins domains in cells, called “rafts”. Firstly, we proved how the combined fluorescence imaging/AFM approach is useful in general for studying supported lipid membranes and the role of lipid domains in biological contexts. We investigated the effect of environmental stress on biological membranes and the protective effects of several substances. Our experimental approach was shown to be a new valuable method to visualize the dehydration damage and its effects on the lateral organization of lipid domains. Our results demonstrated that disaccharides like trehalose or sucrose are effective in protecting lipid membranes, not only on a macroscopic scale — preserving the overall integrity of the bilayer — but also on a microscopic scale, preventing the clustering of microdomains. These

phenomena are interesting in the context of biological damage to living cells which need to be stored for long time, like organs to be transplanted or blood platelets.

Finally, a large part of this thesis focused on the effects of a specific lipid called "ceramide" on the lateral organization of proteins and lipids in the plasma membrane. Ceramide is produced by cells in several situations, like bacterial infections or apoptosis. As consequence of ceramide production *in vivo*, the local concentration and the dynamic behavior of lipids and membrane receptors are supposed to exhibit strong variations. In order to understand the molecular mechanisms responsible for these effects, we applied a combination of AFM, FCS and fluorescence imaging on simple model membranes containing ceramide. We could show for the first time that, in presence of raft-like L_o/L_d phase separation, physiological quantities of ceramide induced the formation of a highly ordered gel phase, constituted of ceramide and sphingomyelin. The enzymatic production of ceramide was monitored both in supported and in free-standing bilayers. In the second case, ceramide production was connected to selective vesicle budding from the raft-like phase. The same mechanism was shown to be involved in protein and lipid sorting during formation of endosomes *in vivo*.

Since short-chain analogues are often used in both medical applications and biochemical research to mimic the effect of long-chain ceramides, we investigated the effect of chain-length on ceramide-induced membrane reorganization. We could show that only long-chain ceramides (C18 and C16) form highly ordered domains. Interestingly, FCS measurements indicated that the physical properties of the L_o raft-like domains are hardly affected by the presence of ceramide domains. Furthermore, the increased thickness of the L_d phase — as measured by AFM — and its higher viscosity — as measured by FCS — strongly support the hypothesis of ceramide-induced cholesterol displacement from rafts. On the other hand, short-chain ceramides showed completely different biophysical properties that lead to a destabilization of the raft domains, possibly acting as surfactants between the different lipid phases. Our findings contribute to the explanation of *in vivo* experiments where short-chain ceramides inhibit, for example, IgE-FcεRI signaling by disrupting the lipid order in the plasma membrane.

We have so far demonstrated that ceramide plays a fundamental role in lipid-lipid interactions. In a physiological context, it is also known to produce dramatic effects in living cells. Since a majority of the processes *in vivo* are thought to be governed by the activity of proteins, it is highly likely that ceramide not only affects lipid organization but also modifies protein-protein and protein-lipid interactions to produce its effects. To test this hypothesis, we reconstituted several membrane proteins in lipid bilayers containing L_d, L_o, and ceramide-rich domains. We were able to show that some membrane proteins are sorted into ceramide-rich domains. More specifically, the raft-associated proteins we tested were enriched in the highly ordered ceramide-rich domains, while the L_d-associated components were excluded from them. Furthermore, the inclusion of any membrane component in ceramide-rich domains is directly connected to a dramatic reduction of its in-plane diffusion. In an *in vivo* context, such a reorganization of membrane receptors might be used by the cell to alter the signaling process, for example, by i) separating raft receptors from inhibitors with lower raft affinity, ii) bringing both raft-associated receptors and raft-associated signaling molecules into contact, or iii) stabilizing the interactions between a receptor and its ligand by decreasing their diffusion coefficients.

In conclusion, this thesis describes a novel combination of AFM, LSM, and FCS for the investigation of the lateral organization of biological membranes. Our results show that this approach applied on model membranes of increasing complexity is an effective tool for understanding the molecular mechanisms behind the organization of biological membranes. This report opens up new possibilities for further investigation in living cell membranes using the same methodology we have described.

List of symbols and abbreviations

A: Resonance frequency of the AFM cantilever
AFM: Atomic force microscopy
Alexa488CholToxin: Alexa 488 labelled Cholera toxin
APD: Avalanche photodiode
Bod: Bodipy fluorescent probe
BODIPY-CholeE: Cholesteryl-Bodipy FL
BODIPY-FChol: Bodipy FL free cholesterol analogue
c: Concentration
c_A: Concentration in phase A
Cer: Ceramide
CT*x*-B: Cholera Toxin subunit B
D: Diffusion coefficient
D*: Relative diffusion coefficient
dc: Direct contact
dcFCCS: Dual color fluorescence cross-correlation spectroscopy
DHPE/DPPE: Dipalmitoylphostaphatidyletanolamine
DiD: 1,1'-Dioctadecyl-3,3,3',3'-tetramethylindodicarbocyanine perchlorate
DiO: 3,3'-dioctadecyloxacarbocyanine perchlorate
DMSO: Dimethyl sulfoxide
DOPC: Dioleoylphosphatidylcholine
DPH: 1,6-diphenyl-1,3,5-hexatriene
DPPC: Dipalmitoylphosphatidylcholine
DRM: Detergent resistant membranes
DSC: Differential scanning calorimetry
E: Fluorescence detection efficiency
EM: Electron microscopy
F: Fluorescence signal
F: Force applied by/on the AFM cantilever
FCεRI: High affinity immunoglobulin epsilon receptor
FCS: Fluorescence correlation spectroscopy
FL: Fluorescine
FRAP: Fluorescence recovery after photobleaching
FRET: Forster/Fluorescence resonance energy transfer
F_t: Threshold yield
FTIR: Fourier transform infra-red
G: Autocorrelation function
Γ: Line tension
G(0): Amplitude of the autocorrelation function
GPI: Glycosyl-phosphatidyl-inositol
GUV: Giant unilamellar vesicle
G^x: Cross-correlation function
η: Fluorescence quantum yield
HTF: Dichroic mirror
Hz: Hertz

I: Excitation profile
IgE: Immunoglobulin E
K: Spring constant of the AFM cantilever
K(A/B): Partition coefficient between phases A and B
k_B: Boltzmann constant
k_D: Inverse of Debye lenght
λ: wavelenght
L_α: Liquid crystalline phase
L_β, $L_{\beta'}$ or $L_{\beta I}$: Gel phase
L_d: Liquid disordered phase
L_o: Liquid ordered phase
LSM: Laser scanning microscope
M: molar concentration
MLV: Multilamellar vesicles
Mol: Moles
n: Index of refraction
N/NP: Number of particles
NMR: Nuclear magnetic resonance
PC: Phosphatidylcholine
PE: Phosphatidylethanolamine
PLAP: Placental alkaline phosphatase
PMT: Photomultiplier
POPC: 1-Palmitoyl-2-oleoyl-sn-glycero-3-phosphocholine
PS: Phosphatidylserine
q: Molecular brightness
r: Position vector
R: Radius of the tip of the AFM cantilever
r_h: Radius of a hole in the membrane
Rho: Rhodamine fluorescent probe
S: Surface energy
s: Volume horizontal extension in 2-focus scanning fluorescence correlation spectroscopy
σ_0: Lennard-Jones zero potential radius
σ_{exc}: Fluorescence excitation cross-section
sFCS: Scanning fluorescence correlation spectroscopy
SFM: Scanning force microscopy
SLB: Supported lipid bilayer
SM: Sphingomyelin
SMase: Sphingomyelinase
SNOM: Scanning near-field microscopy
s_o: Solid ordered phase
SP: Structure parameter
SPM: Scanning probe microscopy
SPT/SMT: Single particle/molecule tracking
SSB: Solid supported bilayer
SSM: Solid supported membrane
STM: Scanning tunneling microscopy
SUV: Small unilamellar vesicle

T: Temperature
t: Time
τ_D: Diffusion time
V_{eff}: Effective volume
W: Shape function of fluorescence detection volume
W_0: Radius of FCS volume in the x-y plane
Y: Normalized fluorescence collection efficiency
Z_0: Extension of FCS volume in z direction
Ψ: Electric potential

Acknowledgments

The experiments described in this thesis were performed in the laboratory of Prof. Dr. Petra Schwille, in the Biotechnologische Zentrum of the Technische Universität Dresden.

This work was partially financed by EFRE Grant 4121/0402.

I would like to thank all the people who helped me during these three years in Dresden and especially:

Petra, for giving me the opportunity to join her group and to carry out my doctoral work in a very stimulating environment. Thanks for giving me trust, assistance and independence, allowing me to choose my own projects and being patient also in moments when things were not great.

Nicoletta Kahya, for the great help and encouragement at the beginning of my PhD. Thanks for showing me how to work diligently and for all the suggestions about the ceramide projects.

All the people who actively helped me in performing the experimental work and in writing papers: Ana García Sáez, Jonas Ries, Grzegorz Chwastek, Lawrence Rajendran, Lars Renner, Dolores Carrer, Ünal Coskun, Robert Bittman, Kirsten Bacia, Karin Krell, Barbara Borgonovo and Mikael Simons.

All the former and current members of the Schwille Group.

Those who helped me proof-reading and discussing this thesis: Alexej Kedrov, Madhavi Krishnan, Annalisa Marsico, Ana, Jonas, Dolores, Lars.

Prof. Dr. Erwin London and Prof. Dr. Lukas Eng for kindly agreeing to review this thesis.

P. H. Puech, S. Morandat, H. Janovjak and Prof. Daniel Müller for introducing me to the use of atomic force microscopy.

All the people in the JPK company in Berlin and, in particular, Rachel Owen.

Claudia Lorenz for the precious help with german burocracy.

A special thank goes to my colleagues and friends who shared the office with me: Ana Jesus, Jonsie and Madhavi. Thanks for being patient friends, in good and bad times, and for bringing some unplanned chaos and laughs in my everyday lab life.

Finally I would like to thank my family for their support and for being always close, in spite of the thousand kilometer distance from home.

Erklärung (Declaration)

Hiermit versichere ich, dass ich die vorliegende Arbeit ohne unzulässige Hilfe Dritter und ohne Benutzung anderer als der angegeben Hilfsmittel angefertigt habe; die aus fremden Quellen direkt oder indirekt übernommenen Gedanken sind als solche kenntlich gemacht. Die Arbeit wurde bisher weder im Inland noch im Ausland in gleicher oder ähnlicher Form einer anderen Prüfungsbehörde vorgelegt.

Diese Arbeit wurde von Juni 2004 bis Dezember 2007 unter der Betreuung von Prof. Dr. Petra Schwille an der Technischen Universität Dresden angefertigt.

Dresden, den 15.12.2007

I herewith declare that I have produced this thesis without the prohibited assistance of third parties and without making use of aids other than those specified; notions taken over directly or indirectly from other sources have been identified as such. This thesis has not been previously presented in identical or similar form to any other german or foreign examination board.

The thesis work was conducted between Juni 2004 and December 2007 under the supervision of Prof. Dr. Petra Schwille at the Dresden University of Technology.